UNIVERSITÉ DU LUXEMBOURG

PhD-FSTM-2025-001

Faculty of Science, Technology and Medicine

DISSERTATION

Defence held on 15 January 2025 in Esch-sur-Alzette

to obtain the degree of

DOCTEUR DE L'UNIVERSITÉ DU LUXEMBOURG EN SCIENCES DE L'INGÉNIEUR

by

Raquel NAVARRO BUENDÍA

Born on 07/11/1993 in Barcelona (Spain)

Precision Altimetry Using Dual-Frequency Grazing Angle GNSS-R

Dissertation Defence Committee:

Dr Sajad TABIBI, Dissertation supervisor

Research scientist, Université du Luxembourg

Prof Francesco VITI, Chairman

Associate professor, Université du Luxembourg

Prof Olivier FRANCIS, Vice Chairman

Professor, Université du Luxembourg

Dr Dallas MASTERS

Muon Space, Boulder, Colorado, USA

Dr Matthieu TALPE

Spire Global, Luxembourg

To my uncle (in memoriam) whose support and passion for my work were indescribable.

“*Toujours en avant*", Carlos Urkiola

Acknowledgements

I express my gratitude first of all to the Luxembourg National Research Fund (FNR) for generously providing the funding for my 4-year PhD contract. Without their support, this research would not have been possible. Second, the Luxembourg Space Agency (LSA) for granting me access to their invaluable data, which greatly enriched my research and allowed me to make significant contributions to my field of study and finally Spire Global Inc. for the fruitful collaboration and the exchange of data.

I would like to express my heartfelt gratitude to the following individuals who have played an fundamental role in making my journey through my PhD a memorable and successful one:

To the members of the jury, Matthieu Talpe, Dallas Masters, Francesco Vitti, Olivier Francis, and Sajad Tabibi, my thanks go to their time invested, expertise, and invaluable feedback. Their discerning comments and constructive critique managed to significantly improve my research, and I appreciate their dedication to assessing my work.

Olivier Francis deserves a special mention for making my PhD experience one of the best and most rewarding periods of my life. His guidance, expertise, encouragement, and unconditional support were invaluable.

I am deeply grateful to Sajad Tabibi for his unwavering support and mentorship throughout my PhD journey. His supervision and help have been a constant source of inspiration and have undoubtedly shaped the quality of my work.

I extend my thanks to my wonderful colleagues, who have not only been supportive but have also added laughter and joy to my daily life at the office. Their constant support has

made this PhD journey infinitely more enjoyable.

Last but not least, I want to express my profound appreciation to my friends and family for their endless support, encouragement, and understanding. Their unwavering belief in me has been the driving force behind my accomplishments. In particular, my best friend Cristina, with whom I have shared all the ups and downs since university, and my partner, whose unconditional love and patience throughout this process have been invaluable.

Finally, I would like to express my special gratitude to my mother. She is the strongest woman I have ever met and has inspired me to believe that truly anything is possible. "Mama, sempre has estat al meu costat de forma incondicional, estimant-me i recolzant-me en cada pas que he fet en la meva vida. No tinc paraules per expressar com d'important va és això per a mi. Sense tu no seria on soc." I love you more than anything.

To all these individuals and organizations, I offer my sincerest gratitude for their contributions, without which my PhD would not have been as fulfilling and successful as it has been.

Thank you all from the bottom of my heart.

Index

1 Introduction **1**

1.1 Motivation and objectives 1

1.2 Contributions 3

1.3 Overview 5

2 Global Navigation Satellite Systems Reflectometry (GNSS-R) **7**

2.1 Global Navigation Satellite Systems (GNSS) 7

2.1.1 Signal's data 9

2.1.2 Data corrections 10

2.2 Global Positioning System (GPS) 11

2.3 Global Navigation Satellite System - Reflectometry (GNSS-R) 14

2.3.1 History 14

2.3.2 Basic principles 14

2.3.3 Differences on low and high elevation angle range 19

2.3.4 Current applications & missions 19

2.3.5 Future directions 21

3 Altimetry retrieval using Grazing Angle GNSS-R (GG-R) measurements **23**

3.1 Data measurements 24

3.2 Model formulation 28

3.3 Coherency criteria 30

3.4 Phase ambiguity 30

3.5 Atmospheric delay . . . 33
3.5.1 Ionospheric delay . . . 33
3.5.2 Tropospheric delay . . . 39
3.6 Reference surface models . . . 42

4 Ocean and sea-ice GG-R altimetry **45**
4.1 Inital GG-R Altimetry in the Hudson Bay . . . 45
4.1.1 Data and Models . . . 47
4.1.2 Altimetry Retrievals . . . 47
4.1.3 Summary . . . 50
4.2 Coherency and sea ice concentration correlation over Hudson Bay . . . 52
4.2.1 Data and Models . . . 52
4.2.2 Results . . . 53
4.2.3 Summary . . . 57
4.3 An improved ionospheric correction model for GG-R altimetry . . . 60
4.3.1 Data and Models . . . 61
4.3.2 Frequency-specific ionospheric delay correction . . . 61
4.3.3 Results and discussion . . . 61
4.3.4 Summary . . . 64
4.4 Enhancing the GG-R altimetry parameters and models . . . 67
4.4.1 Spire's selection and model formulation validation . . . 68
4.4.2 Phase unwrapping methods and Continuity QC filter windows . . . 69
4.4.3 Tropospheric models . . . 70
4.4.4 MSS and Tidal models . . . 71
4.4.5 Ionospheric frequency combinations . . . 73
4.4.6 Optimal combination . . . 78
4.5 Comparison of Sea Surface Height Anomaly Measurements from GG-R and Satellite altimetry Missions . . . 79
4.5.1 Data description and model formulation . . . 81

4.5.2 Results 84
4.5.3 Discussion and Interpretation 96
4.5.4 Summary 98

5 Ice-sheet GG-R altimetry over Greenland and Antarctica 105
5.1 Data and Models 106
5.2 GG-R Ice Sheet Height Retrievals 107
5.3 Height Retrieval over Greenland 107
5.4 Height Retrieval over Antarctica 111
5.5 Collocated Height Profiles 113
5.6 Discussion and Interpretation 116
5.7 Summary 118

6 Software and L2 data product 121
6.1 GRAALT description 121
6.2 Geophysics Laboratory (GL) L2 data product 125

List of Figures

2.1 GPS, Galileo, GLONASS and BeiDou frequencies and spectrum [21] 8

2.2 GNSS-R signal reflection from the transmitter to the reflection point Specular Point (SP) and then to the receiver. The angle α represents the elevation angle from the tangent plane to the transmitter/receiver from the SP. 15

2.3 (a) Coherent and (b) incoherent DDM extracted from CYGNSS mission, with analogy of moonlight reflections on a lake (smooth surface) and on the sea (rough surface). 17

2.4 Most relevant GNSS-R missions and their year launch years. 18

3.1 Spire grazing angle GNSS-R geometry. TR is computed based on positions of the transmitter, nanosatellite and specular point on WGS84 ellipsoid surface. And $T\hat{X}R$ is based on Spire GNSS-R phase measurements 28

3.2 Scheme of Cycle-Slip detection and correction function 31

3.3 Day and night ionospheric regions and atmospheric layers 34

3.4 Low grazing angles GG-R signal through troposphere and ionosphere 35

4.1 Reflections observed over the area of Hudson Bay from January to March 2021 46

4.2 National Oceanic and Atmospheric Administration (NOAA) Sea-ice extend from January to December 2021 [80] 47

4.3 GG-R event over Hudson Bay on 23 January 2021 04:24:47 UTC (blue line) surface height retrievals (orange line) reference surface model. The RMS between the surface height and the reference surface model is 181.9 m . . . 48

4.4 Measurement coverage and coherence percentage over Hudson Bay from January to March 2021 48
4.5 Histogram of RMS differences between GG-R height profiles and DTU + TPXO 49
4.6 (top) GG-R event over Hudson Bay on 24 January 2021 20:26:52 UTC, and (bottom) surface height retrievals (blue dot) and modeled sea surface height (red line) 51
4.7 Surface height deviation minus computed reference surface as a function of specular point elevation angle 51
4.8 January to October 2021 plots of sea ice concentration (odd rows) in percentage from 0% indicating no ice present to 100% representing the highest sea ice concentration, and (even rows) percentage of coherency of GG-R measurements from 0% indicating no coherency to 100% representing the highest coherency value, averaged in a 4-km MASAM2 polar stereographic grid. 55
4.9 Sea ice concentration in percentage (top panel) and the percentage of coherency of GG-R measurements (bottom panel). Data from January to May (left column) and from July to October 2021 (right column), averaged in a 4-km MASAM2 polar stereographic grid. 58
4.10 Two GG-R events for March 27, 2021, at 02:41:39 UTC (FM102) and 03:19:10 UTC (FM122). 59
4.11 Density of GG-R events over Java Sea from January 2020 to October 2021 and the historical altimetry ground tracks since 1992 (red dots) 62
4.12 GG-R Profile generated on November 30, 2020 at 02:57:34 UTC by FM122 tracking PRN15. (a) Collected (light blue) and coherent (dark blue) segments and first measurement (yellow arrow); (b) Heights from WGS84 for ionosphere-free combination (black dot) and frequency-specific ionospheric delay correction (gray dot) and reference surface model (yellow line); (c) Height residuals between the reference model and GG-R retrievals; (d) Ionospheric delay from frequency-specific correction method. 65

4.13 The reference track (blue) is the profile used in Figure 4.12 and the collocated track (red) is generated by FM120 tracking the same signal from PRN15 but was taken 20 sec apart from the reference track; (a) Collected (blue and red for the reference and collocated tracks, respectively) and coherent segments and first measurements (yellow arrows); (b) Physical distance over specular point latitude (coherent segments is shown in yellow) ; (c) Relative heights for the reference (blue) and collocated tracks (red) from WGS84 over specular point latitude; (d) Height residuals between the two collocated GG-R events. . 66
4.14 Tropospheric model delay differences vs. elevation angle in Hudson Bay from July to September 2021. (a) GFS model minus VMF3/GPT3 (b) GFS minus UNB3m (c) VMF3/GPT3 minus UNB3m 72
4.15 Graphical examples of the GPS L_1 frequency specific correction for different window ranges (from 1 to 100 km) and three different smoothing filters; Savitzky-Golay filter (Order 3) and moving Mean and Median window 77
4.16 GG-R geometry and the definition of Sea Surface Height (SSH) with respect to the reference ellipsoid, illustrating the deviation of the SSH from the Mean Sea Surface (MSS) as the Sea Level Anomaly (SLA). 80
4.17 Identified tracks for the comparison between satellite altimetry and Spire GG-R measurements in the North Pole (a), South Pole (b), the Southeast Asian Seas (SEAS) (c), and Gulf of Mexico and surrounding areas (d). Dark blue, light blue, magenta, and yellow represent Sentinel-3A, Sentinel-3B, Saral, and Cryosat-2, respectively. 85

4.18 From left to right the examples from North and South Pole, Gulf of Mexico and Java Sea from Sentinel-3A, Sentinel-3B, Saral and Cryosat-2 respectively. (a) Locations of Sentinel-3A/B, Saral, and CryoSat-2 profiles (blue line) and Spire profiles (red line), (b) Physical distance between the collocated events in km, (c) SP elevation angle for the Spire GG-R track, (d) Absolute height w.r.t WGS84 of RA (blue line), GG-R 50 Hz (black dots), and GG-R 1 Hz (red line), and (e) SLA for each track compared with SLA derived from CMEMS grid data 89
4.19 Geophysical coverage and SLA RMSE of the 938 GG-R collocated tracks, with a maximum time difference of 30-sec between each track pair and an average physical distance of 10 km among all the Spire data available for this study. 92
4.20 GG-R collocated events with the first three columns representing examples located in the Arctic region and the last column showing an example in Antarctica 100
4.21 Number of Spire GG-R observations from May 2019 to June 2020 displayed in (a) EASE 9-km Cylindrical grid, (b) North EASE 9-km Grid Projection, and (c) South EASE 9-km Grid Projection 101
4.22 Grid of prevalence of measurements. Spire GG-R L2 measurements (green), RA (red) data from the first week of June 2020. (a) EASE 9-km Cylindrical grid, (b) North EASE 9-km Grid Projection, and (c) South EASE 9-km Grid Projection 102
4.23 Percentage of coherency from May 2019 to June 2020 computed with an average moving window of the unwrapped and corrected for cycle-slips phase residual differences of L1 and L2 from the reflected signal. (a) EASE 9-km Cylindrical grid, (b) North EASE 9-km Grid Projection, and (c) South EASE 9-km Grid Projection and Zoom-in the regions of (d) Gulf of Mexico, (e) Indonesian SEAS, and (f) Hudson and James Bay area. 103

4.24 Examples of complementary tracks from Sentinel-3A and Cryosat-2: (a) Locations of Sentinel-3A/3B (blue) and Spire (red), (b) Physical distance in km, (c) SP elevation angle for Spire GG-R track, (d) Relative height w.r.t WGS84 for GG-R (50 Hz in black dots and 1 Hz in red line) and RA (blue line), and (e) SLA_{CMEMS} (grey crosses). 104

5.1 Spire L1B tracks generated from January to October 2021 are shown in yellow, while the L2-LR tracks used for ice sheet retrieval are shown in purple over Greenland (left) and Antarctica (right). The white line in the center of Antarctica delineates the 88° boundary where satellite altimeters, such as CryoSat-2 or IceSat-2, do not provide coverage. The dark line delineates the 81.5 ° boundary where satellite radar altimeters such as European Remote Sensing (ERS)-1/2, ENVISAT, and Sentinel-3 do not provide coverage. 108

5.2 GG-R event over Greenland on 26 September 2021 at 13:41:33 UTC. (a) Collected phase observations (yellow) and coherent segments that are successfully unwrapped (purple). The black triangle indicates the first measurement location; (b) SP elevation during the GG-R event; (c) GG-R height profile (blue) since the first measurement, using the ArcticDEM as the reference model (red); (d) Residual of the GG-R height profile relative to the ArcticDEM 109

5.3 Coherent segments color-coded based on the RMSE between the GG-R height retrievals and ArcticDEM as the reference model in Greenland, along with an overlay of the surface slope [116]. The inset provides a better illustration of the correlation between the GG-R tracks and surface slopes. 110

5.4 GG-R event over Antarctica on 5 August 2021 23:55:21 UTC. (a) Collected data (yellow), coherent segments (purple). The black triangle indicates the first measurement; (b) SP elevation during the GG-R event and (c); GG-R height profile (blue) since first measurement and the REMA as the reference model (red); and (d) residual of (c) 112

5.5 Coherent segments color-coded by the RMSE between the height retrievals and the reference model (REMAv1.1 at 200-meter spatial resolution) for the period of January to October 2021 over Antarctica, with an overlay of the surface slope. The inset displays the depiction of Antarctic surface slopes [116].113
5.6 Collocated GG-R profiles generated by FM102 as the reference track and FM099 as the collocated track on August 21, 2021; (b) Physical distance between the reference and collocated tracks; (c) SP elevation during the collocated GG-R events; (d) GG-R collocated height profiles of the FM102 (blue) and FM099 (red); (e) residual of (d); (f) The green color in the top panel depicts the residual of (d) and blue color shows the residual of REMA at FM102 and FM099. Residuals of the top panel (bottom panel) 114
5.7 Collocated GG-R profiles generated by FM099 on April 30, 2021 as the reference track and FM102 on September 01, 2021 as the collocated track. The panels and colors are similar to those of Figure 5.6. 115
5.8 Cumulative distribution function of the track-wise RMSE in Antarctica (cyan) and Greenland (green) 117
5.9 (a) Comparison of RMSE as retrieved for each individual segment over Greenland (green) and Antarctica (cyan); (b) GG-R residuals over retrieved height amplitude 118

6.1 GRAALT software interface 122
6.2 GRAALT software flowchart 126
6.3 Histogram of RMSE differences between GG-R height profiles 130

List of Tables

2.1 Current and Future GPS Generations [25] 13

3.1 Spire CubeSats orbit types and deployment dates used in this dissertation . . 25
3.2 List of L1B Spire data variables and their description 27
3.3 Models and methods used in this study for altimetric retrieval 29
3.4 Summary table of the reference surface models used in this thesis, including MSS, Tidal models and DEM models 41

4.1 Percentage of RMS error between the GG-R profiles and the reference surface model 49
4.2 RMS differences between GG-R height profiles computed with different reference surface and tropospheric models 50
4.3 January to October 2021 summary table of results including the ice concentration and the percentage of compared grid cells. 57
4.4 Percentage of RMSE between the reference surface model and GG-R height retrievals applying ionosphere-free combination and smoothed frequency-specific correction based on dual-frequency carrier phase observations 63
4.5 Summary of the parameters and models for Spire GG-R altimetry 67
4.6 Spire L2 parameters and models selection 68
4.7 Phase unwrapping methods, including the coherency and continuity filters, i.e. quality control filters 70
4.8 Tropospheric delay estimation models 71

4.9 Reference surface models selection 73
4.10 (row 1) Ionospheric-free combination. Frequency specific methods; the first method (row 2) uses only L_1 GPS frequency, the second method (row 3) L_2 and the third method is an average of L_1 and L_2 methods. 74
4.11 Altimetry results using various filters and physical kilometer windows from frequency-specific method 75
4.12 Parameters and models for the most optimal solution 78
4.13 Information on altimetry missions Sentinel-3A/B [98], Saral [97], and Cryosat-2 [96] 82
4.14 Models and methods used in this study for altimetric retrieval 83
4.15 Comparison of GG-R and satellite altimetry measurements. The second row represents the RMSE between GG-R altimetric retrieval and collocated RA measurement; the third raw ($SLA_{GG\text{-}R\ vs.\ RA}$) indicates the RMSE differences of estimated sea level anomaly derived from GG-R height profile and RA retrieval; the fourth row ($SLA_{GG\text{-}R\ vs.\ CMEMS}$ RMSE) shows the RMSE differences between $SLA_{GG\text{-}R}$ and SLA derived from CMEMS grid data (SLA_{CMEMS}), the last row represents the RMS differences between the SLA derived from the radar altimeter (SLA_{RA}) and SLA_{CMEMS}. 86
4.16 Comparison of GG-R and satellite altimetry measurements for the four selected tracks in different regions 90
4.17 Comparison of four GG-R collocated events from Figure 4.20 94
4.18 Comparison of complementary tracks from Figure 4.24 97

5.1 Number of L1B, L2, L2-Low Resolution (LR) profiles and total number of segments in Greenland and Antarctica from January to October 2021 107

6.1 List of Variables in the L2 GL product 127
6.2 List of Attributes in the L2 GL product 128
6.3 Parameters and models for the world wide L2 GL altimetry product 129

6.4 Percentage of RMSE between the GG-R height and the reference surface model 129

List of Publications

The original publications produced during the course of my PhD candidacy are listed below. These publications are referenced in the text as *J* = Journal Article, *C* = Conference Paper, and *P = Presentation*.

J_1 - Raquel N. Buendía et al. “Ice sheet height retrievals from Spire grazing angle GNSS-R”. In: *Remote Sensing of Environment 297 (2023)*, p. 113757. ISSN: 0034-4257.
DOI: 10.1016/j.rse.2023.113757

J_2 - Raquel N. Buendía, Sajad Tabibi, and Olivier Francis. “Exploring Grazing Angle GNSS-R for Precision Altimetry: A Comparative Study". In: *Remote Sensing of Environment*. Under review.
DOI: 10.1016/j.rse.2025.114604

C_1 - Raquel N. Buendía, Sajad Tabibi, and Matthieu Talpe. “Preliminary GNSS-R Altimetry in the Hudson Bay Based on Spire Grazing Angle Measurements”. In: *IGARSS 2022 - 2022 IEEE International Geoscience and Remote Sensing Symposium. 2022, pp. 7135–7138*.
DOI: 10.1109/IGARSS46834.2022.9883079

C_2 - Raquel N. Buendía, Sajad Tabibi, and Matthieu Talpe. “An Improved Ionospheric Correction Model for Grazing Angle GNSS-R Altimetry”. In: *IGARSS 2023 - 2023 IEEE International Geoscience and Remote Sensing Symposium. 2023*, pp. 4332–4335. DOI: 10.1109/IGARSS52108.2023.10282507

C_3 - Raquel N. Buendía, Sajad Tabibi, and Matthieu Talpe. “Comparison of sea surface height anomaly measurements from grazing angle GNSS-R Altimetry and Sentinel-3" *IEEE GNSS+R 2023 - Specialist Meeting on Reflectometry using GNSS and other Signals of Opportunity*.

C_4 - Raquel N. Buendía, Sajad Tabibi, and Olivier Francis. “Relation between GG-R carrier phase signal coherency and Sea Ice Concentration over Hudson Bay”. In: *2024 IEEE International Geoscience and Remote Sensing Symposium (IGARSS) (2024)*.
DOI: 10.1109/IGARSS53475.2024.10640714

P_1 - Raquel N. Buendía, Sajad Tabibi, and Olivier Francis. “GNSS-R Grazing Angle for Sea Ice Altimetry". In: *DTU Driven Colloquium 2021*, Belval, Esch-sur-Alzette, Luxembourg.

P_2 - Raquel N. Buendía, Sajad Tabibi, and Olivier Francis. “Optimizing GNSS-R Grazing Angles for Altimetry Applications". In: *DTU Driven Annual meeting and Workshop 2023*, Kanzem (Saar), Germany.

P_3 - Raquel N. Buendía, and Sajad Tabibi. “Advancing Earth observation through spaceborne GG-R by GRS". In DPCSS - PhD presentation Day, Belval, Esch-sur-Alzette, Luxembourg.

C_5 - Sajad Tabibi, and Raquel N. Buendía. “Comprehensive analysis of spaceborne GNSS reflectometry for precision altimetry". *Living Planet Symposium 2025, 23 - 27 June 2025, Vienna, Austria.*

C_3 - Alena Melic, Raquel N. Buendía, and Sajad Tabibi. “Cycle Slip Correction and Coherency Detection for Precision Altimetry Using Dual-Frequency GG-R Measurements". *IEEE GNSS+R 2025, April 23 – 25, 2025, Leiden, The Netherlands.*

Acronyms

AMSR2 Advanced Microwave Scanning Radiometer 2

ArcticDEM Arctic Digital Elevation Model

CASC Chine Aerospace Science and Technology Corporation

C/A Coarse/Acquisition

CDF Cumulative Distribution Function

CDMA Code Division Multiple Access

cGNSS-R conventional GNSS-R

CLS Collecte Localisation Satellites

CMEMS Copernicus Marine Environment Monitoring Service

CNES Centre National d'Etudes Spatiales

COMSAT COMmunications SATellite systems

CS Cycle-Slip

CSs Cycle-Slips

CYGNSS CYclone Global Navigation Satellite System

DDM Delay-Doppler Map

DEM Digital Elevation Model

DoD Department of Defence

DoT-1 Demonstration of Technology-1

DTU Technical University of Denmark

EASE Equal-Area Scalable Earth Grid

ECEF Earth-centred-Earth-fixed

ERS European Remote Sensing

ESA European Space Agency

ESR Earth and Space Research

FSSCat Federated Satellite System Cat

FM Flight Module

GFS Global Forecast System

GG-R Grazing angle GNSS-R

GIMs Global Ionospheric Maps

GL Geophysics Laboratory

GLONASS GLObalnaya NAvigatsionnaya Sputnikovaya Sistema

GMSL Global Mean Sea Level

GNSS-R GNSS-Reflectometry

GNSS Global Navigation Satellite System

GPS Global Positioning System

GPST GPS Time

GPT Global Pressure and Temperature

GRAALT GRazing Angle ALTimetry

I In-phase

IF Intermediate Frequency

iGNSS-R interferometric GNSS-R

ISRO Indian Space Research Organisation

LEO Low Earth Orbit

LHCP Left Hand Circular Polarization

LR Low Resolution

LTAN Local Time of Ascending Node

LTDN Local Time of Descending Node

L1A Level-1A

L1B Level-1B

L2 Level-2

L-band Long-band

MASAM2 MASIE-AMSR2

MASIE Multisensor Analyzed Sea Ice Extent

Mcps Mega chips/sec

MCS Master Control Station

MEO Medium Earth Orbit

MSS Mean Sea Surface

M-code Military-code

NASA National Aeronautics and Space Administration

NCEP National Centers for Environmental Prediction

NGA National Geospatial-Intelligence Agency

NOAA National Oceanic and Atmospheric Administration

NSF National Science Foundation

NWP Numerical Weather Prediction

OCS Operational Control Segment/System

OL Open-Loop

OLCI Ocean and Land Colour Instrument

OSU Oregon State University

RA Radar Altimetry

REMA Reference Elevation Model of Antarctica

RF Radio Frequency

RHCP Right Hand Circular Polarization

RMS Root Mean Square

RMSE Root Mean Square Error

RO Radio Occultation

ROI Regions Of Interest

RSA Reference Surface Adjustment

PARIS A PAssive Reflectometry and Interferometry System

PDO Pacific Decadal Oscillation

PGC Polar Geospatial Center

PNT Positioning Navigation and Timing

POD Precise Orbit Determination

PPS Precise Positional Service

PRETTY Passive REflecTometry and dosimeTrY

PRN Pseudo Random Noise

P-code Precise-code

Q Quadrature-phase

QC Quality Control

SAR Synthetic Aperture Radar

SD Standard Deviation

SIO Scripps Institution of Oceanography

SIRAL SAR Interferometric Radar Altimeter

SEAS Southeast Asian Seas

SLA Sea Level Anomaly

SLSTR Sea and Land Surface Temperature Radiometer

SMAP Soil Moisture Active Passive

SNR Signal to Noise Ratio

SoOp Signals of Opportunity

SP Specular Point

SPS Standard Positioning Service

SRAL Synthetic Aperture Radar Altimeter

SSH Sea Surface Height

SSO Sun-Synchronous Orbit

STRATOS Sophisticated Spire-engineered software-defined

SVN Space Vehicle Number

TEC Total Electron Content

TU Technical University

UHF Ultra-High Frequency

UK-DMC-1 United Kingdom-Disaster Monitoring Constellation-1

UK-TDS-1 United Kingdom-TechDemoSat-1

UL University of Luxembourg

UNB University of New Brunswick

UPC Universitat Politècnica de Catalunya

USD United States Dollar

UTC Coordinated Universal Time

VMF Vienna Mapping Function

VTEC Vertical Total Electron Content

WAF Woodward Ambiguity Function

WGS84 World Geodetic System 1984

Abstract

Conventional satellite-based altimetry, which relies on radar altimeters or microwave radiometers, achieves centimeter-level accuracy but is limited by spatial and temporal constrains, particularly in regions above and below approximately 80° latitude in the polar regions. In contrast, L-band GNSS signals reflected from the Earth's surface offer global coverage and can operate under all weather conditions. These signals can effectively fill the temporal and spatial gaps left by traditional satellite altimeters, addressing these limitations.

While reflected signals, or multipath, have traditionally been a challenge in GNSS Positioning Navigation and Timing (PNT) due to their potential to degrade measurement accuracy, they have proven to be a valuable resource for remote sensing. The study of these reflected signals, known as GNSS-Reflectometry (GNSS-R), demonstrates how an error source in PNT can be repurposed for a variety of applications, such as reconstruction of digital elevation models, altimetry, soil moisture estimation, and more.

This doctoral thesis explores the use of GNSS-R carrier phase measurements for altimetry retrieval across a variety of surface types worldwide, including oceans, sea ice, and ice sheets, with a particular focus on polar regions. The analysis used data from the Spire Global Inc. Grazing angle GNSS-R (GG-R) satellite constellation, providing a robust dataset to investigate the potential of dual-frequency GNSS-R altimetry at low elevation angles, ranging from 5° to 30°.

Key findings of this dissertation include altimetric results for ocean, sea-ice, and ice-sheet, with decimeter and meter precision for water and land reflections, respectively. This work comprehensively spans model formulation, software development, parameter opti-

mization, and validation against existing platforms and products. The development of the GRazing Angle ALTimetry (GRAALT) software enabled efficient processing and analysis of GNSS-R data, resulting in a refined Level-2 (L2) altimetry product derived from 113,765 GNSS-R tracks. This product achieved a SLA Root Mean Square Error (RMSE) of 16.8 cm with a standard deviation of 16.9 cm. Additionally, the L2 product includes parameters necessary for height recomputation, enhancing its flexibility and utility.

Keywords: GNSS, Reflectometry, GNSS-R, GG-R, Carrier phase altimetry, Ocean, Sea-ice and Ice sheet altimetry

Chapter 1

Introduction

Understanding Earth's dynamics plays an essential role in numerous scientific disciplines. Various remote sensing parameters, such as SSH, ice and sea-ice distribution, are crucial for climate change predictions. The first chapter of this dissertation outlines the motivation and objectives, introduces the main contributions, and concludes with an explainations of the structure of the dissertation.

1.1 Motivation and objectives

Earth remote sensing data is pivotal in analyzing various parameters, such as land cover changes [1], vegetation dynamics [2], atmospheric variations [3], and sea and sea-ice surface variations [4]. This information is essential for environmental monitoring, natural resource management, and disaster response. These branches, which are growing exponentially, are driven by the ongoing effects of climate change, which reply on constant data from various remote sensing variables. This is particularly critical in polar regions, which are some of the most dynamic and sensitive areas in terms of climate change [5, 6]. The accelerated melting of polar ice sheets and glaciers significantly impacts global sea-level rise, which endangers many coastal areas [7]. Additionally, remote sensing techniques are the key in assessing the effectiveness of conservation strategies and sustainable development initiatives [8].

Distinct platforms are used to monitor global environmental changes over time, providing vital geophysical information, such as satellites and aircraft. However, satellite-based remote sensing is the most widely used due to its broader coverage, whereas aircraft missions offer higher precision but lower revisit frequency. Additionally, producing similar data products with aircraft is far more expensive than using satellite data [9].

The extent of coverage and frequency of revisits of satellite revisits are essential for monitoring the evolution of the parameters in a given area. Nevertheless, active remote sensing satellites sometimes fail to meet the spatio-temporal needs, creating an opportunity for complementary techniques to emerge.

In recent decades, there has been growing interest among researchers in the use of Signals of Opportunity (SoOp) in remote sensing applications. SoOp refers to existing radio-frequency signals, such as Global Navigation Satellite System (GNSS), that were not originally intended for specific scientific or research purposes but can be repurposed for various applications. Since GNSS systems already exist, the cost of using these passive system to collect signals is significantly lower than that of active remote sensing satellites, making them an attractive complementary tool.

The use of the SoOp approach with reflected GNSS signals is called GNSS-R, and it has emerged as a promising complementary to traditional satellite remote sensing systems. Conventional radar and optical remote sensing often face limitations in spatio-temporal resolution and are hindered by specific conditions such as complex terrains, cloud cover (visual lost of Earth's surface), and vegetation, which can obscure the soil beneath. The main advantages of GNSS-R are:

- It operates effectively under all weather conditions, through above-ground vegetation, and over various surface types, with some penetration that can provide valuable insights into the Earth surface.
- It offers high temporal resolution, as it can collect multiple simultaneous reflections from different GNSS constellations, such as Global Positioning System (GPS), Galileo, and GLObalnaya NAvigatsionnaya Sputnikovaya Sistema (GLONASS).

- It can provide diverse surface parameters such as surface winds [10], soil moisture [11, 12, 13], ocean altimetry [14, 15], and ice sheet dynamics [16].
- Its operational costs are significantly lower than those of active remote sensing satellites, as GNSS-R are passive platforms. While the launch and operating costs of remote sensing satellites range from $100 million to several billion dollars [17], the cost of GNSS-R satellites can range from $1 million to few hundred million dollarsUnited States Dollar (USD) dollars [18, 19, 20].

.

Among the different environmental climate variables that can be monitored using GNSS-R, the observation of sea level variations, sea-ice distribution, and ice sheet thickness plays a critical role in understanding and predicting the impacts of climate change, particularly regarding sea-level rise. This need is addressed in this dissertation.

1.2 Contributions

The PhD thesis focuses on analyzing the GNSS-R signal to retrieve altimetric measurements in polar and ice-covered regions. Specifically, GNSS-R under GG-R geometries, where the signal is collected at low elevation angles and the carrier phase measurements are expected to be coherent (sufficient to retrieve high-precision altimetry retrievals) over smooth surfaces such as calm waters, ice and sea-ice.

The main contributions of this work are as follows:

- **Model formulation validation:** A validation of the model formulation, in which the regions and periods selected for this study were identified as the most suitable and stable for analyzing sea-ice covered areas. The specific area of focus is Hudson Bay, a large body of saltwater in northeastern Canada.
- **Monthly and seasonal comparison:** A monthly and seasonal comparison to analyze the correlation between ice concentration and the quality of the carrier phase GG-R measurements in the Hudson Bay area from January to October 2021.

- **Sea surface altimetry study:** A study using dual-frequency GNSS carrier phase measurements under GG-R for sea surface altimetry over the Java Sea, Indonesia. A total of 714 coherent profiles from January 2020 to October 2021 were used to retrieve the relative surface height from World Geodetic System 1984 (WGS84). Two methods were employed to remove the ionospheric delay: an ionosphere-free combination and frequency-specific correction based on dual-frequency carrier phase observations.

- **Parametrization analysis:** An analysis of different variables in the model formulation's parametrization, such as the reference surface model, the tropospheric model, and the use of different frequency-specific filters. This section also includes improvement in the detection and correction of cycle-slips.

- **Comparison with traditional radar altimetry:** A comparison between GG-R altimetry measurements and traditional radar altimetry data, including Sentinel-3A/3B, Saral, and Cryosat-2. The analysis spans from May 2019 to October 2021 and explores whether the GG-R technique can complement existing satellite altimetry data.

- **Ice sheet altimetry:** Altimetry measurements over land ice-covered regions (Greenland and Antarctica), with approximately 7800 coherent segments processed over a nine-month period. Different Digital Elevation Model (DEM) datasets were used for the relative height adjustment and to validate the GG-R retrievals. The results demonstrate the potential of dual-frequency GG-R for measuring ice sheet surface heights.

- **GRAALT software:** Additional content on the final data product and a software tool specifically developed to support the continuation and use of the data processing in this research.

1.3 Overview

This thesis is organized into six main chapters.

Chapter 2 introduces GNSS systems and their evolution, detailing their application in GNSS-R. It explains the principles of signal reflection and the factors affecting coherence, such as surface roughness and the Fresnel zone. Applications of GNSS-R in altimetry, wind monitoring, and cryosphere studies are discussed, along with a review of existing GNSS-R missions, such as CYGNSS and their contributions. Future opportunities and enhancements in GNSS-R methods are also explored.

Chapter 3 develops methodologies for retrieving altimetry measurements using low-elevation GNSS-R signals. It addresses challenges such as phase ambiguity, atmospheric delays, and reference surface modeling. Dual-frequency approaches are applied to correct ionospheric delays. Model validations are performed using data from selected regions like Hudson Bay. The results highlight the feasibility of GNSS-R altimetry achieving decimeter-level accuracy.

Chapter 4 focuses on GNSS-R altimetry over oceans and sea ice, using Hudson Bay as a case study. Seasonal data comparisons are made to analyze the correlations between ice concentration and measurement coherency. Enhanced ionospheric correction models are proposed to improve accuracy. A comparison between GNSS-R and traditional satellite altimetry systems is presented, highlighting complementary advantages. The chapter concludes with parameter refinements for GG-R altimetry models.

Chapter 5 explores GNSS-R applications for measuring ice sheet elevation in polar regions. Thousands of coherent tracks over Greenland and Antarctica are processed. The analysis validates the effectiveness of GNSS-R against digital elevation models like Arctic Digital Elevation Model (ArcticDEM) and Reference Elevation Model of Antarctica (REMA). Challenges related to collocated height retrievals and segment coherency are addressed. This chapter highlights GNSS-R's potential to fill gaps left by traditional satellite altimeters.

Chapter 6 describes the development of the GRAALTv1 software for processing GNSS-R data and introduces the Level-2 (L2) data product. The software is validated using datasets

from multiple regions, demonstrating significant improvements in sea level anomaly measurement accuracy. GRAALT aims to facilitate future research by offering a robust toolset for GNSS-R data analysis. The chapter concludes by emphasizing the global applicability of these advancements.

The final chapter of this thesis, dedicated to the conclusions, summarizes the key findings, results, and outlines directions for future work.

Chapter 2

Global Navigation Satellite Systems Reflectometry (GNSS-R)

This chapter, titled GNSS-R, includes a detailed discussion of different GNSS constellation and signals, with a specific focus on the GPS constellation. It provides an overview of the principle of GNSS-R and its methodologies, concluding with a section dedicated to Grazing angle GNSS-R (also referred to as GG-R), a type of GNSS-R technique for retrieving altimetry measurements.

2.1 Global Navigation Satellite Systems (GNSS)

Global Navigation Satellite Systems (GNSS) refers to a constellation of satellites transmitting Long-band (L-band) signals from space. these signals provide positioning and timing data to GNSS receivers, enabling them to determine its location. The first fully operational GNSS was the US GPS, initially developed for military purposes but opened for civilian use in 1983. While GPS remains the most widely used GNSS, other nations have developed their own systems, such as the Russian GLONASS, the European Galileo, and BeiDou operated by the People's Republic of China.

These systems share common frequency bands to prevent mutual interference. Figure 2.1 shows the frequency signal emitted by GPS, Galileo, GLONASS, and BeiDou, along

with their associated codes and spectrum - a GNSS signal features described in the following section.

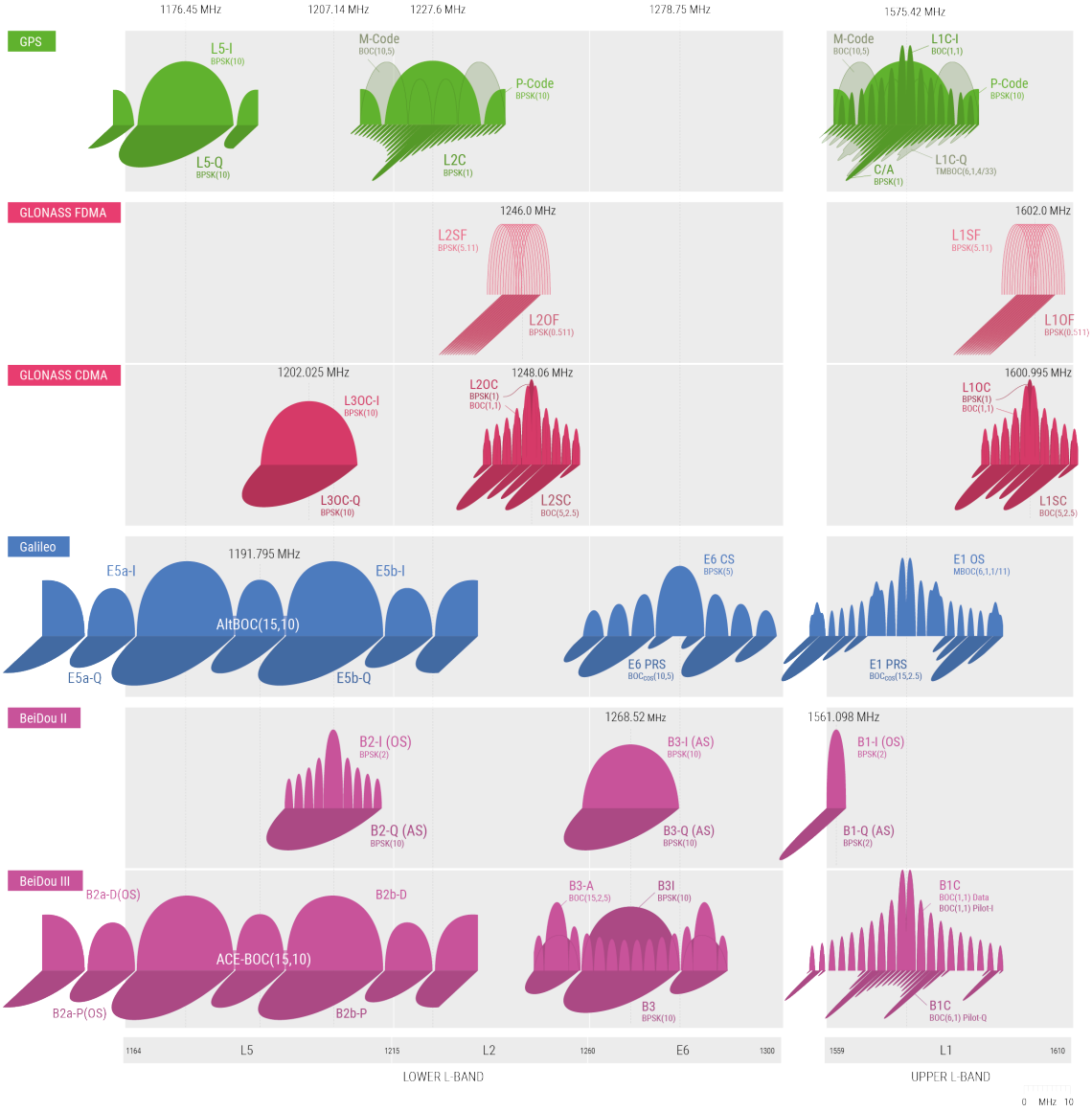

Figure 2.1: GPS, Galileo, GLONASS and BeiDou frequencies and spectrum [21]

The key advantage of GNSS signals for PNT and remote sensing lies in their passive nature. Receivers do not need to actively interact or communicate with satellites. Like broadcast radio or television, GNSS functions as a one-way communications sys-

tem (COMmunications SATellite systems (COMSAT)) that allows for an unlimited number of users.

GNSS satellites are equipped with highly accurate atomic clocks, which are fundamental to their precision. A receiver determines its position by measuring the time taken for a signal to travel from the satellites to the receive. By multiplying this transmission time by the speed of light, the distance between the satellite and receiver is calculated. To determine a user's position, at least three satellite distance measurements are required, a process known as trilateration. However, because receivers typically do not use atomic clocks, an additional measurement from a fourth satellite is necessary to calculate the time difference between the receiver's clock and the satellites' clocks. This enables the receiver to solve for four unknowns: latitude, longitude, altitude, and time. In addition to the pulses in the signals that enable time-of-arrival measurements, satellites also transmit a binary data message. This message, part of a one-way COMSAT system, contains the satellite's location and other essential parameters needed by the receiver to calculate its position accurately.

2.1.1 Signal's data

Most satellites in the GNSS constellation transmit at least **two types of different data**: **observation data** and **navigation data**, both of which are essential for accurate positioning.

Observation data: Observation data is transmitted every millisecond and consists of: **pseudorange** and **Pseudo Random Noise (PRN) number**, **carrier-phase** and **time**.

The **pseudorange** (ranging code) and **PRN number** are key components of this data. Each satellite transmits a unique code, known as a Pseudo-random code, that enablesGNSS receivers to identify and differentiate between satellites. Receivers use two critical aspects of these signals: (1) the specific sequence emitted by each satellite, which allows the receiver to associate the sequence with the satellite's unique PRN number, and (2) the timing pattern of the transmitted signal, which enables the receiver to match the satellite's signal sequence in real time. By correlating the received GNSS signal (adjusted to baseband and Doppler-corrected) with modeled replicas of these codes, the receiver can estimate the time difference between signal transmission and reception. Multiplying this time difference by the

speed of light yields **pseudorange** or **code** between the satellite and receiver.

This technique, known as Code Division Multiple Access (CDMA), relies on pseudo-random codes with excellent auto-correlation properties (a peak when aligned, with a consistent decay otherwise) and minimal cross-correlation between different codes (orthogonal behavior). The length and rate of a PRN code determine how effectively a signal can be acquired and tracked in the presence of noise and interference[22].

The **carrier-phase**, which represents the carrier Radio Frequency (RF) sinusoidal signal is another observation parameter. The PRN code is modulated onto the carrier signal, which depends on the transmission frequency. Similar to pseudorange measurement, the carrier-phase can be correlated with a replica signal to achieve a highly accurate distance measurement. However, carrier-phase measurement are more complex and sensitive, requiring high-quality receivers and favorable environmental conditions for reliable results.

The **observation time** refers to the reading of the receiver clock at the moment the code and/or the carrier-phase measurements are valid.

Navigation data: Navigation data is more extensive and takes 12.5 minutes to broadcast a complete message. The nformation in the navigation message is divided into the following components: **time** and **clock** corrections, **satellites health** status, **ionospheric** corrections, and **ephemeris** and **almanac** data.

2.1.2 Data corrections

The GNSS **time** parameters and **clock** corrections are used to compute satellite clock offsets and perform time conversions. These corrections also include satellite health information, which identifies valid navigation datasets, and ionospheric models for single frequency receivers.

The **ephemeris** data provides precise satellite orbit and clock parameters, essential for short-term positioning. This high-resolution orbital information enables accurate satellite coordinate estimation and is updated every 2 hours.

The **almanac** data contains coarse satellite orbit information, which support long-term tracking and receiver initialization. It includes the status and low-resolution orbital informa-

tion of all satellites and is updated every 6 days, enabling the computation of approximate positions for most GNSS satellites.

Without both types of data, GNSS receivers cannot perform positioning calculations. These represents the **minimum information required** to determine the receiver's position using data from at least four different satellites. When positioning is performed using observation and navigation data alone, without additional corrections or augmentations, and relying only on pseudorange measurement, the positioning mode is referred to as Standard Positioning Service (SPS).

2.2 Global Positioning System (GPS)

GPS was the first GNSS to provide PNT services globally, becoming fully operational in April 1995. The GPS constellation nominally consists of at least 24 geometrically spaced slots (4 satellites per each of the 6 orbit planes), with each slot containing at least one operational satellite. Each satellite is identified by a two-character code: a letter designating the orbital plane (A through F) and a number identifying the satellite within the orbital plane (1 through 4 in the baseline constellation). In practice, the system supports a constellation of more than thirty satellites in orbit [23].

The GPS satellites are not equally spaced within their orbital plane. The six orbital planes are inclined at 55° and separated by 60° in the ascending node. Satellites orbit at an altitude of approximately 20.560 km in a nearly circular Medium Earth Orbit (MEO), corresponding to an orbital period of 12 sidereal hours. Consequently, a satellite will appear in the same position in the sky 4 minutes earlier each day. This arrangement ensures that at least the minimum four satellites required for positioning are always visible. Satellite coverage, or the number of satellites in view, is a crucial factor in improving PNT accuracy [24].

Each GPS signal consists of three components:

- **Carrier**: A RF sinusoidal signal transmitted in three different UHF bands: L_1 (1575.42 MHz), L_2 (1227.6 MHz), and L_5 (1176.45 MHz).
- **Ranging code**: Binary sequences known as PRN codes, which are associated with

either SPS or Precise Positional Service (PPS). These codes possess mathematical properties that allow multiple satellites to transmit on the same frequency without interfering with one another. In the GPS frequency bands, signals are transmitted in both the in-phase and quadrature components. For example, as illustrated in 2.1, the L_1 band includes the Coarse/Acquisition (C/A) code, Military-code (M-code), and Precise-code (P-code) encrypted with the Y-code (P(Y)), as well as L_1C-I and L_1C-Q signals. Similarly, the L_2 band includes the M-code, P-code in-phase and L_2C in quadrature. Finally, the L_5 band provides L_5-I and L_5-Q signals, primarily intended for civilian users requiring precise positioning, with characteristics comparable to the P(Y)-code.

- **Navigation data**: A binary-coded message that includes satellite health and status, precise ephemeris data (satellite position and velocity), clock bias parameters, and an almanac providing reduced-precision ephemeris data for all satellites in the constellation[23].

GPS provides two levels of services:

- **Standard Positioning Service** (SPS) for civilian use, as introduced in the previous section.
- **Precise Positioning Service** (PPS) encrypted for military purposes or authorized users, such as the Department of Defence (DoD) [1] [23].

To provide those levels of service, each GPS satellite transmits two types of ranging codes: the C/A for SPS and the M and P(Y) codes for PPS. These signals incorporate cryptographic techniques, which means that with the appropriate decryption keys the authorized users decrypt them, that techniques, requiring decryption keys for access This approach, known as Anti-Spoofing, prevents unauthorized interference, such as spoofing, which could overpower the weak GNSS signals and cause a loss of positioning.

The C/A code is a unique sequence of 1023 bits with a repetition period of 1 ms. This results in a chip-duration of $\sim 1\mu$s (equivalent to a wavelength of $\sim$ 300 m), with a chip-rate

[1] The U.S. DoD oversees the provision of PPS, adhering to international GNSS standards.

of 1023 MHz or Mega chips/sec (Mcps). In contrast, the P-code has a much longer repetition period of one week ($\sim 10^4$ chips) with a chip chip-duration of $\sim$ 30 m and a chipping rate of 10.23 Mcps. The higher chipping rate of the P-code provides greater precision in range measurements compared to the C/A-code.

The direct sequences used for broadcasting SPS GPS signals include the L_1 C/A, L_1C, L_2C, and L_5 signals.

Table 2.1 presents the features of both current and future generations of GPS satellites, including Block IIA (2nd generation, "Advanced"), Block IIR ("Replenishment"), Block IIR-M ("Modernized"), Block IIF ("Follow-on"), GPS III, and GPS IIIF ("Follow-on").

Table 2.1: Current and Future GPS Generations [25]

	Legacy Satellites		**Modernized Satellites**		
	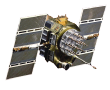	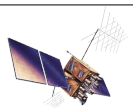	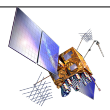		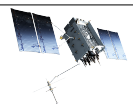
Block	**IIA**	**IIR**	**IIR-M**	**IIF**	**III/IIIF**
Operational satellites	0	6	7	12	6
Year design lifespan	7.5	7.5	7.5	12	15
Launched in...	1990-1997	1997-2004	2005-2009	2010-2016	2018-2023

The GPS Operational Control Segment/System (OCS) monitors its satellites and tracks the quality of their signals in order to provide information about the reliability. The control segment includes several key components: a Master Control Station (MCS) located in Colorado Springs, Ground Antennas for communication with the satellites in Ascension Island, Diego García, Kwajalein Atoll, and Cape Canaveral, as well as Monitoring stations spread across 16 global locations.

The global coordinate frame used by GPS is WGS84, a reference system for mapping and navigation developed by National Geospatial-Intelligence Agency (NGA). Another important parameter is time; while Coordinated Universal Time (UTC) is the most widely used reference time worldwide, GPS uses the GPS Time (GPST), which measures the number of seconds since midnight on January 6, 1980.

2.3 Global Navigation Satellite System - Reflectometry (GNSS-R)

This section introduces the concept of GNSS-R starting with its historical development, followed by an explanation of the basic principles, and concluding with a discussion on GNSS-R missions and future directions.

2.3.1 History

The idea of using GNSS-R signals first emerged in 1988 [26], primarily for monitoring ocean winds. In 1993, the A PAssive Reflectometry and Interferometry System (PARIS) concept was proposed for altimetry purposes using a technique known as interferometric GNSS-R (iGNSS-R) [27]. A few years later, conventional GNSS-R (cGNSS-R) (the most commonly used technique in GNSS-R) was proposed by [28]. In 1997, the first airborne experiment was conducted, demonstrating the effects of sea surface roughness on GNSS-R measurements and providing the first ocean surface wind demonstration [29]. Following several prove-of-concept experiments, the first theoretical model was developed in the early 2000s [30].

The first dedicated GNSS-R mission was United Kingdom-Disaster Monitoring Constellation-1 (UK-DMC-1), a Low Earth Orbit (LEO) satellite launched in 2003 to collect reflections and measure ocean surface roughness [31]. After this successful mission, the United Kingdom-TechDemoSat-1 (UK-TDS-1) was launched in 2014, collecting reflections for many various observation applications, including oceans, land, and ice [32], the next major mission, CYclone Global Navigation Satellite System (CYGNSS). Launched in December 2016 and still operational (as of the publication of this dissertation), was initially designed to track tropical cyclones. However, CYGNSS observations have also been used for multiple applications, similar to its predecessor, UK-TDS-1 [33, 34, 35, 36].

2.3.2 Basic principles

GNSS-R is a technique that uses L-band signals from GNSS in a bistatic configuration. The L-band for GPS refers to the frequency range used by GPS satellites to transmit signals, specifically around 1.2 GHz (L2) and 1.5 GHz (L1). In a bistatic configuration, the signal

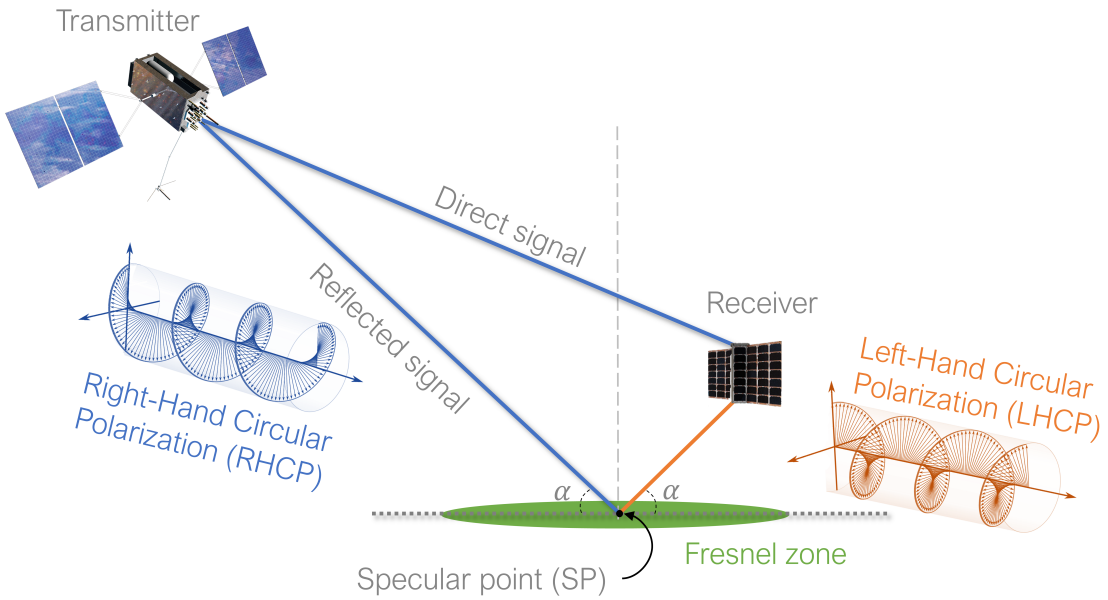

Figure 2.2: GNSS-R signal reflection from the transmitter to the reflection point SP and then to the receiver. The angle α represents the elevation angle from the tangent plane to the transmitter/receiver from the SP.

travels from the transmitter to the Earth's surface and is then collected by the receiver. The reflected signal provides crucial data from the reflection point. The direct signal from the transmitter is also important, as the differences between the reflected and direct signals are key to retrieving the information. The two signals can be distinguished because the reflected signal undergoes a change in polarization after the reflection from Right Hand Circular Polarization (RHCP) to Left Hand Circular Polarization (LHCP) for elevation angles above 30 degrees (Figure 2.2).

In principale, the signal reflection takes the shortest path from the transmitter to the receiver, i.e., the same elevation angle from the reflection point (SP) as shown in Figure 2.2. However, after the reflection, the signal scatters, which can affect its quality and power upon reception. The scattering occurs in a region known asthe glistening zone, which depends on surface characteristics such as roughness, soil moisture, and the elevation angle, as well as the wavelength of the signal.

Reflections from smooth surfaces, such as calm water, ice, or sea-ice, produce strong reflections, and the size of the glistening zone is reduced. When the glistening zone is smaller than half the wavelength of the transmitted signal, the phase component is considered coherent. This region around the specular point is called the Fresnel zone, as illustrated in Figure 2.2.

For the coherent scattering, the power of the signal,P_c, is represented by the bistatic equation [37]:

$$P_c = \frac{P_t G_t \lambda^2}{(4\pi)^3 (R_{ts} + R_{sr})^2} G_r V_F, \tag{2.1}$$

where $P_t G_t$ is the transmitter's Effective Isotropic Radiated Power, G_r is the receiver antenna gain pattern, V_F is Fresnel reflection coefficient, λ is the wavelength of the signal, R_{ts} and R_{sr} are the distances between the nominal specular point and the transmitter/receiver, respectively.

For scattering beyond the Fresnel zone (non-coherent or diffuse scattering), the bistatic radar equation becomes more complex. In this case, the diffuse scattering power, (P_d), can be computed as [30]:

$$P_d = \frac{P_t G_t \lambda^2}{(4\pi)^3} T_i \iint \frac{G_r}{R_{ts}^2 R_{sr}^2} \chi^2(\Delta\tau, \Delta f_D) \sigma_{pq}^0 dA \tag{2.2}$$

where T_i is the coherent integration time, χ is the Woodward Ambiguity Function (WAF), Δf_D is the Doppler shift, A is the effective scattering area, and σ_{pq}^0 is the scattering coefficient, representing the strength of the signal scattered from a given point on the surface toward the receiver.

From Equation 2.2, one of the most commonly used data products in GNSS-R can be derived: the Delay-Doppler Map (Delay-Doppler Map (DDM)).

The DDM is generated by cross-correlating the received signal with a local replica of the time delay from the transmitter to the SP, and the Doppler shift caused by the relative motion between the transmitter and receiver [37]. Figures 2.3 show two examples of DDM: on the left, a coherent scattering and on the right, diffuse or incoherent scattering. The analogy is

illustrated with moonlight reflections on a smooth surface (lake) and a rough surface (sea).

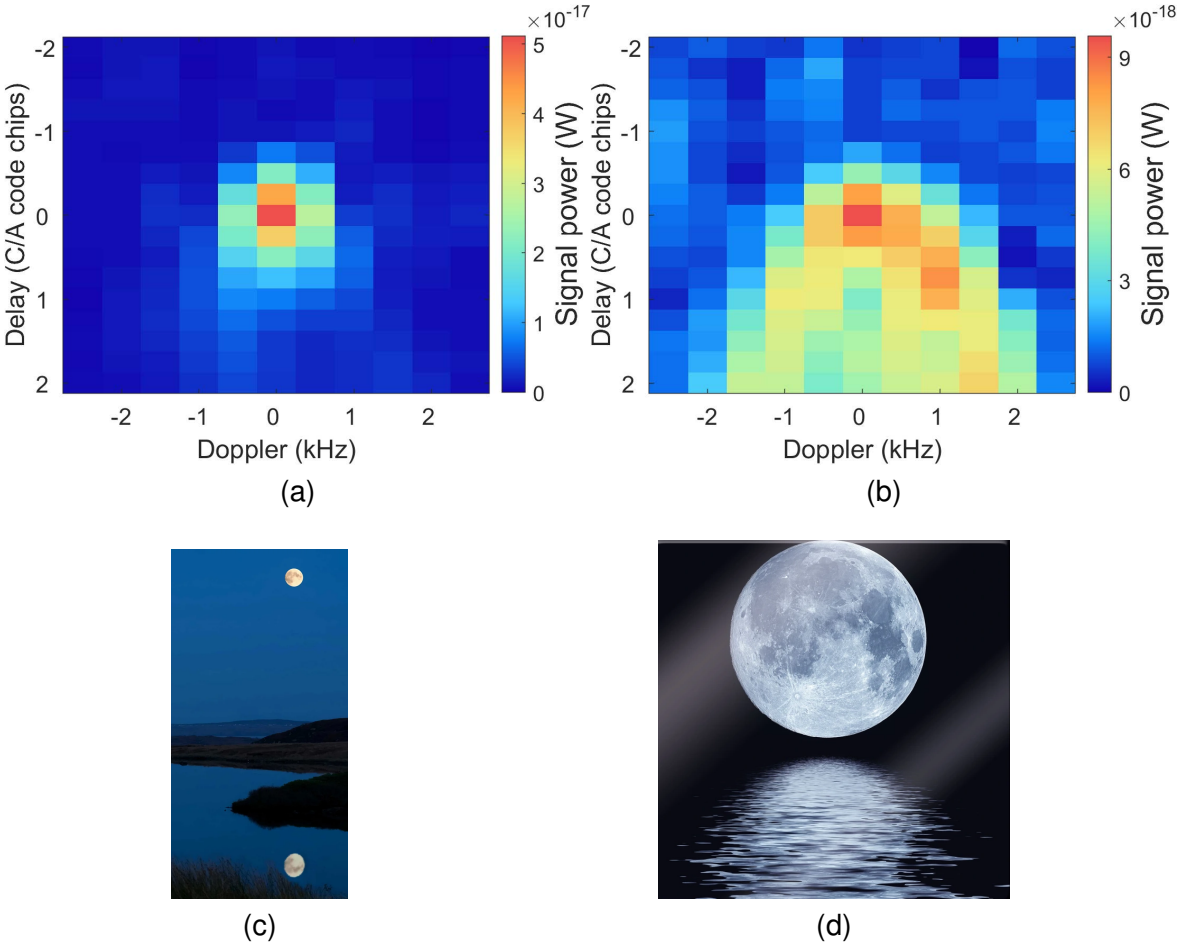

Figure 2.3: (a) Coherent and (b) incoherent DDM extracted from CYGNSS mission, with analogy of moonlight reflections on a lake (smooth surface) and on the sea (rough surface).

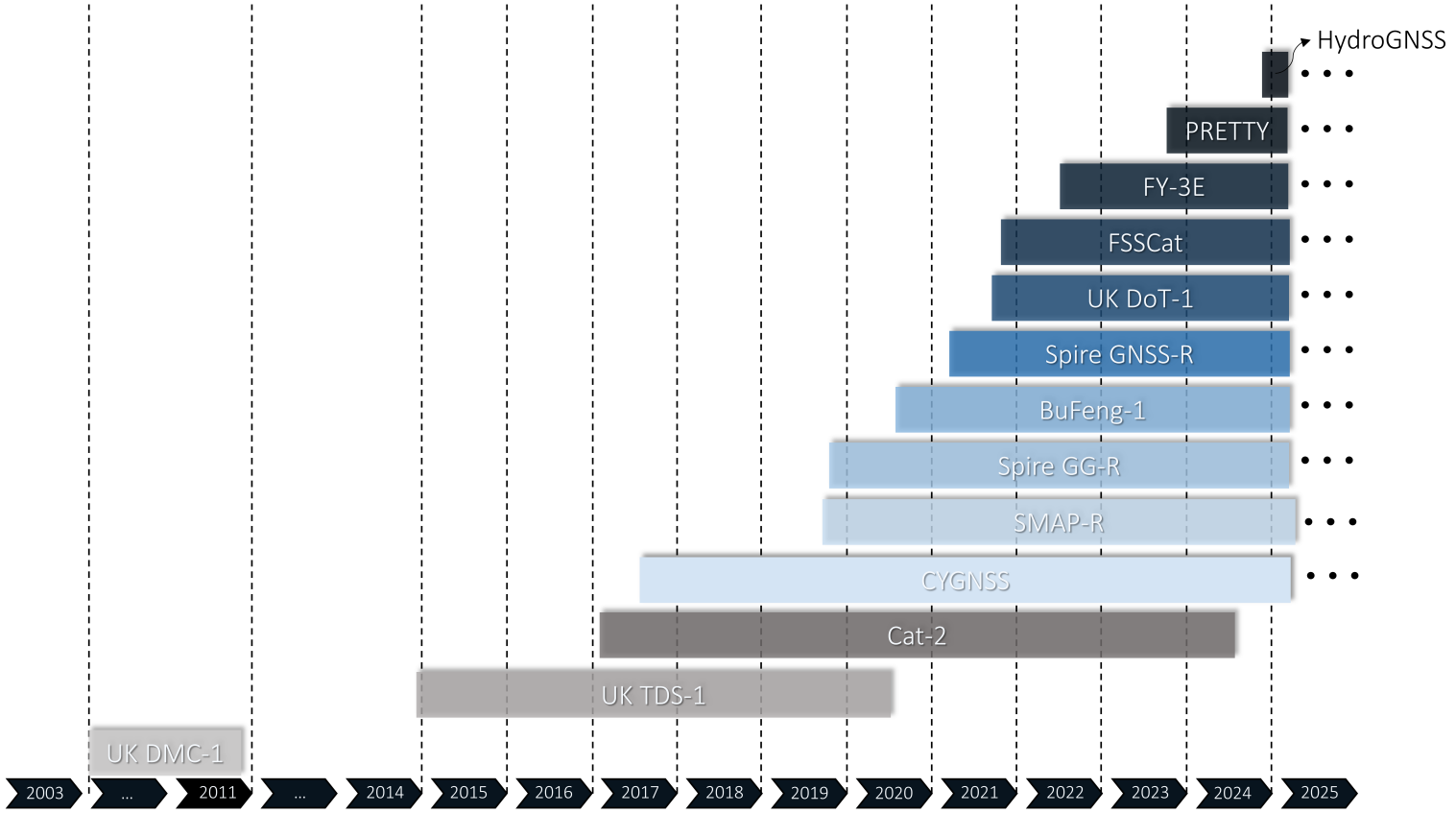

Figure 2.4: Most relevant GNSS-R missions and their year launch years.

2.3.3 Differences on low and high elevation angle range

The angle at which these signals reflect greatly influences the techniques to be applied, as well as the characteristics of the signal in its reflection.

For grazing angles, that is, high incidence angles often above 70° relative to the surface in the SP, the reflection geometry is actually one in which the reflected signal path is almost parallel to the surface. They are more coherent in nature (depending on surface characteristics), keeping phase information, and mostly analyzed using coherent reflectometry techniques. Here, the reflected signal has very strong phase information, enabling applications in altimetry, such as sea surface height and ice topography measurements. At these grazing angles, the reflected signal is mainly RHCP, thereby reflecting off the surface with minimal polarization inversion.

On the other hand, at incidence angles lower than this, say below 70°, the reflection becomes more diffuse, scattering energy in many directions rather than in a coherent beam. In this case, the received signal is mostly analyzed using incoherent reflectometry techniques where one considers the signal power instead of phase. These geometries and technique are mostly used for soil moisture and vegetation monitoring. The reflection causes a rotation of the polarization that transforms in its reflection from RHCP into LHCP, as shown in Figure 2.2. The transition between these two regimes affects the antenna polarization selection and processing algorithms in system design.

2.3.4 Current applications & missions

GNSS-R has become a versatile and prominent remote sensing technique, with a wide range of applications in various fields such as oceanography, land monitoring, and cryospheric studies.

Ocean Applications: GNSS-R has proven particularly effective in ocean altimetry, providing key information on sea surface height [14, 15], wind speed [33, 38], and wave dynamics [39, 40]. These measurements are critical understanding climate change impacts, particularly sea-level rise. The National Aeronautics and Space Administration (NASA) CYGNSS

mission, initially designed to monitor tropical cyclones, has been instrumental in retrieving surface wind speeds and improving hurricane models using GNSS-R.

Land and Cryosphere Applications: On land, GNSS-R shown significant utility in mapping soil moisture [11, 12, 13], monitoring vegetation biomass [2], and studying wetlands. It has also demonstrated great promise in flood detection [41], with GNSS-R signals distinguishing flooded and dry areas based on the strength of the reflected signals. In polar regions, GNSS-R is used to study ice sheet thickness [16] and sea ice extent [42], offering valuable insights into the dynamic processes affecting polar ice sheets. The TechDemoSat-1 mission, for example, contributed to generating digital elevation models of Greenland and Antarctica [16].

The most prominent GNSS-R missions are summarized in Figure 2.4. Notable missions include UK-DMC-1 and UK-TDS-1, which were to successfully employ GNSS-R for various Earth observation applications. The CYGNSS mission, initially designed to track tropical cyclones, has since expanded its applications to oceanographic and atmospheric studies. Prior to CYGNSS, the first GNSS-R CubeSat mission, conducted by Universitat Politècnica de Catalunya (UPC) NanoSat-Lab, demonstrated the capabilities of GNSS-R by collecting data using both iGNSS-R and cGNSS-R techniques. The mission was decommissioned in late 2023, and was followed by Federated Satellite System Cat (FSSCat), launched in September 2020 as a new version of the previous Cat spacecraft family.

Soil Moisture Active Passive (SMAP) mission started its operational phase in April 2015, with its prime mission phase completing in 2018. Since then, it has been reconditioned and renamed SMAP-reflectometry, where it has contributed to soil moisture monitoring and other land features assessments [43].

In late 2019, Spire Global Inc. successfully reconfigured its Radio Occultation (RO) satellites to collect GG-R data. About a year later, they launched their own dedicated GNSS-R satellites, designed to measure reflections and expanding the mission's scope to new GNSS-R applications.

From China, two key missions have contributed to GNSS-R data collection. The Bu-Feng-1 A/B mission, launched in 2019 by Chine Aerospace Science and Technology Corpo-

ration (CASC), focuses primarily on measuring reflections from BeiDou constellation. The FY-3E mission, launched in 2021, contributes additional GNSS-R data for atmospheric and land applications.

The UK Demonstration of Technology-1 (DoT-1) is a test designed to demonstrate the functionality of the buses for the upcoming European Space Agency (ESA) HydroGNSS mission, which will consist of two identical satellites dedicated to measuring soil moisture retrievals.

Finally, the ESA Passive REflecTometry and dosimeTrY (PRETTY) mission, launched in October 2023, is a 3-unit CubeSat specifically designed for ice and sea height measurements. This mission is expected to achieve ocean altimetry with a precision better than 50 cm [44].

2.3.5 Future directions

GNSS-R technology continues to evolve with exciting developments on the horizon. Key future trends include:

Multi-GNSS Constellations: The rise of multi-GNSS constellations (including Galileo and BeiDou) is expected to enhance GNSS-R'sperformance. By using signals from multiple satellite systems, GNSS-R will benefit from increased observations frequency, improved spatial resolution, and more reliable temporal coverage [15].

New Applications: GNSS-R applications is significant. Upcoming possibilities include detecting natural hazard such as detecting landslides, tsunamis, and even earthquakes. Subtle changes in reflected GNSS signals may provide early warning signs for these disasters. Moreover, GNSS-R may be extended to more specialized polarimetric applications in areas like dense vegetation or the cryosphere [45].

Integration with Other Remote Sensing Technologies: GNSS-R is increasingly being integrated with other remote sensing technologies, such as Synthetic Aperture Radar (SAR) and optical sensors.This integration will enable more comprehensive understanding of Earth's processes, particularly in complex environments like forests, wetlands, and ice-covered regions [45].

Chapter 3

Altimetry retrieval using Grazing Angle GNSS-R (GG-R) measurements

Satellite altimetry has made significant advances, achieving centimeter-level precision in measuring Earth's surface elevations [46]. However, as previously mentioned, existing operational satellite altimetry systems, despite their commendable performance, still face limitations in spatial and temporal resolution. This is where the value of GNSS-R becomes apparent, offering a unique opportunity to address data gaps that conventional satellite altimetry cannot file. This is especially relevant in regions demanding higher-resolution data, such as the Polar Regions, where satellite altimeter coverage does not extend beyond 81° latitude. The inherent challenges of the Polar Regions, including dynamic ice sheet changes and complex sea-ice conditions, necessitate higher-resolution measurements for accurate monitoring and a deeper understanding of these critical areas. By integrating GNSS-R data with existing remote sensing technologies, researchers and operational agencies can enhance their understanding of Earth's changing environments, improve weather forecasting, and support a wide range of environmental and disaster management efforts.

The GNSS-R measurements used in this study were collected by Spire Global Inc. graz-

ing angle satellite constellation. This constellation consists of more than 25 satellites initially designed for RO applications, which has been reprogrammed to also collect reflected signals under grazing angle geometries.

Grazing angle GNSS-R, also referred to as GG-R geometries, involves the collection of reflected signals at low elevation angles, typically ranging from 5 to 30 degrees. In this geometry. In this configuration, the characteristics of the received signal suggest minimal penetration into the Earth's surface, as indicated in prior research [14]. This property is essential for ensuring that the signal primarily reflects from the Earth's surface rather than deeper layers.

This chapter introduces the GG-R data measurements, model formulation, and the error and correction methods applied to obtain altimetry retrievals using GG-R measurements. Among the most prevalent corrections applied to the signal are phase ambiguity correction, ionospheric and tropospheric delay, and reference surface adjustment, each of which is discussed in a dedicated section.

3.1 Data measurements

The data used in this dissertation is sourced from a fleet of Spire CubeSats, also known as Flight Module (FM), designed to observe grazing angle reflections of GNSS signals. These CubeSats were launched across five distinct events and positioned in orbits with altitudes ranging from 500 to 585 km, as outlined in Table 3.1. Their orbits include Sun-Synchronous Orbit (SSO) configurations with an inclination of 97.5°, as well as Local Time of Ascending Node (LTAN) / Local Time of Descending Node (LTDN) parameters. Although the primary mission of the FMs focused on collecting RO measurements to derive atmospheric profiles (refractivity, temperature, and bending angle) they have successfully reprogramming to support grazing angle GNSS-R measurements [14].

Each FM is equipped with Sophisticated Spire-engineered software-defined (STRATOS), an advanced software-defined radio payload developed by Spire. The STRATOS system consists of three antennas: two limb-facing antennas and one zenith-oriented antenna. The

Table 3.1: Spire CubeSats orbit types and deployment dates used in this dissertation

FM name	Orbit type	Altitude (km)	Date deployed
FM079	SSO (11:15 LTAN)	585	February 2018
FM084	51.6°	445	"
FM085	"	"	"
FM086	85°	500	November 2018
FM087	"	"	"
FM088	"	"	"
FM099	SSO (09:30 LTAN)	505	April 2019
FM100	"	"	"
FM101	"	"	"
FM102	"	"	"
FM103	SSO (15:05 LTAN)	530	July 2019
FM104	"	"	"
FM105	"	"	"
FM106	"	"	"
FM108	"	"	"
FM113	"	"	"
FM116	SSO (LTDN 10:30)	540	September 2020
FM118	"	"	"
FM120	"	"	"
FM121	"	"	"
FM122	"	"	"
FM124	"	"	"
FM125	"	"	"
FM115	37°	550	"
FM117	"	"	"
FM119	"	555	"
FM128	"	"	"
FM129	"	"	"

limb-facing antennas, employing RHCP, capture the In-phase (I) and Quadrature-phase (Q) data. This data undergoes onboard processing and is downlinked at a frequency of 50 Hz. The phase component is derived relative to a modeled value obtained through Open-Loop (OL) tracking of dual-frequency reflected and direct signals between the transmitter and receiver. Meanwhile, the zenith-oriented antenna collects closed-loop dual-frequency phase and pseudorange measurements from six or more GNSS satellites simultaneously.

hese measurements, output at a frequency of 1 Hz, facilitating subsequent post-processing for Precise Orbit Determination (POD) solutions.

The main differences between OL and closed-loop processing methods are as follows:

(1) In OL model, the receiver processes both direct and reflected GNSS signals without continuous feedback adjustments. Instead, reflected signals are analyzed using a fixed or predicted model, where parameters like code delay and Doppler shift are estimated through cross-correlation with known satellite codes. This method is suitable for weak and noisy signals but does not update the tracking model based on real-time signal variations.

(2) In contrast, closed-loop GNSS-R signal processing involves continuous feedback from the received signals. The receiver dynamically adjusts its internal model in real-time by tracking changes in phase, frequency, and time delay. This iterative feedback loop enables more precise tracking and accurate measurement of small variations. However, it requires strong signal reception and higher computational resources due to the constant updates to the tracking model.

Data downlinking is achieved through Ultra-High Frequency (UHF) and S-band communication, enabling connectivity with a global ground station network exceeding 30 stations strategically distributed across all continents, including Antarctica. Once the data is downlinked, Spire produces two first level products: (1) Level-1A (L1A) Spire data product contains the 50 Hz timestamps and OL I/Q values of the reflected signal, along with other additional information about the antenna's performance and configuration. (2) Level-1B (L1B) product provides a more comprehensive range of parameters [47] (Table 3.2):

- Residual phase and SNR are computed using Equations 3.1 and 3.2.
- Pseudorange is estimated based on the early and late SNR values.
- SP location, along with its azimuth and elevation angles, is approximated using the positions of the receiver and transmitter .
- Received timestamps are corrected for receiver clock errors. For dual-frequency GPS signals, the OL values corresponds to those of the L_1 reflected signal. Consequently,

Table 3.2: List of L1B Spire data variables and their description

Variables	**Description**	**Units**
Tap	Flag to determine the quality of the data (not coherency)	Unit-less
Course time	Time of GNSS measurement (1 Hz)	seconds
Time	Time of GNSS measurement (50 Hz)	seconds
Residual phase	Signal residual phase (wrapped)	radians
Phase (OL model)	Signal OL model	meters
Pseudorange	Signal Pseudorange	meters
Signal to Noise Ratio (SNR)	Signal to Noise Ratio	V/V
Specular point location	Specular point latitude and longitude	degrees
Specular point angles	Specular point elevation and azimuth angles	degrees
Relative geometric delay	Reflected minus Direct Geometric delay on WGS84	meters
Transmitter position	Transmitter x,y,z components in Earth-centred-Earth-fixed (ECEF)	meters
Receiver information	Receiver x,y,z components in ECEF, the velocities, the clock errors, attitude quaternion, angle between the SP and the antenna (off-boresight) and azimuth angle between the SP and antenna boresight	meters meters/second seconds unit-less degrees degrees

the residual phase and SNR for direct L_1 and direct/reflected L_2 are interpolated to these timestamps.

- Receiver and transmitter positions, as well as attitude information, are interpolated to the Coarse time (1 Hz).

$$\phi_{residual} = \textit{atan2}(I, Q), \tag{3.1}$$

where I is the in-phase of the reflected or direct signal, and Q is th quadrature-phase component of the reflected or direct signal.

$$\textit{SNR} = \frac{\sqrt{S_R(I^2 + Q^2)}}{N_f}, \tag{3.2}$$

where S_R is the sampling rate, which in this case is 50 Hz, and N_f represents the noise floor, dependent on the tracked signal.

The next level of product after the previously described level is Level-2 (L2) [48], which represents the altimetry product. To produce L2 data, the L1B data must to be processed, and specific models need to be applied, as detailed in the following section.

3.2 Model formulation

The height above the WGS84 ellipsoid is primarily determined by the difference between the direct signal path from the GNSS satellite to the GG-R CubeSat (TR) and the reflected signal path, which travels from the GNSS satellite to the SP and then back to the GG-R ($T\hat{X}R$) (Figure 3.1). Additionally, the surface height is a function of the relative total phase between the direct and reflected signals. This phase difference can be reconstructed for the L_1 and L_2 carrier frequencies and modeled using the a priori OL phase measurements (Φ_{OL}) combined with the unwrapped and corrected residual phase measurements (Equation 3.1) in meters as:

$$\Delta\Phi_i^{RD} = \Phi_i^R - \Phi_i^D = \Delta\Phi_{OL_i}^{RD} - \Delta\phi_{\text{residual}_i}^{RD}, i = 1, 2, \tag{3.3}$$

where superscripts R and D denote the phase measurements in the direct and reflect directions, respectively, and i indicates the L_1 and L_2 carrier GPS frequencies (f_1 and f_2).

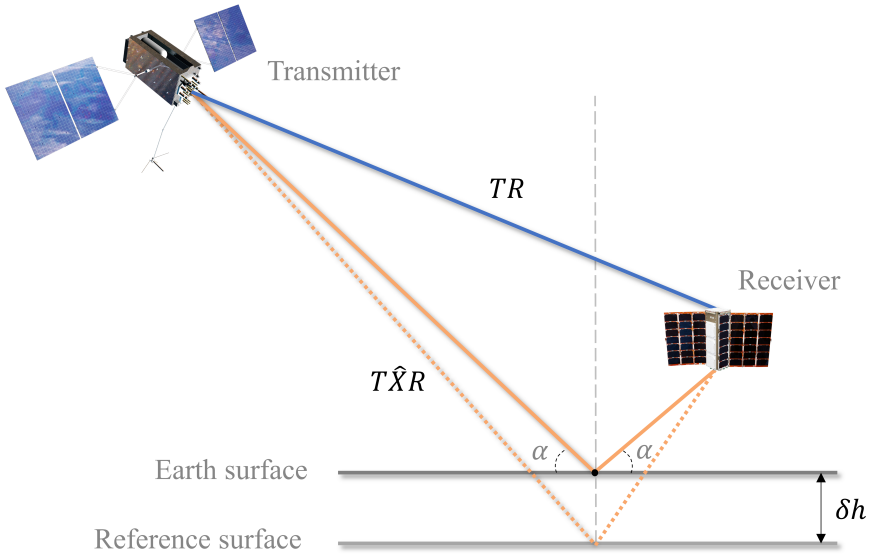

Figure 3.1: Spire grazing angle GNSS-R geometry. TR is computed based on positions of the transmitter, nanosatellite and specular point on WGS84 ellipsoid surface. And $T\hat{X}R$ is based on Spire GNSS-R phase measurements

To begin, it is important to unwrap the phase measurements and address any discontinuities in the carrier phase. The unwrapped phase residual is processed through a cycle slip detecto, which is based on the geometry-free combination of phase residuals of L_1 and L_2 for both direct and reflected signals (Section 3.4). It should be noted that uncorrected cycle slips can result in meter-level errors in sea surface height retrievals, significantly affecting the accuracy of altimetric measurements.

Once the residual phase has been corrected for cycle slips, the application of Quality Control (QC) filters is a critical step. These filters, referred to as coherency criteria, are designed to ensure the quality and consistency of the altimeter data. A detailed explanation of these criteria and their application is provided in Section 3.3.

Finally, the height above the WGS84 ellipsoid (H), can be estimated. This is accomplished by calculating the differences between the a priori relative geometric delay ($T\hat{X}R - TR$) and the actual difference in total phase measurements between the direct and reflected signals. These relative geometric differences are further corrected for ionospheric delay and tropospheric delays affecting the reflected signal (T^R), as well as biases used to adjust the retrieved surface height (δh in Figure 3.1). These adjustments are ultimately projected onto using the slant direction using the elevation angle α, incorporating the Bias-Reference Surface Adjustment (B_{RSA}) as:

$$H = \frac{T\hat{X}R - TR - \Delta\Phi^{RD}_{\text{iono-free}} - T^R - B_{RSA}}{2sin\alpha} \tag{3.4}$$

Table 3.3: Models and methods used in this study for altimetric retrieval

Category	**Models or methods**
Ionospheric delay	Frequency specific
Tropospheric delay	VMF3/GPT3
Reference surface	MSS_CNES_CLS_15
Ocean tide	TPXO9
Cycle slip	Geometry-free combination
Clock errors	Reflected and direct geometric differences

3.3 Coherency criteria

The QC filters, as previously mentioned, are selected through an empirical approach using Spire L_2 data as reference. These filters are based on two key parameters: coherence and continuity. The initial filter identifies measurements that are coherent, rejecting those where the Standard Deviation (SD) of the residual phases (L_1 and L_2 signals) of the reflected signal differences exceeds a specified threshold (set at 0.065) within a 2-second window. The empirically-determined threshold helps exclude measurements with higher variability, guaranteeing the quality of the retrievals. The second filter ensures the continuity of the coherent measurements. Coherent measurements in the signal must last for 3 seconds. After applying these two QC filters, the number of coherent segments within a profile is determined .

3.4 Phase ambiguity

The carrier phase measurement represents the range between the satellite and the receiver, expressed in units of carrier phase cycles. The GNSS transmits in the L-band radio frequency, with the carrier modulated by a pseudorandom noise (PRN) code. This signal is transmitted as a linear combination of sinusoids with an amplitude of 2π, where the sinusoidal period depends on the wavelength of the signal. For example, the GPS L_1 and L_2 frequencies correspond to wavelengths of 19.05 cm and 24.45 cm, respectively.

These measurements for precise computation of the range between the satellite and the receiver. However, the measurements are subject to ambiguity regarding the number of cycles due to errors such as thermal noise, multipath effects, clock errors, and atmospheric disturbances. While the tropospheric layer can cause phase errors, the ionospheric layer is particularly influential, introducing frequency-dependent phase errors. These changes in the phase measurements are referred to as Cycle-Slips (CSs), which manifest as jumps in phase measurement, typically on the order of the signal's wavelength.

The detection and correction of CSs is a challenging task. To provide the precise number

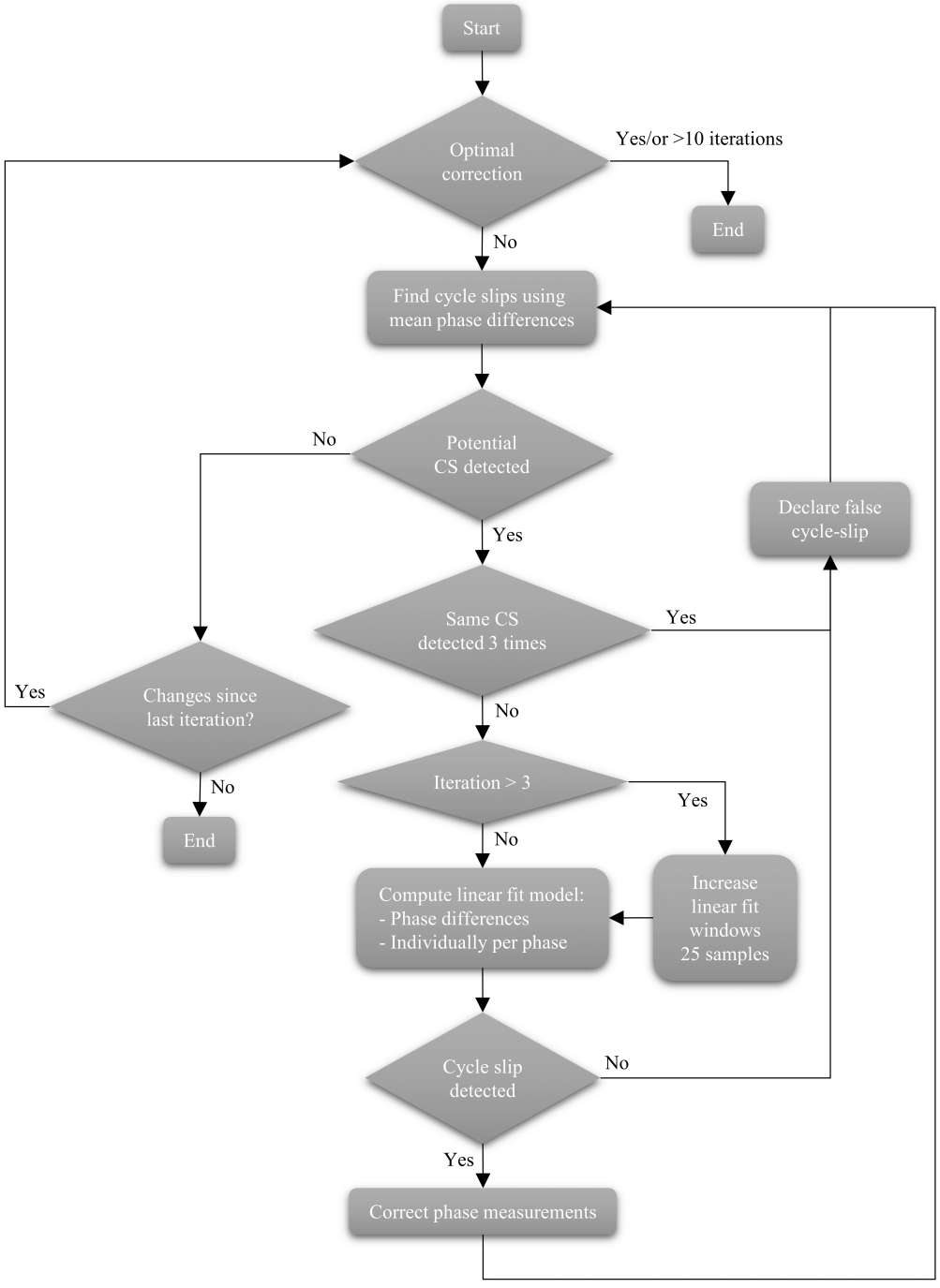

Figure 3.2: Scheme of Cycle-Slip detection and correction function

of cycles, the Cycle-Slip (CS) must be identified and corrected amidst signal noise. In single-frequency data, only one signal is available for analysis. However, with dual-frequency data, phase differences between the frequencies are used to detect and correct the CSs.

The method used in this dissertation is based on a geometry-free combination approach. Using dual-frequency measurements, we can detect where phase jumps occur and correct them individually for each frequency. The process for detecting and correcting the CSs is outlined step by step as follows:

1. Dual-frequency measurements are used to detect the location of the CSs. This is achieved by analyzing abrupt mean changes in the data within a threshold corresponding to the differences in the wavelength of the signals.

2. For each detected CS, a linear model is fitted to the differences for each frequency, with 50 samples (corresponding to a 50 Hz data sampling rate) taken to the left and right of the identified cycle-slip location. If significant deviations are found (jumps with amplitudes close to the wavelength for the individual signal or its differences), the phase measurements are adjusted accordingly.

3. The previous step is repeated until no additional CSs are detected in the current iteration.

4. After completing the correction process for all detected CSs, the phase measurements are corrected for those identified in the iteration. The process is then restarted until an optimal solution is found or a maximum of 10 iterations is reached. Moreover, if a CS is detected 3 times at the same location within a single iteration, it is declared as false CS and will until next iteration when the list will be disregarded in the current iteration. The list of false CSs is reset in the next iteration.

Figure 3.2 schematically shows the workflow of the algorithm developed to detect and correct CSs.

3.5 Atmospheric delay

The Earth atmosphere is divided into different layers based on their characteristics. In ascending order, these layers include the troposphere (from the Earth surface to 18-20 km, depending on latitude), stratosphere (20-50 km), mesosphere (50-85 km), thermosphere (85-600 km) and exosphere (600-10.000 km), with respective intermediate layers (Figure 3.3). In terms of electromagnetic properties, the atmosphere is primarily structured into the neutral atmosphere (which includes the troposphere and stratosphere) and the ionosphere.

Both the troposphere and ionosphere significantly affect GNSS signal propagation, introducing various delays and noise. This impact is particularly notable in GG-R (Figure 3.3), where both the reflected and direct signals traverse substantial portions of the atmosphere. Given their critical role in the technique, dedicated sections will be devoted to discussing these atmospheric layers in greater detail. Figure 3.4 schematically shows the GG-R signal as it passes through the troposphere and ionospheric layers.

3.5.1 Ionospheric delay

The ionosphere is a layer of the Earth's atmosphere that extends from approximately 50 km to 1000 km above the surface. As the name suggests, this layer is primarily composed of ionized particles. The composition of the ionosphere is influenced by solar radiation (X and Ultra-Violet rays). During the day, solar radiation causes the ionization of neutral particles, producing free electrons and ions. At night, this process reverses, with neutral particles reappearing and the concentration of electrons and ions decreasing.

The propagation delay of signals in the ionosphere is directly proportional to the electron density in the layer. A higher concentration of electrons, which occurs under increased solar radiation, results in a longer signal propagation delay. This delay is also dependent on the frequency of the signal.

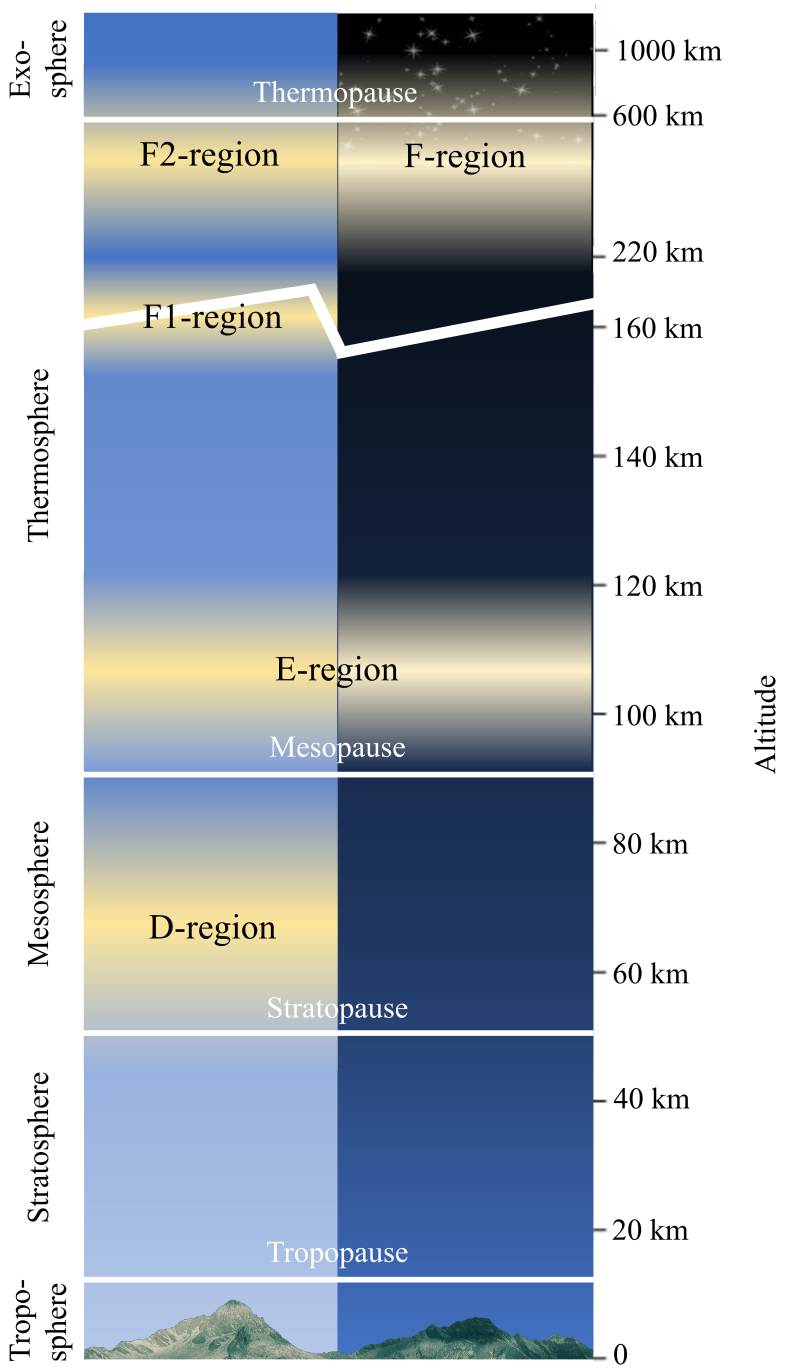

Figure 3.3: Day and night ionospheric regions and atmospheric layers

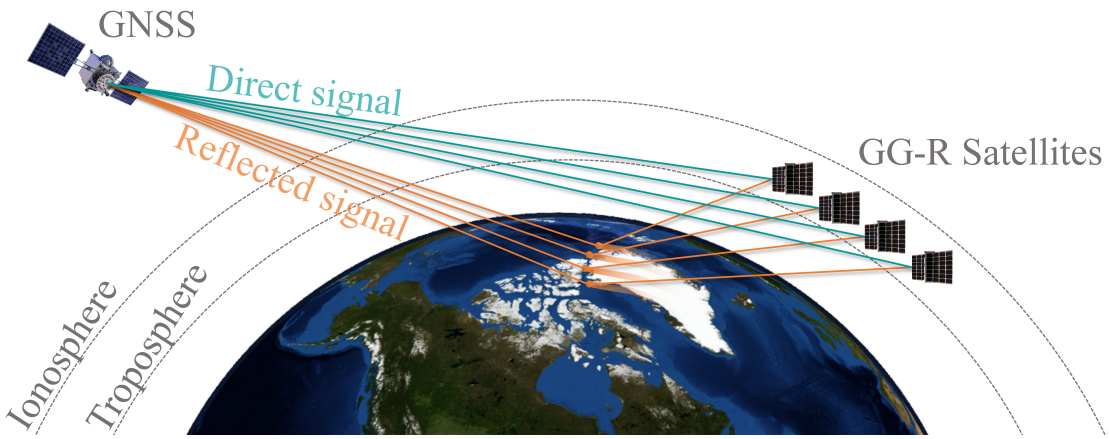

Figure 3.4: Low grazing angles GG-R signal through troposphere and ionosphere

Layers of the Ionosphere

The ionosphere spans a region that includes parts of the mesosphere, thermosphere, and exosphere. It is divided into subsections known as regions, which are structured according to electron density: D, E, F1, and F2 regions. The electron density, and therefore the altitude range of these regions, changes over time. During the day, when solar radiation interacts with the atmosphere, D-region spans from 50-90 km, the E-region from 90 to 150 km, the F1-region from 150 to 220 km, and the F2-region from 220 to 1000 km. At night, the E-region remains within the same altitude range but with a reduced electron density. The D-region almost disappears, and the F1 and F2 regions merge into a single F-region, which extends from 220 to 1000 km. It is worth to mention that the boundaries of these ionospheric regions are variable, and altitude ranges provided are approximates.

Electron Density and its variation

The electron density, and therefore the thickness of the layers introduced in the previous paragraph, varies with latitude, time of day, year, and the solar cycle. The electron content exhibits the following characteristics:

- It is lower at middle latitudes and highly variable in polar, subpolar, and equatorial regions.
- It reaches its daily peak in the early afternoon (around 14:00 local time) and its minimum at midnight local time.
- It is also lower during the summer at mid-latitudes in northern hemisphere compared to winter, a phenomena known as winter anomaly.
- It follows an 11-year cycle, with its peak occurring during solar maximum, when solar flares are most frequen.

Impact of the Ionosphere on the GNSS signals

The GNSS signal experiences a frequency-dependent delay as it travels through the ionosphere. The lower the frequency emitted, the larger the signal delay will be. Additionally, as previously mentioned, the greater the ion density in the ionospheric layers, the larger the delay will be. However, the effect on the signal differs between code and carrier phase. or the code, the ionospheric delay is positive, meaning the signal is delayed, whereas for the carrier phase, the effect is the opposite: a higher ion density results in a negative delay, causing the signal to travel faster. In both cases, the magnitude of the delay is the same, but the sign of the correction differs..

Ionospheric delay is one of the largest and most important corrections for positioning purposes, as its error magnitude can be significant, typically in the range of 5 to 15 m. In extreme cases, such as during large solar activities, the error can increase to several hundred meters[49].

Total Electron Content (TEC)

The TEC quantifies the total number of electrons present along the trajectory of a signal as it passes through the ionosphere (Equation 3.5). TEC is measured in TEC Units (TECU), where 1 TECU equals 10^{16} electrons per square meter, and the range typically spans from a few to several hundred TECU.

$$TEC = \int_s N_e ds \tag{3.5}$$

Generally, TEC is modeled in the slant direction and then projected onto the vertical reference using the zenith angle from the transmitter to the receiver. This projection is referred to as Vertical Total Electron Content (VTEC).

Once TEC is determined, the ionospheric delay can be modeled as:

$$\Delta t = \frac{Kx\mathit{TEC}}{f^2} \tag{3.6}$$

where, f is the signal frequency and $K = 40.3$, a constant determined by a combination of physical parameters related to the signal's passage through the ionosphere.

Single-frequency ionospheric delay estimation techniques

To estimate the ionospheric delay using a single frequency, models or correction techniques are typically employed. The single-frequency approach is commonly used in cost-effective receivers; however, it is less effective compared to methods that use multiple frequency signals, which cansignificantly degrade positioning accuracy.

The most commonly used models and correction techniques include the Klobuchar model [50], NeQuick model [51], and the use of Global Ionospheric Maps (GIMs). Each method has its advantages and weakness, which are described below:

- **Kobuchar Model** is one of the most widely used models for single-frequency ionospheric correction. It can reduce ionospheric effects by up to 50% according to [52]. It estimates the piercing point an the average height of the ionosphere at the time when the signal is emitted, using the transmitter and receiver's location. With this information, along with data collected from the navigation messages, the model can estimate the necessary coefficients to determine the TEC of the signal. [50]

- **NeQuick Model** is an empirical, three-dimensional, and time-dependent model. It provides a guaranteed correlation capacity of at least 70% for the ionospheric code delay, Root Mean Square (RMS), according to [53]. The model uses 12-month values of solar radiation activity to estimate the solar flux at a specific time and location, with the electron content defined by this parameter and the location of both the GNSS satellite and the receiver. [51].

- **GIMs** offer an alternative method for estimating ionospheric delays in single-frequency GNSS systems. These maps are produced by processing data from a worldwide network of GNSS receivers that measure the TEC in the ionosphere. The maps are regularly updated and provide a TEC value for the signal's path, which can be used to correct ionospheric delays. This technique provides greater accuracy (up to 80%

of the ionospheric delay can be estimated [54]), particularly during periods of intense solar activity or in areas with significant ionospheric variability [55, 56].

While these models and techniques are useful, the most accurate method for estimating ionospheric delays remains the use of dual-frequency measurements.

Dual-frequency ionospheric delay estimation techniques

Dual-frequency measurements offer a significant advantage in GNSS ionospheric delay estimation by effectively eliminating first-order ionospheric effects (up to 99.9%). As previously mentioned, ionospheric delay is one of the most significant sources of error in GNSS positioning. Therefore, the possibility to use dual-frequency measurements, as opposed to single-frequency measurements, is crucial for obtaining accurate results.

The technique works by comparing the phase shift between a pair of frequencies (typically L_1 and L_2 for GPS) to identify ionospheric distortions in real-time. The ionospheric-free combination, presented in Equation 3.7, uses dual-frequency phase ϕ or pseudorange R measurements, along with the signal frequencies f, to determine the ionospheric delay [57].

$$\Phi_{iono-free} = \frac{f_1^2\Phi_{L_1} - f_2^2\Phi_{L_2}}{f_1^2 - f_2^2}; R_{iono-free} = \frac{f_1^2 R_{L_1} - f_2^2 R_{L_2}}{f_1^2 - f_2^2}. \tag{3.7}$$

This method not only enhances positioning accuracy but also improves reliability and consistency, particularly in situations where ionospheric conditions are highly variable. Moreover, dual-frequency systems are more robust against signal interference and multipath effects.

3.5.2 Tropospheric delay

The Troposphere is the first layer of the Earth's atmosphere and contains the largest air mass. Its average height is is approximately 13 km, but it varies globally, being larger at the Equator than at the poles. Similar to the ionospheric layer, the GNSS signal passing through the troposphere will cause delays along its path. These delays depend on tropospheric conditions (temperature, pressure and humidity). Unlike ionospheric effect, the tropospheric

delay is not frequency-dependent, meaning it can be estimated using models alone. A key advantage of the tropospheric is its relative stability and predictability compared to the ionospheric layer, allowing for more accurate models.

The tropospheric delay is divided into two main components: wet and dry. The wet component, which consists on predicting the water vapor (clouds) in the troposphere is more difficult to determine than the dry component, which is composed by the gases in the atmosphere. If the GNSS signal is not corrected for the tropospheric delay the errors that may cause can be up to 25 meters [23].

The most commonly used methods and models are as follows:

- **Saastamoinen**: One of the first models and one of the most widely used. Has a fair first-order tropospheric delay estimated and its commonly used for general applications [58].
- **Hopfield**: Old but still currently used model based on a simplified atmospheric structure to estimate the delay [59].
- **University of New Brunswick (UNB)**: Stands for University of New Brunswick and it is a improvement of the Saastamoinen model[60].
- **Vienna Mapping Function (VMF)**: It is a sophisticated model used in high-precision GNSS applications. The newest version released, version 3, proved better global accuracy [61].
- **Global Pressure and Temperature (GPT)**: It is an empirical model for pressure and temperature globally. It is used for post-processing and geodetic applications [62]. This model is often used in conjunction with VMF to improve its accuracy.
- **Global Forecast System (GFS)**: It is a Numerical Weather Prediction (NWP) model developed and operated by the National Centers for Environmental Prediction (NCEP). It provides accurate forecasts of atmospheric conditions, including tropospheric variables, on a global scale.

Table 3.4: Summary table of the reference surface models used in this thesis, including MSS, Tidal models and DEM models

Type	**Model**	**Coverage**	**Resolution**	**Key Features**
MSS	DTU18MSS	Global	2 km	Multi-satellite data (20 year product up to 2018)
	DTU21MSS	Global	2 km	Latest DTU model that integrates more sat. data up to 2021
	MSS-CNES-CLS-15	Global	2 km	Multiple altimetry data from 1993 to 2012
	MSS-CNES-CLS-22	Global	2 km	Latest CNES model that adds new sat. data until 2021
	SIO CNES-CLS15 DTU15	Global	2 km	Hybridization of Scripps-CLS15, CNES-CLS15, and DTU15 MSS
Tide models	TPXO9	Global (Open Ocean)	1 km	Tidal model optimized
	Arc2Km	Arctic Region	2 km	Tidal model optimized for Arctic region
DEMs	Earth2014	Global	from 2 km to 1 km	Global DEM model using data until 2014
	REMA	Antarctica	from 2 m to 1 km	Antarctic DEM model
	ArcticDEM	Arctic region	from 2 m to 1 km	Arctic DEM model
Grid SLA	CMEMS	Global	$0.25^\circ \times 0.25^\circ$	Gridded SLA computed with a thirty-year [1993, 2023] mean

3.6 Reference surface models

The reference surfaces model is an important parameter in GG-R techniques as the relative surface height need to be adjusted to it. The model selected for the adjustment accounts for the surface type and characteristics of the reflection.

Models can be global or regional and can be ocean or land surface height with different resolutions. The models for ocean surface are called MSS and they are often applied with the tide corrections, and the land surface models are called DEM.

There are many combinations and each reference surface needs to be chosen according to the surface characteristics and regions. Table 3.4 contains the models that are going to be used in this dissertation. In addition, the description of the models is listed here:

- **Technical University of Denmark (DTU)** is recognized internationally as a leading university in the areas of the technical and the natural sciences and it has developed different MSS models (DTU13MSS [63], DTU15MSS [64], DTU18MSS [65] and DTU21MSS [66]) that provide high-resolution global sea surface height.
- **Centre National d'Etudes Spatiales (CNES)** is a French agency is charge of various public products including MSS that offer their own MSS products and the hybrid MSS that combines three different reference MSSs over the ocean: the Scripps Institution of Oceanography (SIO) MSS [67] in the open ocean, CNES Collecte Localisation Satellites (CLS) 2015 or 2022 MSS [68] in coastal areas and the Antarctic region, and DTU15 or DTU21 MSS [64, 66] in Arctic regions.
- **TPXO** is a high-resolution global tidal model from Oregon State University (OSU) that predicts ocean tides using satellite altimetry data and hydrodynamic modeling. The model includes tidal components (amplitudes and phases) for major and some minor tidal constituents. [69]
- **Arc2Km** is a high-resolution tidal model that the Earth and Space Research (ESR) and OSU create and provide barotropic tide models for the Arctic Ocean and the seas surrounding Antarctica [70].

- **Earth 2014** developed by Curtin University (Western Australia) and Technical University (TU) of Munich is a DEM model of earth's topography, bedrock and ice-sheets constructed as a composite from up-to-date topography models [71].
- **Arctic DEM and REMA** are a high-resolution and high-quality DEM that provides detailed topographic data for the Arctic and the Antarctic regions, respectively. There were developed in a public-private initiative by the Polar Geospatial Center (PGC) at the University of Minnesota in collaboration with NGA-National Science Foundation (NSF) [72] [73].
- **The Global Ocean Gridded L4 SLA** dataset used in this thesis is produced by the Copernicus Marine Environment Monitoring Service (CMEMS) and computed to a mean from 1993 to ongoing [74].

Chapter 4

Ocean and sea-ice GG-R altimetry

In this section, we discuss the findings of the Ocean and sea-ice GG-R altimetry studies in this dissertation. The section is divided into five parts: (1) the first study involves validating the initial model formation over Hudson Bay [75], followed by (2) an investigation of the relationship between ice concentration and signal coherency in the same region [76]. The next two sections will focus on parameter improvements: the first (3) describes a novel method for estimating the ionosphere [77], and the second (4) offers a comparative study where we evaluate retrievals using various models and techniques to determine the most optimal solution. Finally, (5) we will present a global comparison between GG-R and a set of satellite altimeter solutions [78].

4.1 Inital GG-R Altimetry in the Hudson Bay

In this work, Spire dual-frequency phase observations under GG-R events during a 3-month ice period from the 1st January to 31st March 2021 are used to assess the initial performance of the model formulation for precise altimetry in a steady region where sea ice is present. Hudson Bay is located north of Ontario, west of Quebec, north-east of Manitoba, and south-east of Nunavut, but it is entirely part of Nunavut (see Figure 4.1) and it has a surface of 1.3 million km^2 forming one of the biggest inland seas in North America. Typically, the Hudson Bay is completely ice-covered by late December and is free of ice from

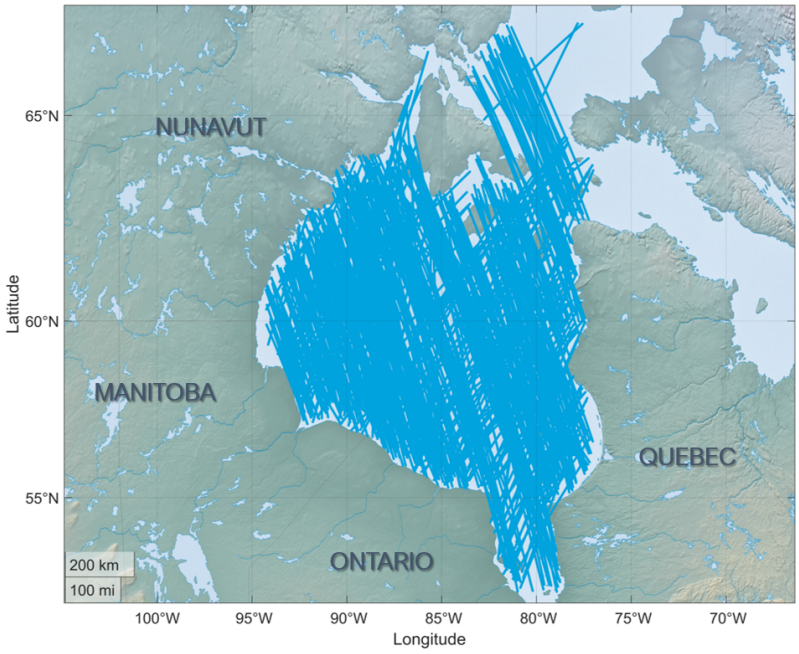

Figure 4.1: Reflections observed over the area of Hudson Bay from January to March 2021

mid-August to late October. Second-year ice is found on rare occasions, but is limited to the northeastern Hudson Bay [79]. The maximum ice extension of Hudson Bay remains almost constant ($\sim$1.19 million km^2) from January until April (see Figure 4.2). Therefore, January to March has been selected in this study as the period with the most consistent coverage of sea ice. This has been considered the most suitable and steady starting point case study for further analysis in the polar regions. Section 4.1.1 describes the Spire GG-R data and the models used in this study. Finally, the GG-R height retrievals are validated against a reference surface in section 4.1.2.

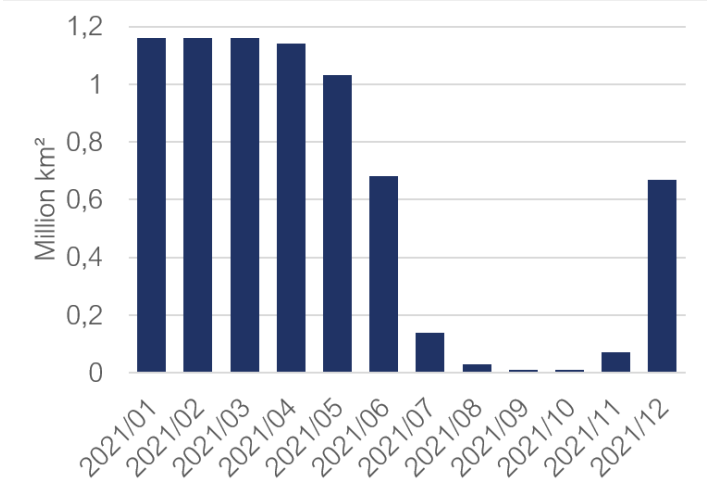

Figure 4.2: NOAA Sea-ice extend from January to December 2021 [80]

4.1.1 Data and Models

The Spire FMs that we collect data from are 79, 88, 99, 100, 101, 102, 103, 104, 106, 113, 116, 118, 120, 122, 124 and 125 (see Table 3.1 for orbital information).

Out of 525 L1B profiles, 508 were sufficiently coherent to allow for altimetry retrievals. However, three profiles had to be excluded due to significantly inaccurate measurements. This recommendation comes directly from Spire's team, who have also observed profiles where some reflected signal measurements are considerably off, requiring further investigation to address the problem. As a result, all retrievals with height RMSE exceeding 10 meters are discarded without exception (see Figure 4.3).

In this study, the GPT3 model and VMF3 [61] are used. The surface height deviation retrievals are adjusted to the reference surface model combined DTU21MSS with a 1-min resolution [66] and the ocean tide model TPXO9-atlas.

4.1.2 Altimetry Retrievals

More than 500 profiles over the Hudson Bay have been considered to compute surface height deviation (Figure 4.4) for a 3-month period from January to March 2021. Figure 4.4 shows the percentage of tracks' coherence as well. Table 4.1 summarizes the RMS error be-

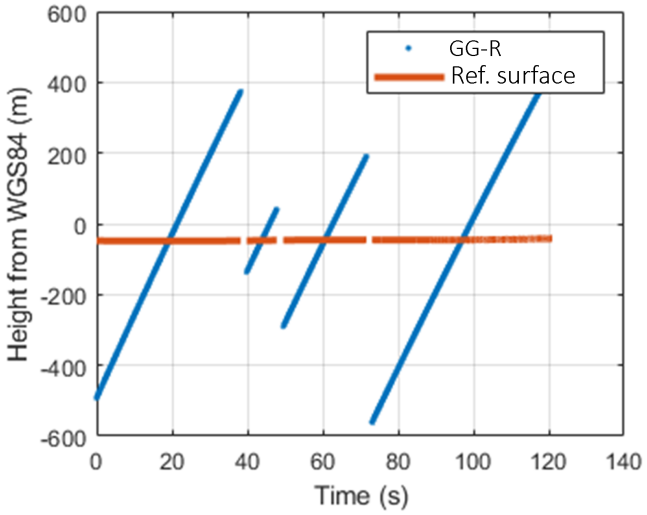

Figure 4.3: GG-R event over Hudson Bay on 23 January 2021 04:24:47 UTC (blue line) surface height retrievals (orange line) reference surface model. The RMS between the surface height and the reference surface model is 181.9 m

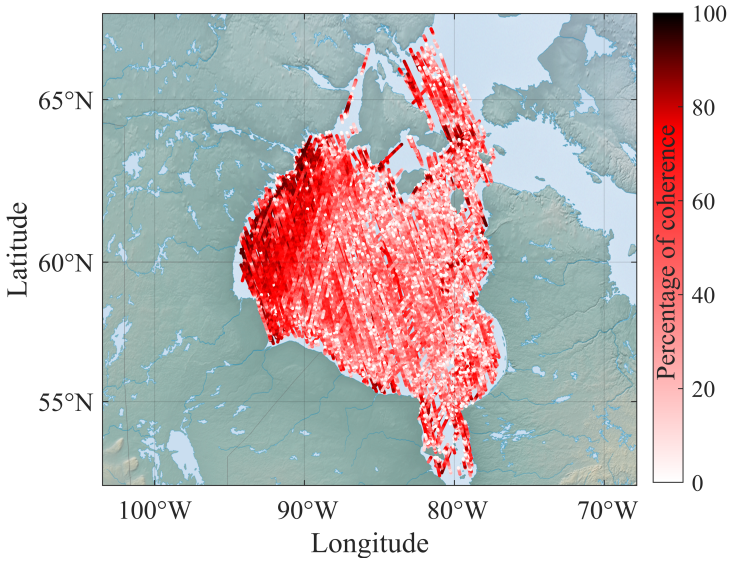

Figure 4.4: Measurement coverage and coherence percentage over Hudson Bay from January to March 2021

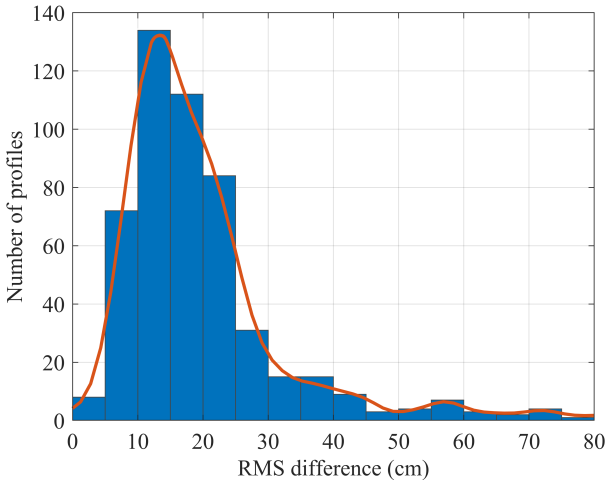

Figure 4.5: Histogram of RMS differences between GG-R height profiles and DTU + TPXO

tween the GG-R altimetry retrievals and the reference surface model over this three months period. While the large majority of GG-R profiles agree with the reference surface model within 50 cm, 63.6% of the profiles successfully retrieve surface height with an RMS error of less than 20 cm.

Table 4.1: Percentage of RMS error between the GG-R profiles and the reference surface model

RMS	< 5 cm	< 10 cm	< 20 cm	< 50 cm	< 1 m	< 1.6 m
% of tracks	1.0%	15.2%	63.6%	94.5%	99.4%	100%

Figure 4.5 shows the RMS error histogram of the GG-R profiles that agree with the reference surface (DTU21MSS and TPXO) within 80 cm that represents the 98.6% of profiles. The mean RMS error of all 500 profiles over the three-month period from January to March 2021 in Hudson Bay is 16.4 cm.

Figure 4.6 illustrates a height retrieval collected on 24 January 2021 at 20:26:52 UTC by Spire satellites FM-104 and transmitted by GPS PRN 08. The 50-Hz GG-R profile has a RMS error of 4.5 cm. The average of the elevation angle for this track is 21.6°. Moreover, the RMS error between the smoothed 1-Hz surface height and DTU21MSS that is corrected for ocean tide is 2.7 cm.

Table 4.2: RMS differences between GG-R height profiles computed with different reference surface and tropospheric models

	DTU18MSS	**DTU21MSS**
VMF3/GPT3	16.5 cm	16.4 cm
UNB3m	17.0 cm	16.9 cm

Table 4.2 compares the retrieved heights using different mean sea surface and tropospheric models. There is a millimeter differences between the GG-R height retrievals using different models. On one hand, DTU21MSS performes better than DTU18MSS with an RMS error of about 1 mm. On the other hand, the RMS differences between GG-R height profiles and the surface model using VMF3/GPT3 and UNB3m tropospheric models are not statistically significant.

As it can be seen in the Figure 4.7, the high-RMS error retrievals are mainly from the low-elevation angle profiles (i.e., lower than 15°). This is due to the limited tropospheric resolution for low-elevation height profiles. Therefore, further investigation on the tropospheric models would improve the precision of GG-R height retrievals. Additionally, it has been noticed that further improvement in the phase unwrapping algorithm would yield more precise surface height retrievals.

Overall, as the RMS error of the vast majority of the profiles is less that 50 cm (94.5%), suggesting that precise carrier phase altimetry can be derived using low-Earth receivers under GG-R events over sea-ice covered areas.

4.1.3 Summary

Precise carrier phase altimetry was derived from Spire grazing angle GNSS-R observations over Hudson Bay for a three-month period from January to March 2021. The altimetry retrievals are corrected for tropospheric delay from computed slant paths using VMF3/GPT3. The mean RMS error between GG-R height profiles and DTU21MSS mean sea surface model that are corrected for tides is 16.4 cm. Therefore, the initial model formulations are validated starting in an area where sea ice is present that can be extended to other similar regions.

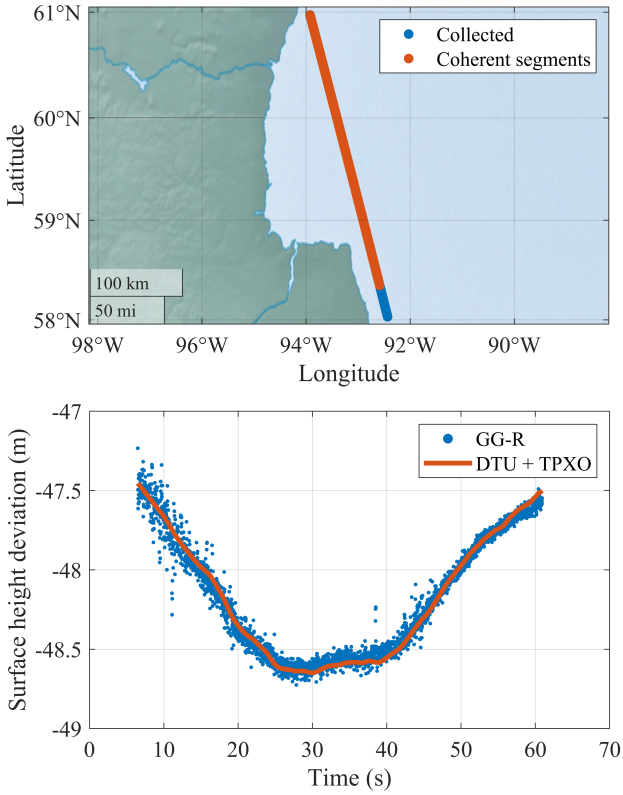

Figure 4.6: (top) GG-R event over Hudson Bay on 24 January 2021 20:26:52 UTC, and (bottom) surface height retrievals (blue dot) and modeled sea surface height (red line)

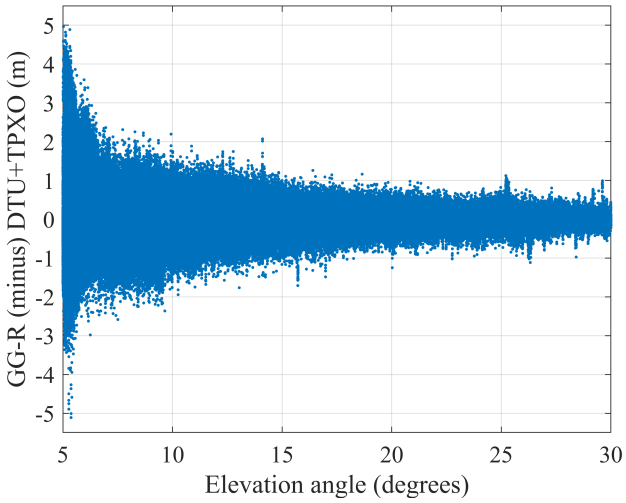

Figure 4.7: Surface height deviation minus computed reference surface as a function of specular point elevation angle

4.2 Coherency and sea ice concentration correlation over Hudson Bay

The area is selected for this study to identify the relationship between the coherency of GG-R measurements and ice concentration. The main purpose is to improve the accuracy and understanding of GG-R altimetry measurements and the factors that might influence the retrievals using this technique. As mentioned previously, current altimetry satellites (as of mid-2024), such as Sentinel-3, have certain limitations in terms of temporal and spacial resolution, especially in polar regions. However, the precision of GNSS-R measurements does not yet match the accuracy achieved by satellite altimeters like Jason-3, which reaches an accuracy of 3 cm [46], whereas GG-R techniques achieve decimeter-level accuracy [14, 77]. Continuous research in this technique is crucial for improving retrievals, particularly in ice-covered regions.

This chapter in this thesis presents a comparison between the coherency and ice concentration from January to October 2021 over the Hudson Bay region. This period allows for comparison of GG-R altimetry retrievals under conditions of both high and low sea ice concentration.

The structure of this chapter is as follows. Section 4.2.1 presents the Spire GG-R satellite and measurements and models used in this study. Section 4.2.2 presents the results of the comparison, focusing on altimetry over the study region. Finally, we have a summary of the results in Section 4.2.3

4.2.1 Data and Models

The UNB3m neutral atmosphere delay model is used to correct for tropospheric delay [60]. The resulting relative surface height is adjusted to the reference surface using combined MSS model [68]. Ocean tides are corrected according to TPXO9-atlas [81].

4.2.2 Results

Aiming to investigate the magnitude of influence of altimetry retrievals using the GG-R technique, we compare ice concentration data and GG-R measurements from January to October 2021 in the area of Hudson Bay. The sea ice concentration product used is MASIE-AMSR2 (MASAM2), a daily Arctic 4-km product in a polar stereographic projection [82]. The MASAM2 combines ice coverage from the Multisensor Analyzed Sea Ice Extent (MASIE) product at a 4 km grid cell size with ice concentration from the Advanced Microwave Scanning Radiometer 2 (AMSR2) at a 10 km grid cell size.

Figure 4.8 shows monthly data of the two products, and Table 4.3 presents numerically the results observed in the figure, including the median RMS of the SLA. The period from January to May represent the months with the highest concentration of ice, with an average ice concentration of 98% and the period from July to October corresponds to the months when nearly all the ice has melted, with the remaining months representing the melting period. An increase in the median RMSE of SLA from 2 to 8 cm is seen as ice concentration decreases. A similar trend is found in the percentage of coherency, with about a 10% difference between high and low ice concentration periods.

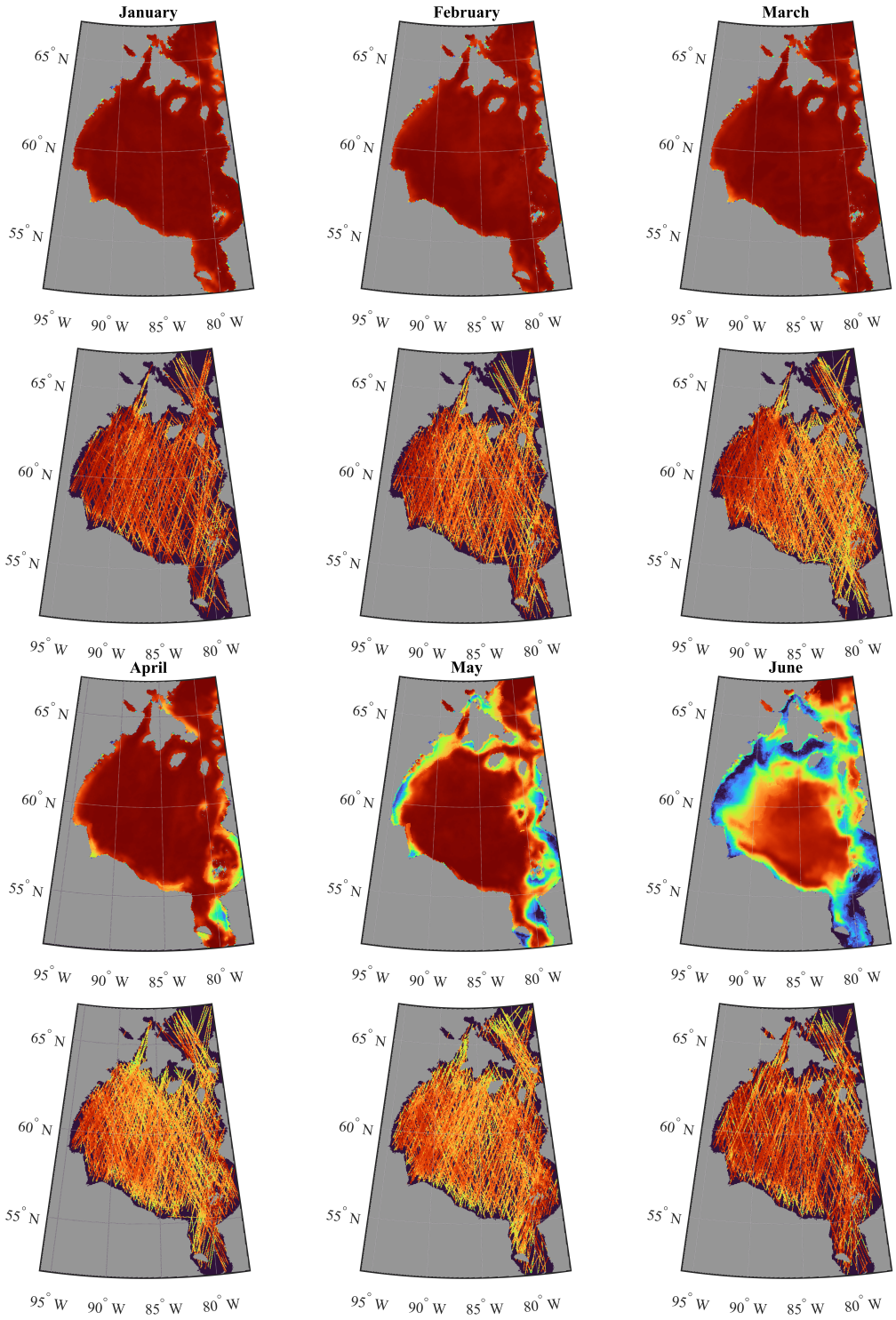
January
February
March
April
May
June
65° N
60° N
55° N
95° W
90° W
85° W
80° W

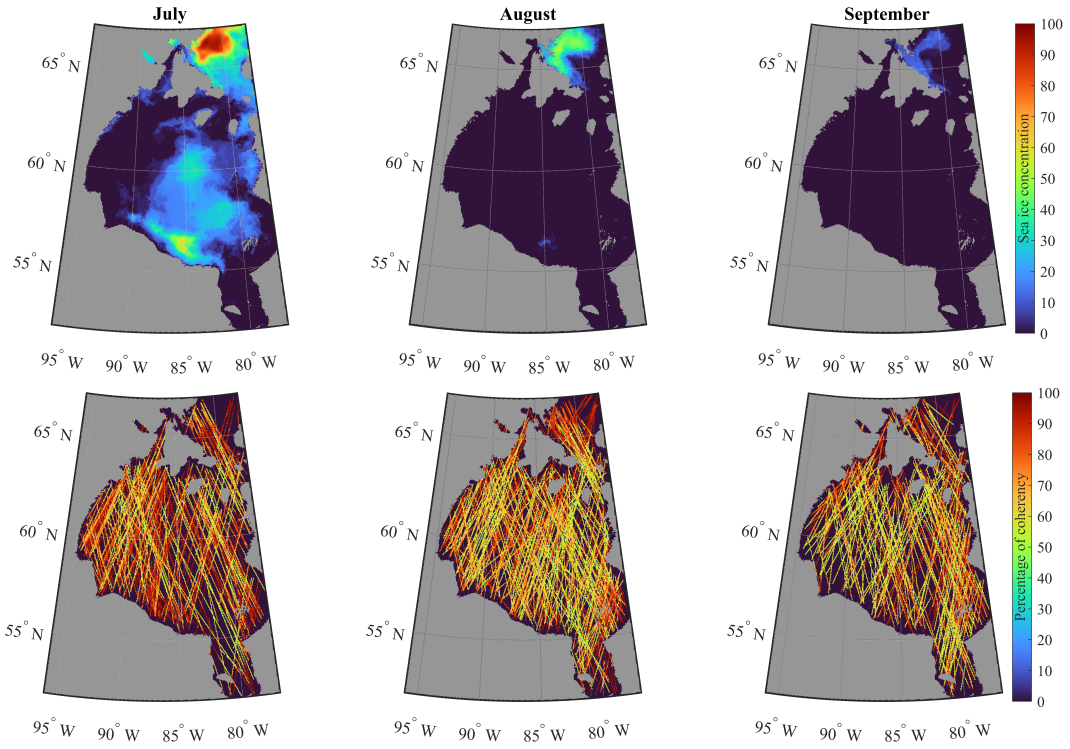

Figure 4.8: January to October 2021 plots of sea ice concentration (odd rows) in percentage from 0% indicating no ice present to 100% representing the highest sea ice concentration, and (even rows) percentage of coherency of GG-R measurements from 0% indicating no coherency to 100% representing the highest coherency value, averaged in a 4-km MASAM2 polar stereographic grid.

The percentage of coherency is computed using the maximum value observed in both scenarios as the reference, assigned a value of 100%. Larger differences in coherency are observed during the high and low periods, particularly from January to May and from July to October. Even though the sea ice concentration product ranges from 40% to 100%, values between 20% and 30% observed during the summer period result from temporal averaging.

Figure 4.9 shows the ice concentration and percentage of coherency for the winter and summer periods. During winter, most of the surface presents high coherency (above 70%). In summer, the highest coherency is generally found in the northern part of Hudson Bay.

The comparison between the summer and winter results shows that, while the majority of the coherency grid cells are below 60% in summer in the center of the Bay, the coherency in winter generally tends to be above 80%. Moreover, the winter study case shows a uniform percentage of ice concentration around the whole area except for the coast and Jason Bay. During the same time frame, observations from GG-R indicate a greater coherency percentage. This is particularly true in the western region of Hudson Bay, where the sea ice concentration remains largely uniform. Additionally, increased anomalies are noted in the water body region west of Southampton Island, with most coherency values fluctuating around 40%. Comparable patterns are observed in James Bay, where reduced coherency correlates with lower sea ice concentrations. In the summer period, the coherency across the Hudson Bay seems to be stochastic except along the coast, specifically in the area of 56°N/77°W and in the region north of the Bay. These locations coincide with higher ice concentration.

Furthermore, the number of GG-R coherent tracks are 1375 and 840 in winter and summer period, respectively. Notably, there are approximately 63% more successful coherent GG-R events in winter than in summer, and the median RMSE between the reference surface model and the altimetry results is 12.5 cm for winter and 18.1 cm for summer, with corresponding standard deviations of 12.5 cm and 33.8 cm for winter and summer, respectively. Once again, this illustrates an improvement in the quality of GG-R signal reflection in regions where ice is present.

Figure 4.10 illustrates two events (FM102 and FM122) tracking signal reflections from

Table 4.3: January to October 2021 summary table of results including the ice concentration and the percentage of compared grid cells.

	SLA RMSE (cm)	Ice concentration (%)	Coherency (%)	Grid cells (%)
January	13.0	98.6	84.6	59.9
February	14.3	98.6	79.3	61.3
March	15.3	98.3	76.5	66.6
April	14.6	98.3	73.2	67.2
May	14.6	95.7	75.1	70.2
June	16.7	60.8	83.4	64.3
July	21.1	6.5	75.8	49.6
August	16.2	0	66.8	59.1
September	17.2	0	65.5	48.5

the same GPS satellite, separated by only 38 minutes and a maximum physical distance of 5.7 km. We can see consistent SLA along the specular point longitude. However, when plotting SLA data against ice concentration, we notice an improvement in SLA values as ice concentration increases.

4.2.3 Summary

This study compares altimetry quality of 3088 Spire GNSS-R dual-frequency retrievals under grazing angle with ice concentration from January to October 2021 over the Hudson Bay area. This region offers a perfect contrast in terms of sea ice coverage: the entire area is covered with ice during the winter (January to May), becoming ice-free in the summer (July to October).

Overall, there appears to be no distinct correlation between regions of increased coherence and higher ice concentrations. However, there are more coherent measurements and overall improvement in the RMSE of SLA from months with lower to higher ice concentration.

One example of this comparison demonstrates consistency in the SLA on the two nearly simultaneous signal tracking events, along with an improvement in altimetry results with higher ice concentration.

A significant numerical distinction is observed when examining the RMSE and standard

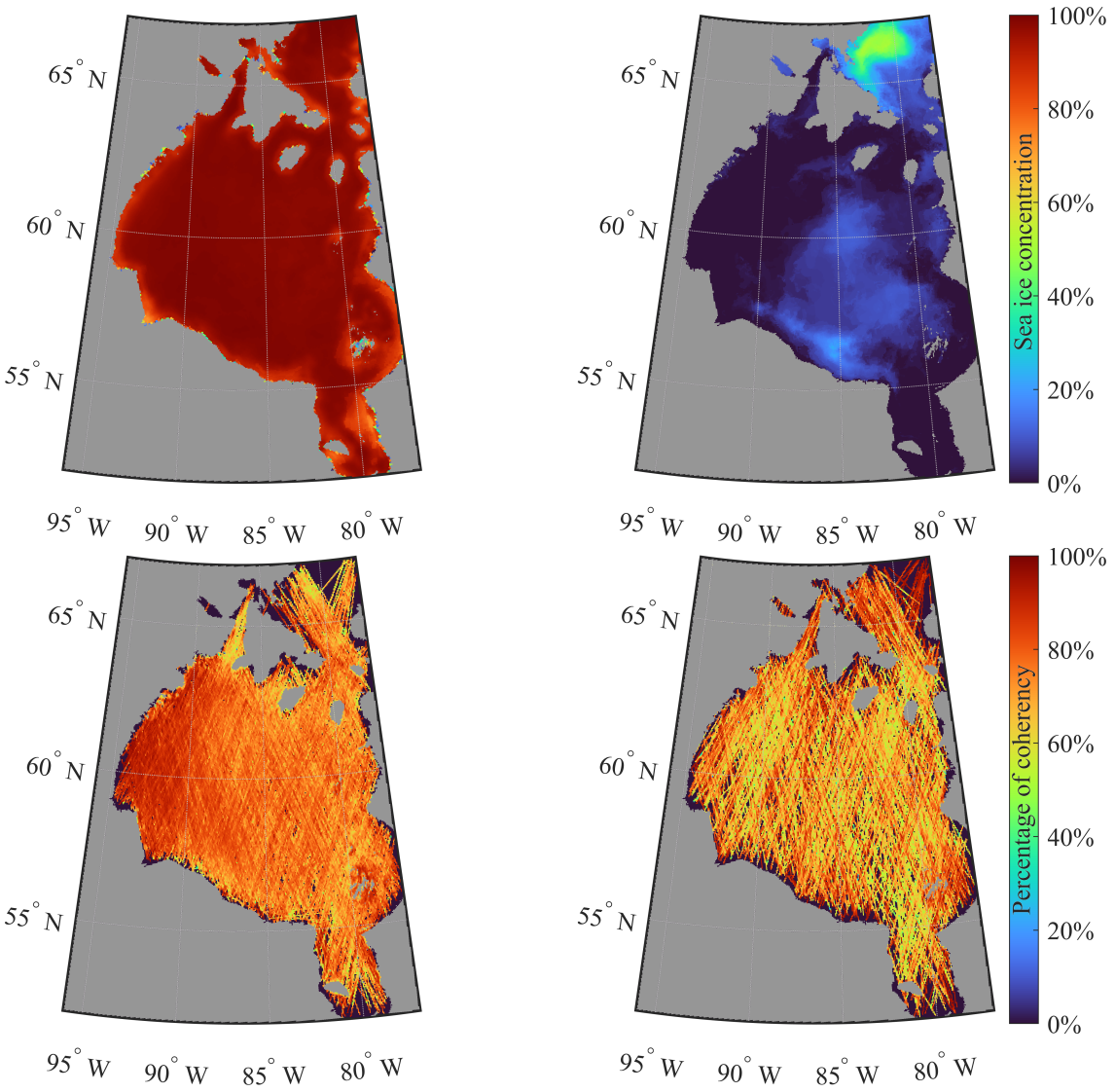

Figure 4.9: Sea ice concentration in percentage (top panel) and the percentage of coherency of GG-R measurements (bottom panel). Data from January to May (left column) and from July to October 2021 (right column), averaged in a 4-km MASAM2 polar stereographic grid.

deviation, with values of 6 and 21 cm, respectively, and an increase of 535 in the number of coherent tracks from summer to winter periods.

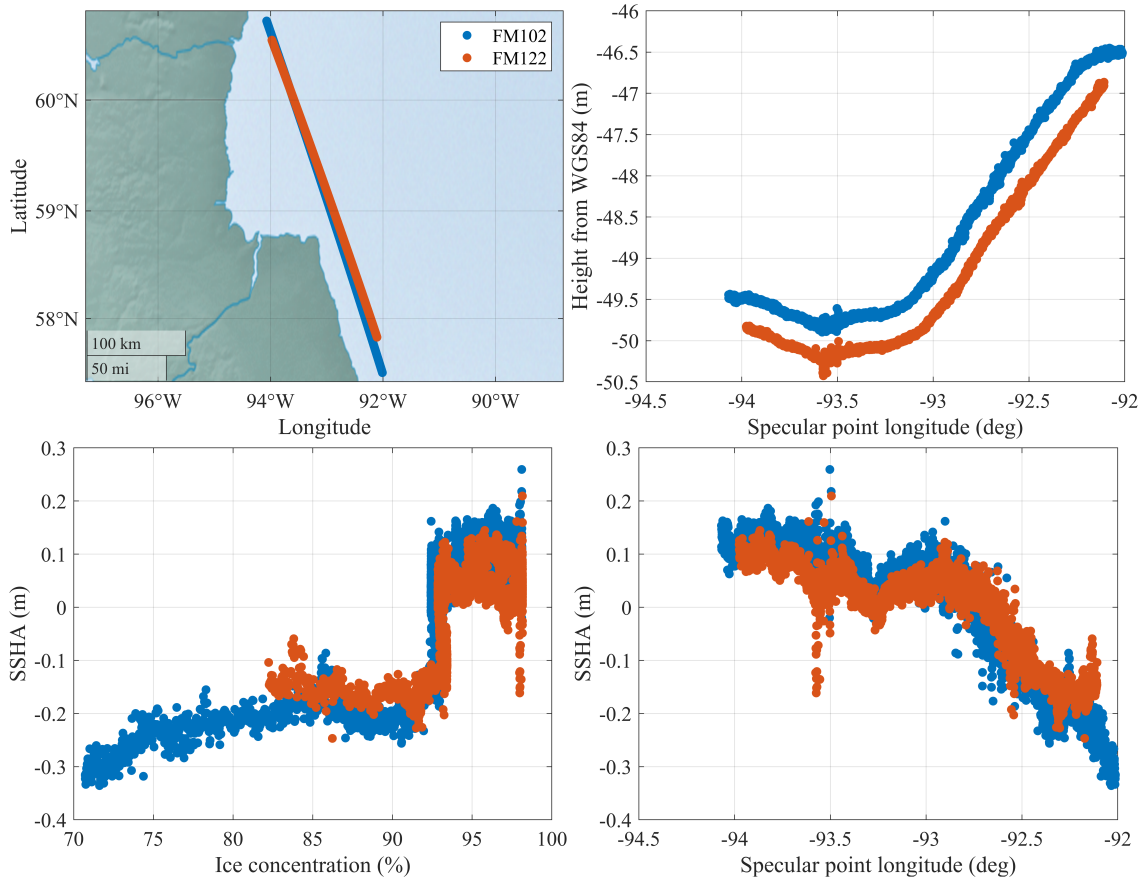

Figure 4.10: Two GG-R events for March 27, 2021, at 02:41:39 UTC (FM102) and 03:19:10 UTC (FM122).

4.3 An improved ionospheric correction model for GG-R altimetry

The Southeast Asian Seas (SEAS), where the Java Sea is located, is a large oceanic pathway that connects the Pacific and Indian Ocean. This region has been widely studied, as sea-level trends are one of the most significant measurements in historical satellite altimetry. Furthermore, when the Pacific Decadal Oscillation (PDO) is removed, the rate of sea-level trends in the last two decades is lower than the global mean sea-level trend [83]. However, the rise in the Global Mean Sea Level (GMSL) will continue and the long-term sea level in the SEAS is projected to rise, putting the coastline in this region at risk. Therefore, any contribution to the altimetric time series in these areas are important for monitoring and understanding the changes in sea-level in the region.

This study presents surface altimetric height retrievals from January 2020 to October 2021 off of Java Sea. In particular, the Java Sea's strategic location, complex tides, sea level variability, and data availability make it an ideal location for sea altimetry using GG-R.

In this work, two different methods are applied to mitigate the impact of ionospheric delay on the retrievals. The first method uses the ionosphere-free combination of carrier phase observation to retrieve the relative surface height above WGS84 [75]. The second method uses frequency-specific carrier phase observations that are corrected for ionospheric delay based on dual-frequency residual phase measurements. The main advantage of this latter method is that it effectively smooths out high-frequency noise in the ionospheric correction, resulting in a three-fold reduction in phase noise compared to the ionosphere-free combination method.

The structure of this chapter is as follows. In Section 4.3.1, the Spire GG-R observations used in this study are outlined. The retrieval algorithms for sea surface altimetry are presented in Section 3. Finally, in Section 4, the GG-R retrievals of the ionosphere-free combination are compared to those using the frequency-specific ionospheric correction method.

4.3.1 Data and Models

The measurements are corrected for tropospheric delay using VMF3 and GPT3 [61]. Also, the adjustments reference surface used for the adjustment is the MSSDTU21 [66], which has been corrected for ocean tides according to TPXO9-atlas [81].

4.3.2 Frequency-specific ionospheric delay correction

We have seen in the Section 3.5.1 that the ionospheric-free combination removes the first-order ionospheric effect. In order to go one step forward and to determine second order ionospheric delay, we need different unique method. As we can see in the Equation 3.7, the ionospheric-free combination is a self-contained method, offering limited possibilities for extracting the second-order ionospheric delay, which is why we introduce the following alternative approach.

In the frequency-specific method, individual correction of total phase differences of L_1 and L_2 is performed using dual-frequency ionosphere correction as:

$$\Delta\Phi^{RD}_{corr_{1,2}} = \Delta\Phi^{RD}_{1,2} + \frac{f^2_{2,1}(\Delta\Phi^{RD}_1 - \Delta\Phi^{RD}_2)}{f^2_1 - f^2_2} \tag{4.1}$$

The correction term that is the second term on the right-hand side of Eq. 4.1 is smoothed using the local robust quadratic regression filter [84]. This filter essentially returns a moving average of the correction term through the use of a fixed window length. A window duration of 10 km was selected after conducting several tests with different window lengths. The mean of the corrected total phase differences of L_1 and L_2 is then used to retrieve the relative surface height.

4.3.3 Results and discussion

Over a 21-month period from January 2020 to October 2021, 714 coherent profiles are found in the Java Sea. Figure 4.11 presents the density of different GG-R tracks found in a 9x9 km Equal-Area Scalable Earth Grid (EASE)-Grid [85], with the aim of visualizing the probability of finding diversity of measurements from different GG-R events. The red dots

in Figure 4.11 represent the historical altimetry ground tracks followed by ocean altimeters since 1992 [86]. It can be seen that the temporal and spatial resolution of conventional altimetry is not comparable to the number of GG-R events collected in this study.

The median RMSE of 24.4 cm and 16.8 cm is observed between the GG-R retrievals and the reference surface model for the ionosphere-free combination and frequency-specific ionospheric delay correction methods, respectively. As a result, the latter method demonstrates a superior performance with an improvement of 7.6 cm when compared to the former method.

Table 4.4 summarizes the RMSE of GG-R retrievals based on ionosphere-free combination and the smoothed frequency-specific correction based on dual-frequency carrier phase observations methods. The most notable discrepancy between the two methods is observed for tracks with RMSE better than 10 cm. 31% of the GG-R height retrievals using the frequency-specific ionospheric delay correction method have an RMSE better than 10 cm, while 5% of the tracks were achieved in this manner when the ionosphere-free combination method was applied.

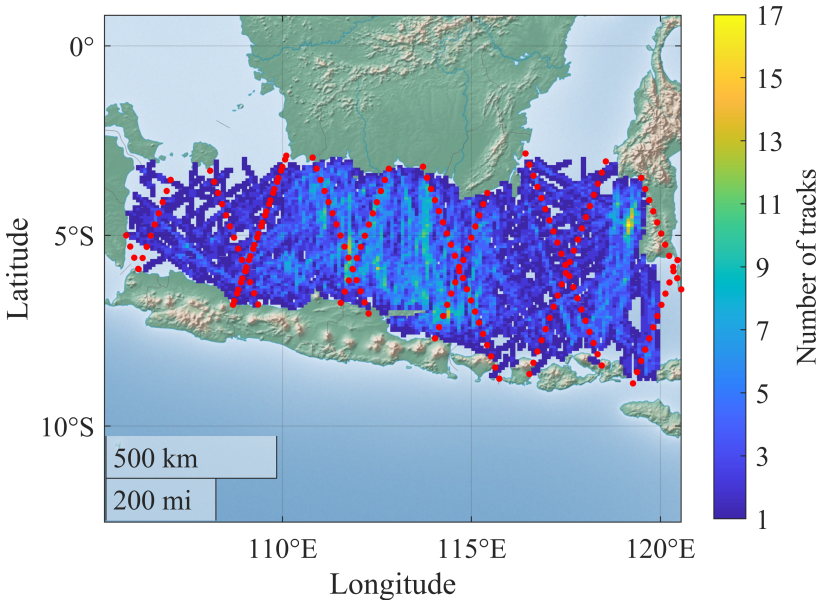

Figure 4.11: Density of GG-R events over Java Sea from January 2020 to October 2021 and the historical altimetry ground tracks since 1992 (red dots)

Table 4.4: Percentage of RMSE between the reference surface model and GG-R height retrievals applying ionosphere-free combination and smoothed frequency-specific correction based on dual-frequency carrier phase observations

RMSE	**Ionosphere-free combination (%)**	**Frequency-specific correction (%)**
< 5 cm	0	7
5 cm - 10 cm	5	24
10 cm - 50 cm	75	53
50 cm - 1 m	15	11
1 m - 2 m	4	4
> 2 m	1	1

Figure 4.12 illustrates an example of GG-R event. The profile was generated on November 30, 2020 at 02:57:34 UTC by the Spire FM122, which tracked the GPS satellite PRN15. Despite having a duration of $\sim$ 61 s, it only has a continuous coherent segment of 20 sec (Figure 4.12a, dark blue). Figure 4.12b and Figure 4.12c depict the GG-R relative heights from WGS84 (black and gray dots representing the ionosphere-free combination and frequency-specific correction methods, respectively) and the reference surface model (yellow line) and the height residuals between the GG-R and the reference model, respectively. While the ionosphere-free combination method provides the relative height with an RMSE of 17.7 cm (black dots), the RMSE of the GG-R retrieval is 7.9 cm when applying the smoothed frequency-specific ionospheric delay corrections. Figure 4.12d shows the estimated ionospheric delays from the frequency-specific method (dark green) and also illustrates the smoothed ionospheric delays (light green). This particular example is one of the profiles whose retrievals are improved approximately one order of magnitude when applying the frequency-specific ionospheric delay correction method (Table 4.4).

The smoothing process is possible in the frequency-specific method due to the individual corrections for each frequency. However, one clear disadvantage of the ionosphere-free combination method is that when phase differences are formed, the corrective term is encapsulated in the combination. Unequivocally, the results obtained by the average of the unsmoothed frequency-specific method of L_1 and L_2 are found to be the same as the ionosphere-free combination.

A comparison of two collocated GG-R events is also presented in this section to assess the repeatability of height retrievals in this study. It is important to note that the reference track in Figure 4.13 is the example presented in Figure 4.12 and the collocated track is collecting the same signal reflection from PRN15. The physical distance between the specular points of the reference and collocated tracks is decreasing from $\sim$55 km to 49 km (Figure 4.13b). It is noteworthy that not only are the two GG-R profiles physically relatively close to one another, but they are also temporally close: the first measurement of the collocated track begins just 20 seconds after the first measurement of the reference track, making this GG-R event particularly valuable. Figure 4.13c shows the relative height from WGS84 using the frequency-specific correction model for the reference (blue) and collocated (red) tracks. The difference between the two GG-R events is 8.2 cm, and the RMSE between the GG-R height profiles and the reference surface model are 7.9 cm and 17.5 cm for the reference and collocated tracks, respectively (Figure 4.13d).

4.3.4 Summary

In this study, two models are investigated to remove the ionospheric effect from Spire grazing angle GNSS-R phase delay altimetry observations. The ionosphere-free combination, which only removes the first-order ionospheric effect, and the frequency-specific model, which smooths out high-frequency noise of the ionospheric correction, are applied for sea surface altimetry over the Java Sea, Indonesia. The results from 714 coherent tracks indicate that the RMSE between the height retrievals using the latter method and the reference model improved by $\sim$ 8 cm. In addition, the cm-level agreement between the two collocated GG-R events and the reference model demonstrates the consistency of GG-R altimetry retrievals. Lastly, the high spatial resolution and increased temporal coverage of the Spire constellation of nanosatellites in low-Earth orbit could provide a more spatially dense set of sea surface height measurements and thus complement conventional altimetry measurements.

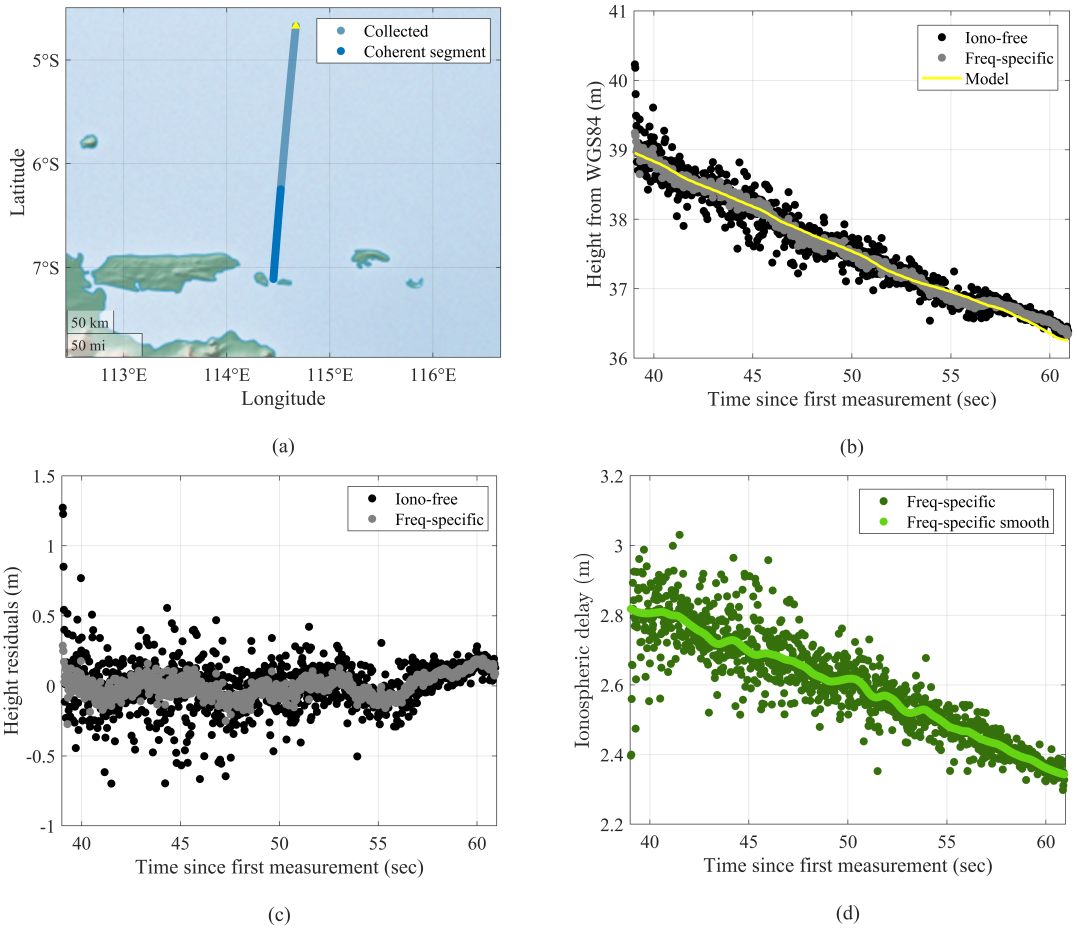

Figure 4.12: GG-R Profile generated on November 30, 2020 at 02:57:34 UTC by FM122 tracking PRN15. (a) Collected (light blue) and coherent (dark blue) segments and first measurement (yellow arrow); (b) Heights from WGS84 for ionosphere-free combination (black dot) and frequency-specific ionospheric delay correction (gray dot) and reference surface model (yellow line); (c) Height residuals between the reference model and GG-R retrievals; (d) Ionospheric delay from frequency-specific correction method.

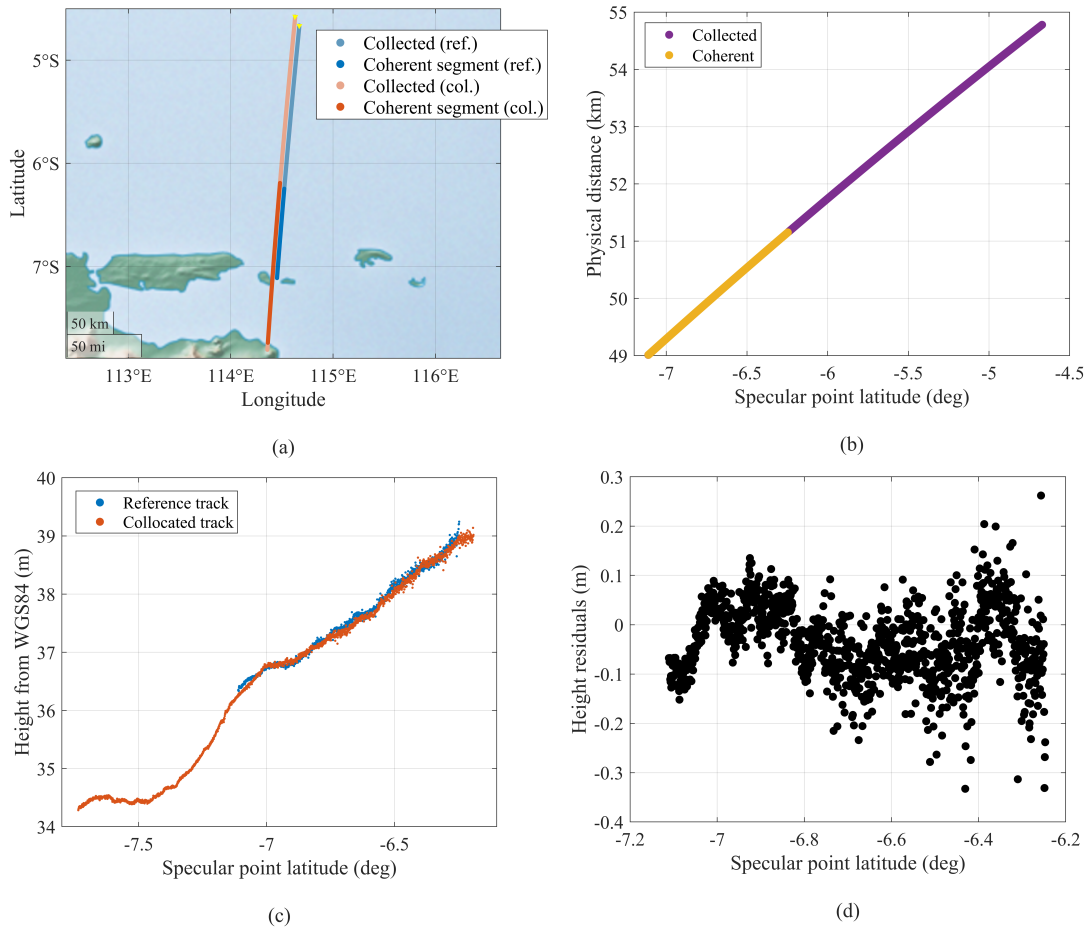

Figure 4.13: The reference track (blue) is the profile used in Figure 4.12 and the collocated track (red) is generated by FM120 tracking the same signal from PRN15 but was taken 20 sec apart from the reference track; (a) Collected (blue and red for the reference and collocated tracks, respectively) and coherent segments and first measurements (yellow arrows); (b) Physical distance over specular point latitude (coherent segments is shown in yellow) ; (c) Relative heights for the reference (blue) and collocated tracks (red) from WGS84 over specular point latitude; (d) Height residuals between the two collocated GG-R events.

4.4 Enhancing the GG-R altimetry parameters and models

Following the success of earlier studies in enhancing ionospheric delay estimation, there was an urge to refine parameter settings in the processing to obtain the altimetry L2 product from L1B data.

A effective approach is to use a well-established and validated altimetry product as a reference, specifically the Spire L2 product. Next, we systematically compiled and analyzed the most relevant models and methods that could influence the accuracy of the obtained altimetry retrievals, which are listed along with a short description in the Table 4.5. Subsequently, we individually modified each parameter and model in the list to assess the impact on the final product, determining whether these modifications led to significant improvements in the altimetry measurements.

Table 4.5: Summary of the parameters and models for Spire GG-R altimetry

Parameters:		**Description:**
Phase unwrapping		Process to unwrap the phase compressed in $-\pi$,π
Tropospheric delay		The tropospheric model applied to the reflected signal
Reference surface	MSS	Mean Sea Surface model applied to the relative height
	Tides	Tidal model
QC filters	Coherency	Filter that determine if the data is coherent or not
	Continuity	Guarantees a segment with continuous data (in sec)
Frequency combination		Type of frequency specific applied
Filter	Type	Type of filter to applied to the frequency specific method
	Order	Order of the filter
	Window	Window of the filter

The Spire L2 data available for this comparison is from 1st of July to 30th of September World-wide. However, the aim for this study was an steady area where the percentage of coherency is higher. Therefore, we once again selected Hudson Bay, which presented a total of 678 coherent tracks (approximately 1.8M samples) for the comparison.

Any data comparison requires an initial point —the formulation and model validation of both the Spire approach and that of UL. In other words, even if L2 data is provided, we still need to reproduce the computational processes for all models to minimize differences from the starting point.

4.4.1 Spire's selection and model formulation validation

The Table 4.6 summarizes the parameters that Spire chose for their altimetry L2 products.

Table 4.6: Spire L2 parameters and models selection

Parameters:		**Selection:**
Phase unwrapping		Spire method
Tropospheric delay		GFS
Reference surface	MSS	DTU18
	Tides	TPXO9
QC filters	Coherency	0.065
	Continuity	5 sec
Frequency combination		L_1
Filter	Type	Savitzky-Golay
	Order	3
	Window	50 km

The altimetry results with the Spire parametrization corresponds to a 17.4 cm and 25.7 cm median RMSE and standard deviation between the height from WGS84 and the reference surface.

Ideally, when processing the data using the identical initial data, parameters, and models, and assuming everything is correct and optimized, the software we developed in the Geophysics Laboratory (GL) should obtain the same altimetry results as those reported in the L2 Spire data. Then, after processing and obtaining the results, we made a direct comparison to the altimetry data, demonstrating an agreement of **0.76 mm** and **1.20 mm** of RMSE and SD from the values obtained in the previous results, respectively. This comparison validates and established an initial point from which we can individually analyze and study the different parameters involved in obtaining altimetry measurements.

In this study we analyze and compare mainly the parameters and estimates listed below:

- Phase unwrapping methods
- QC filter (continuity windows)
- Troposphere delay models
- Mean Sea Level and Tidal models

- Ionospheric frequency combinations and the filter's type, order and window.

Each modified parameter will be analyzed in the following subsections.

4.4.2 Phase unwrapping methods and Continuity QC filter windows

Phase unwrapping is a process, as mentioned previously, that consists to unwrap the residual phase that is compressed between $-\pi$ and π. Even if the process might appear simple, it is not when there is noise on the signal. That is why it is important to use a robust method, in order to not induce errors while unwrapping the phase residuals that will cause accumulated error in the final unwrapped phases.

The phase unwrapping used in GL is an algorithm that unwraps the radian phase angles. Whenever the jump between consecutive angles is greater than or equal to π radians, unwrap shifts the angles by adding multiples of $\pm 2\pi$ until the jump is less than π. After this process the phase residual is corrected for the cycle slips, as explained in the Section 3.4. And finally the coherency criteria is applied as described in the Section 3.3.

Spire is using a method that combines phase unwrapping and cycle slip detection and correction in point by point analysis. The process involves geometry differences (L_1 and L_2) and a smoothing window of 2 sec to detect and to correct cycle slips and as well differentiate phase noise than a cycle slip after the phase unwrap. After that, the reflected signal is taken to perform an analysis on the geometric differences one more time to apply the coherency and continuity filters. The coherency threshold is set to 0.065 on the standard deviation of the smoothed 3 sec moving windows, and the continuity filter selected for Spire is 5 sec continuity coherent measurements.

In this analysis we compare the method from UL and Spire the phase unwrapping and the coherency criteria, specifically the continuity criteria.

Comparing the altimetry results reveals slight differences between the 5-second and 3-second windows, indicating a low presence of short coherent segments. Additionally, the threshold value is a critical parameter, as it significantly influences the number of coherent observations collected—up to 32% fewer coherent samples compared to the results obtained by Spire. Decreasing the threshold value improves the altimetric results, never-

Table 4.7: Phase unwrapping methods, including the coherency and continuity filters, i.e. quality control filters

Window/Threshold	RMSE	SD	Coherent sample gain
5 sec/0.065 (Spire)	17.8 cm	25.7 cm	0 %
5 sec/0.065	16.7 cm	25.6 cm	-0.4%
3 sec/0.065	16.7 cm	25.4 cm	1.7%
3 sec/0.06	16.0 cm	25.3 cm	1.5%
3 sec/0.055	14.9 cm	24.4 cm	-5.1%
3 sec/0.05	14.1 cm	23.7 cm	-9.4%
3 sec/0.0325	12.0 cm	23.5 cm	-32%
3 sec/0.125	22.6 cm	39.9 cm	14.5 %
3 sec/0.25	27.3 cm	73.1 cm	31.3 %

theless, it comes at the cost of losing valuable measurements. On the other hand, with a coherency threshold of 0.25, we obtain 31% more measurements, but the standard deviation increases to 73 cm.

We find that the optimal solution, without losing many measurements (5%), is a threshold of 0.055. At this value, we see an improvement of approximately 3 cm in the RMSE and 1 cm in the standard deviation.

4.4.3 Tropospheric models

Estimating the tropospheric delay is an important factor, as described in 3.5.2. Moreover, for low elevation angles, this correction is particularly significant in the case of the GG-R signal, as it needs to pass through a large portion of the atmosphere not just once but twice for the reflected signal. Therefore, the correct selection of the model is essential, especially for the low elevation angles. This is why we will not only try different tropospheric models but also combinations of them to observe the performance across different elevation angle ranges.

The Table 4.8 summarizes the comparison between the tropospheric models presented in 3.5.2. Additionally, in rows 4 to 6, different ranges of elevation angles (from 5° to 30 °) and tropospheric models have been selected to observe the influence of them for various ranges. Influenced by the elevation angle range comparison, Figure 4.14, in which we can find a comparison with the three models we analyze with respect to the elevation angle and color

coded by the number of observations. In these three plots, we can observe the differences between the models, where the larger differences take place at the lower elevation angles, e.g., in the Figure 4.14 (a) where come samples reach 2.5 m differences between GFS and VMF3/GPT3 differences. As we can also observe in the Table 4.8, the closer differences are between the two model GFS and UNB3m. However, the results seen in the Table 4.8 shows no improvement while using combined models.

The models that in fact presented the better results are GFS and UNB3m, which are models that present a better tropospheric ray tracing. However, GFS requires more computational time to estimate the tropospheric delay while UNB3m is very efficient.

Table 4.8: Tropospheric delay estimation models

Selection	**RMSE**	**SD**
GFS	17.8 cm	25.7 cm
VMF3/GPT3	19.5 cm	35.6 cm
UNB3m	18.9 cm	36.7 cm
VMF3/GPT3 >15° UNB3m<15 °	20.8 cm	36.7 cm
VMF3/GPT3 >10° UNB3m <10°	20.7 cm	41.4 cm
GFS >10° UNB3m <10°	18.4 cm	37.4 cm

4.4.4 MSS and Tidal models

The open-water reference surface model must be constructed using the MSS and the tidal models. In this section, we list and analyze different reference surface models from various institutions to observe their influence on the altimetric retrievals.

Specifically, for GG-R technique, the reference surface model plays an important row in the final altimetry product. As explained in the Section 3.6, the GG-R technique used in this dissertation produces relative values that must be adjusted to this reference surface model.

The MSS and tidal models are also described in Section 3.6.

Overall, we can consider that all MSS and tidal models are performing within an acceptable range, with maximum differences of approximately 1 cm in RMSE and 6.5 cm in SD. We

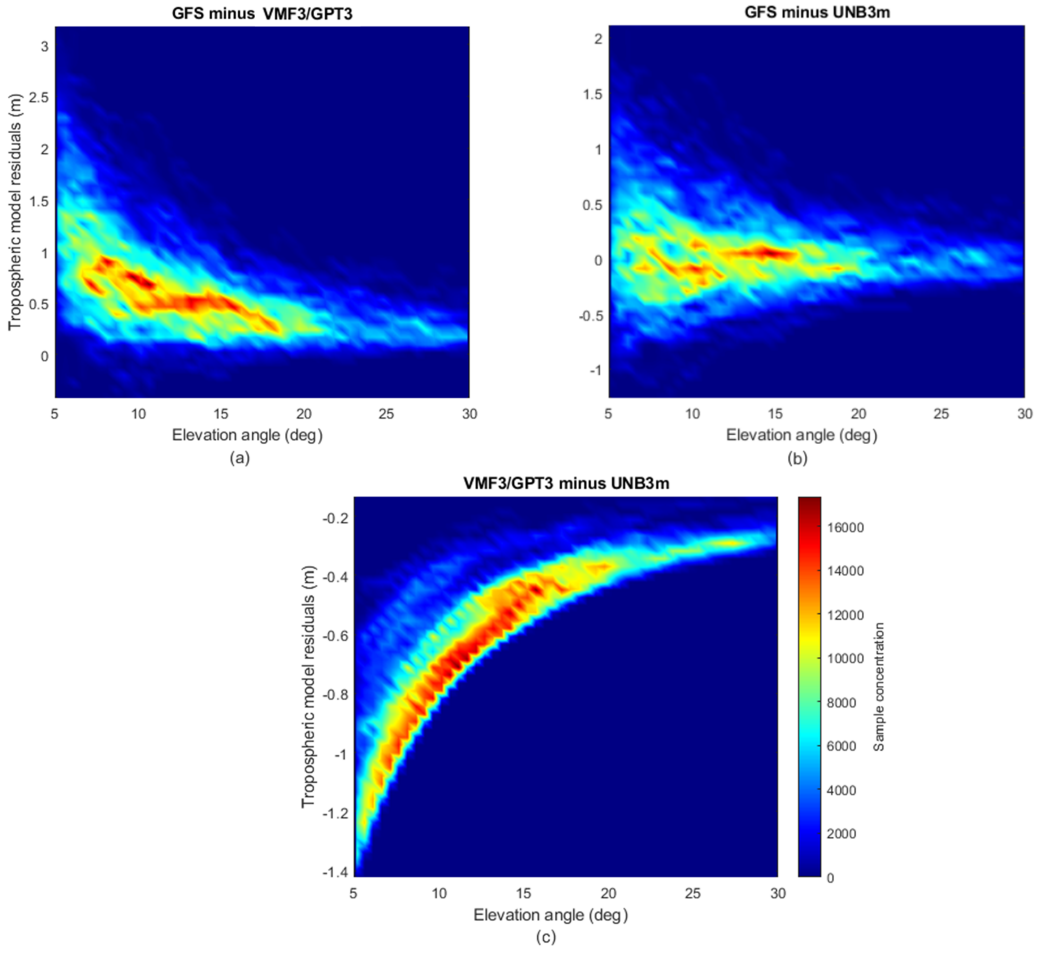

Figure 4.14: Tropospheric model delay differences vs. elevation angle in Hudson Bay from July to September 2021. (a) GFS model minus VMF3/GPT3 (b) GFS minus UNB3m (c) VMF3/GPT3 minus UNB3m

Table 4.9: Reference surface models selection

Selection	RMSE	SD
MSSDTU18 & TPXO9v1	17.8 cm	25.7 cm
MSSDTU18 & TPXO9v5	16.6 cm	25.1 cm
MSSDTU21 & TPXO9v1	18.2 cm	30.1 cm
MSSDTU21 & TPXO9v5	16.4 cm	25.1 cm
MSSDTU18 & Arc2kmTM	18.6 cm	25.9 cm
MSSDTU21 & Arc2kmTM	18.7 cm	25.9 cm
MSS-CNES-CLS2022 & TPXO9v5	17.4 cm	25.1 cm
SIO CNES-CLS15 DTU15& TPXO9v5	16.2 cm	23.6 cm
SIO CNES-CLS22 DTU21& TPXO9v5	15.9 cm	23.5 cm

also observe that TPXO9v5 outperforms TPXO9v1, which has fewer constituents; this is especially evident in the SD, where we find a 5 cm difference between the tidal models when applied with the MSSDTU21 model. Additionally, we find that the tidal model Arc2kmTM does not perform well in either SD or RMSE.

Among the MSS models, MSSDTU21 and the hybrid models SIO CNES-CLS15 DTU15 and SIO CNES-CLS22 DTU21 presented the best results, showing a reduction in RMSE of more than 1 cm compared to other models. Notably, the SIO CNES-CLS22 DTU21 model also exhibited a better standard deviation, with an improvement of approximately 2 cm in both SD and RMSE from the Spire initial parameters.

4.4.5 Ionospheric frequency combinations

The study in Section 4.3 was inspired by this analysis, where we compare the altimetry differences between the variances obtained from the ionospheric-free and frequency-specific methods, as explained in Section 4.3.2.

Table 4.10 summarizes the altimetry results of the ionospheric-free combination and of the three other possible of frequency specific method's combinations. The largest difference is observed between the ionospheric-free combination and the frequency-specific methods, with approximately 8 cm difference of the RMSE. However, the ionospheric-free combination SD is minimally smaller (7 mm) than the other methods.

Along the different frequency-specific methods, we find little difference between them.

However, surprisingly, even though the RMSE of the average L_1 and L_2 shows an improvement of 5 mm compared to using only L_1 for the smoothing, the standard deviation increases by 2 mm when using the average of L_1 and L_2 in the frequency-specific methods (Table 4.10).

Table 4.10: (row 1) Ionospheric-free combination. Frequency specific methods; the first method (row 2) uses only L_1 GPS frequency, the second method (row 3) L_2 and the third method is an average of L_1 and L_2 methods.

Method	**Frequencies**	**RMSE**	**SD**
Ionopheric-free combination	Encapsulated L_1 and L_2	25.8 cm	25.0 cm
Frequency-specific	L_1	17.8 cm	25.7 cm
	L_2	18.2 cm	25.7 cm
	Average L_1 and L_2	17.3 cm	25.9 cm

The results in Table 4.11 show that the moving median filter consistently achieves the lowest RMSE and SD values across all window sizes, particularly at 10 km, where it reaches a minimum RMSE of 17.5 cm and SD of 25.2 cm, highlighting its superior performance. For larger window sizes (e.g., 50–100 km), the moving mean filter tends to produce higher RMSE and SD values, indicating reduced performance in smoothing over extended distances. Overall, the Savitzky-Golay filters (Orders 1–5) show stable results but slightly higher errors compared to the moving median, emphasizing the moving median's effectiveness in minimizing deviations in GNSS-R altimetry.

To make the results in the Table 4.11 more visual, we provide examples of various filters, specifically the Savitzky-Golay filter (order 3), moving mean, and moving median, applied over a range of 1 km to 100 km, compared to unfiltered data (see Figure 4.15).

Table 4.11: Altimetry results using various filters and physical kilometer windows from frequency-specific method

Window		S. Golay Order 1	S. Golay Order 2	S. Golay Order 3	S. Golay Order 4	S. Golay Order 5	Mov. Mean	Mov. Median
1 km	RMSE	18.9 cm	20.0 cm	20.1 cm	21.4 cm	21.7 cm	18.8 cm	18.8 cm
	SD	25.5 cm	25.3 cm	25.2 cm	25.1 cm	25.1 cm	25.5 cm	25.4 cm
5 km	RMSE	18.0 cm	18.3 cm	18.3 cm	18.7 cm	18.7 cm	17.8 cm	17.7 cm
	SD	25.6 cm	25.6 cm	25.6 cm	25.5 cm	25.5 cm	25.6 cm	25.6 cm
10 km	RMSE	17.9 cm	18.0 cm	18.2 cm	18.2 cm	18.2 cm	17.7 cm	**17.5 cm**
	SD	25.7 cm	25.6 cm	25.6 cm	25.6 cm	25.6 cm	25.6 cm	25.6 cm
20 km	RMSE	18.0 cm	17.8 cm	17.9 cm	18.1 cm	18.1 cm	18.0 cm	17.7 cm
	SD	25.7 cm	25.7 cm	25.7 cm	25.6 cm	25.6 cm	25.5 cm	25.4 cm
25 km	RMSE	17.9 cm	17.8 cm	17.8 cm	18.0 cm	18.1 cm	18.0 cm	17.7 cm
	SD	25.7 cm	25.7 cm	25.7 cm	25.6 cm	25.6 cm	25.4 cm	25.3 cm
50 km	RMSE	18.4 cm	17.9 cm	17.8 cm	17.9 cm	17.9 cm	19.0 cm	18.4 cm
	SD	25.9 cm	25.7 cm	25.7 cm	25.7 cm	25.7 cm	25.4 cm	**25.2 cm**
100 km	RMSE	18.6 cm	18.2 cm	18.1 cm	18.0 cm	18.1 cm	21.4 cm	21.2 cm
	SD	26.1 cm	25.8 cm	25.8 cm	25.7 cm	25.7 cm	31.3 cm	30.9 cm

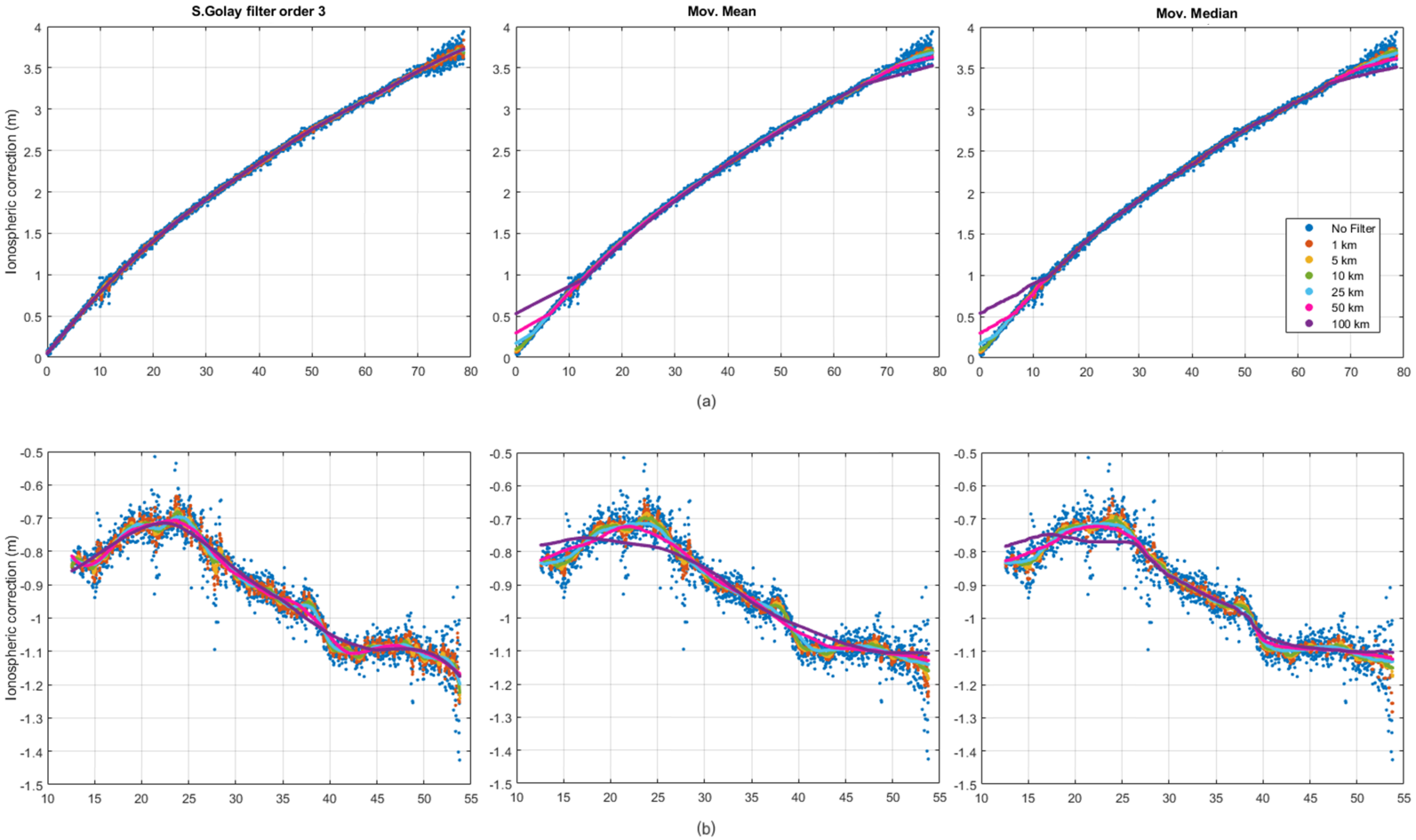
S.Golay filter order 3
Mov. Mean
Mov. Median
Ionospheric correction (m)
No Filter
1 km
5 km
10 km
25 km
50 km
100 km
(a)
Ionospheric correction (m)
(b)

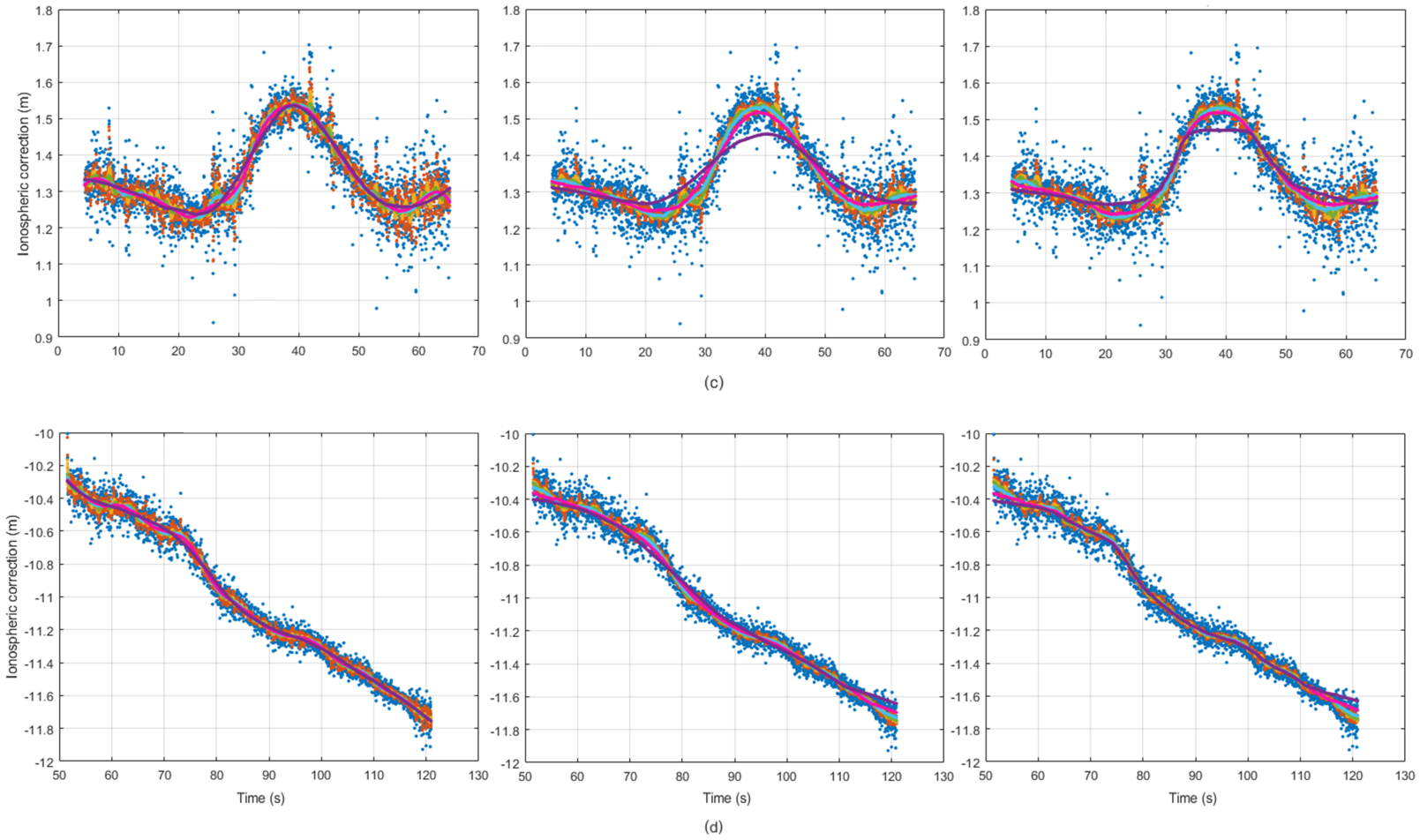

Figure 4.15: Graphical examples of the GPS L_1 frequency specific correction for different window ranges (from 1 to 100 km) and three different smoothing filters; Savitzky-Golay filter (Order 3) and moving Mean and Median window

4.4.6 Optimal combination

After conducting individual analyses, we decided to explore the most optimal solution for retrievals as described in Table 4.4.6. Here, the Root Mean Square Error (RMSE) and the Standard Deviation (SD) are 13.6 cm and 22.4 cm, respectively. However, there is a sample loss of 4.2% compared to the total number of coherent samples from the initial values provided by Spire.

Compared to the initial results obtained with the parameters chosen by Spire, we observed improvements in the height retrievals and reference surface model differences: 4.2 cm for the Median RMSE and 3.3 cm for the SD. Despite minimal coherent data loss, these changes represent significant reductions of 24% and 13%, respectively.

Table 4.12: Parameters and models for the most optimal solution

Parameters:		**Selection:**
Phase unwrapping		GL
Tropospheric delay		GFS
Reference surface	MSS	SIO CNES-CLS22 DTU21
	Tides	TPXO9v5
QC filters	Coherency	0.055
	Continuity	3 sec
Frequency combination		L_1 and L_2
Filter	Type	Median
	Order	-
	Window	10 km

4.5 Comparison of Sea Surface Height Anomaly Measurements from GG-R and Satellite altimetry Missions

The measurement of SLA is crucial for understanding complex oceanic processes, climate variability, and key measurements such as sea level changes, ocean circulation patterns, and the impacts of meteorological and climate phenomena.

For decades, satellite-based Radar Altimetry (RA) has been pivotal in collecting SLA data [46]. Missions like Jason-3 and Sentinel-3 have revolutionized our ability to monitor SSH achieving accuracy within a few centimeters and providing global coverage. These advancements have significantly enhanced our understanding of sea level variations [4, 87], sea-ice distribution [88], and ocean dynamics [89].

Since its initial concept [27] and first experiment [90], ocean altimetry using GNSS-R has evolved through different platforms, achieving centimeter-level in airborne and ground-based experiments [91, 92, 93, 94] and decimeter-level precision in space-borne missions [14, 75]. Precision altimetry measurements with GNSS-R require specific geometries known as GG-R. Coherent measurements are typically obtained from smooth surfaces such as ice, sea ice, and calm waters when the elevation angle from the specular point is between 5° and 30°, as demonstrated with the Spire grazing angle satellite constellation [14], which is used in this research.

To improve GG-R measurements and achieve precision comparable to satellite RA data, it is essential to compare SLA from both sources. This comparison helps discerning the advantages and limitations of each technique and leverages their measurements for more comprehensive SLA datasets.

This section presents a detailed investigation comparing SLA measurements from satellite altimetry missions (Sentinel-3A and 3B, Saral, and Cryosat-2) with data derived from Spire Global Inc.'s GG-R satellite constellation, using exclusively dual-frequency GPS measurements. Additionally, we compare gridded SLA products disseminated via the CMEMS project with the those from GG-R retrieval to provide an additional grid value comparison. It is important to mention that, $SLA_{GG\text{-}R}$, SLA_{RA} and SLA_{CMEMS} are highly noted in this section

for the differences between the GG-R, RA and CMEMS average grid [74] altimetric values with respect to the reference surface. All height retrievals in this study are referenced to WGS84 ellipsoid. Figure 4.16 illustrates the GG-R geometry and the relationship between SSH and SLA.

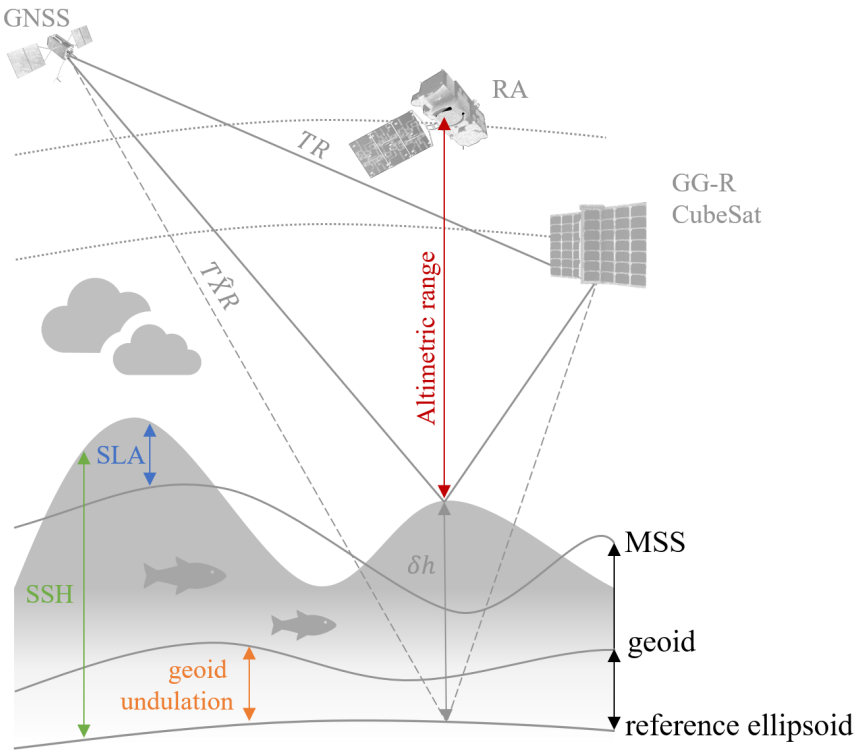

Figure 4.16: GG-R geometry and the definition of SSH with respect to the reference ellipsoid, illustrating the deviation of the SSH from the MSS as the SLA.

The rest of the section is structured into 4 parts. Section 4.5.1 provides a detailed overview of the datasets and outlines the analytical approaches. The results section (4.5.2) is divided into 3 subsections: the first one compares SLA from satellite altimetry missions (SLA_{RA}) with Spire GG-R retrievals ($SLA_{GG\text{-}R}$), the second one presents a comparison of collocated GG-R profiles, and the last one focuses on the coverage and signal coherency of the GG-R measurements. Section 4.5.3 discusses the role of GG-R as an additional measurement source. Finally, the findings and summary are presented in Section 4.5.4.

4.5.1 Data description and model formulation

A brief description of the different altimetry satellites is given in this section. Initially, our research involved an examination of several satellite altimeters, including Jason-3 and HY-2. However, we found that Sentinel-3A, Sentinel-3B, Saral, and Cryosat-2 had more collocated events with GG-R. As a result, we selected these satellites for comparisons with GG-R events. Table 4.13 summarizes all satellites altimetry missions used in our study.

Cryosat-2

Cryosat-2 was launched on 8th of April 2010 by ESA. It is one of their Earth Explorer missions designed to study Earth's polar ice. Equipped with a radar altimeter known as the SAR Interferometric Radar Altimeter (SIRAL), Cryosat-2 operates in a LEO at an altitude of approximately 717 km and an inclination of 92°. The SIRAL altimeter allows Cryosat-2 to obtain measurements of ocean surfaces height with an accuracy of 6 cm [95]. It provides unique data for monitoring polar ice conditions and understanding the dynamics of ice masses [96].

Satellite with ARgos and ALtika

Saral is a collaborative satellite mission between the Indian Space Research Organisation (ISRO) and the CNES. Launched on February 25, 2013, Saral is specifically designed for precise altimetry measurements of the ocean surface. Operating in a polar SSO of 98.54° at an altitude of approximately 781 km and a repeat cycle of 35 days, Saral carries two main instruments: the Altika altimeter and the ARGOS-3 payload [97]. The Altika altimeter provides measurements of sea surface height with an accuracy of 3 to 5 cm [97].

Sentinel-3A

Sentinel-3A, a radar altimeter of the ESA Copernicus program, was launched on February 16, 2016. Operating in a polar SSO of 98.65° at an altitude of around 815 km, it completes one orbit approximately every 101 minutes with a repeat cycle of 27 days. Equipped

with advanced instruments such as the Ocean and Land Colour Instrument (OLCI), Sea and Land Surface Temperature Radiometer (SLSTR), and Synthetic Aperture Radar Altimeter (SRAL), Sentinel-3A systematically captures high-resolution data on ocean color, sea surface temperature, and sea surface height. [98].

Sentinel-3B

Launched on April 25, 2018, Sentinel-3B serves as the twin satellite of Sentinel-3A, featuring identical orbits and instruments. This similarity enabling consistent and complementary data collection between the two missions. Altimetry data collected from both Sentinel-3A and Sentinel-3B missions has an accuracy within the range of 2 to 3 cm [95]. The combined efforts result in a more frequent revisit time and a broader coverage area, thereby enhancing the program's ability to monitor and manage environmental changes on a global scale [98].

Table 4.13: Information on altimetry missions Sentinel-3A/B [98], Saral [97], and Cryosat-2 [96]

	Sentinel-3A/B	**Saral**	**Cryosat-2**
Altitude	814.5 km	781 km	717 km
Inclination	98.65°	98.54°	92°
Period	100.99 min	100.54 min	100 min
Repeat Cycle	27 days	35 days	369 days
Agency	ESA	ISRO/CNES	ESA
Date deployed	2016.02/2018.04	2013.02	2010.04
Accuracy	2-3 cm	3-5 cm	6 cm

Satellite altimetry principle

Satellite altimeters function by measuring the time taken for a radar pulse to travel from the satellite to the Earth's surface and back. This time delay is directly related to the distance between the satellite and the Earth's surface. Different corrections must be estimated and applied to the signal. One critical correction addresses ionospheric delays in the radar signal. Additionally, tropospheric corrections are necessary to account for atmospheric conditions below approximately 50 km. Sea state bias corrections are then applied to mitigate inaccuracies arising from the roughness of the sea surface. Finally, geophysical corrections

refine measurements by addressing sea level fluctuations caused by factors such as tides and other relevant geophysical phenomena. These corrections collectively contribute to the accuracy and reliability of satellite altimetry data.

Alongside the precisely computed altitude of the satellite (H), SSH can then be derived as [99]:

$$SSH = H - h_{corr} \tag{4.2}$$

where h_{corr} represents the corrected altimeter range accounting for environmental conditions mentioned earlier. The accuracy of this correction is crucial for ensuring the precise retrieval of the SSH.

GG-R data and models

The tropospheric delay is corrected using VMF3 and GPT3 model [61]. The reference surface model in the Reference Surface Adjustment (RSA) is the hybrid MSS that combines three different reference MSSs over the ocean: the SIO MSS [67] in the open ocean, CNES CLS 2015 MSS [100] in coastal areas and the Antarctic region, and DTU15 MSS [101] in Arctic regions. The MSS is then corrected for ocean tides based on the TPXO9-atlas [81] and is used here as the reference surface model. Table 4.14 summarizes all models and methods used in this study for GG-R precision altimetry retrievals.

Table 4.14: Models and methods used in this study for altimetric retrieval

Category	**Models or methods**
Ionospheric delay	Frequency specific
Tropospheric delay	VMF3/GPT3
Reference surface	MSS_CNES_CLS_15
Ocean tide	TPXO9
Cycle slip	Geometry-free combination
Clock errors	Reflected and direct geometric differences

4.5.2 Results

The findings of this study are presented in three distinct subsections. The first section is dedicated to the outcomes of the altimetry comparison between radar altimetry and GG-R measurements. Subsequently, the second subsection offers a similar analysis but focuses solely on GG-R measurements. The final section provides an examination of the missions coverage and GG-R coherency distribution.

In this context, it is essential to define several key terms. The notation GG-R refers to grazing angle retrievals, while RA denotes measurements obtained from radar altimeters. The subscript CMEMS corresponds to the SLA grid product, which averages altimetry data from TOPEX-Poseidon, Jason-1, Jason-2, Jason-3, and Sentinel 6-A satellite altimeters over the period from 1 January 1993 to 8 September 2023 [74]. Furthermore, the altimetry results are presented asRMSE of different parameters. The first comparison involves Height RMSE, which refers to the RMSE between height retrievals from WGS84 for both GG-R and RA measurements. The second comparison focuses on the RMSE of SLA, defined as the RMSE between the height retrievals from GG-R and RA and the reference surface. Finally, the last type of comparison corresponds to the RMSE of SLA between the gridded sea surface height from CMEMS and the GG-R and RA solutions.

Comparison of Satellite altimetry missions with Spire data

This section delves into a comparison of SLA_{RA} between the Sentinel-3A/3B, Saral, and Cryosat-2 radar altimetry missions and GG-R measurements from the Spire constellation ($SLA_{GG\text{-}R}$). The study period spans from May 2019 to October 2021, focusing on events that closely match in both time and space. Specifically, we identify and use collocated events with a 1-day temporal difference and an average spatial separation of 10 km for this analysis.

Figure 4.17 illustrates the global distribution of tracks used for comparing RA with Spire GG-R measurements. The Regions Of Interest (ROI) are chosen according to Spire's implementation of data filtering starting from August 2020 and focusing on North Pole (north of 40°N), South Pole (south of 50°S), the Indonesian archipelago, and the Gulf of Mexico.

Further discussion on Spire mission coverage is provided in subsection 4.5.2.

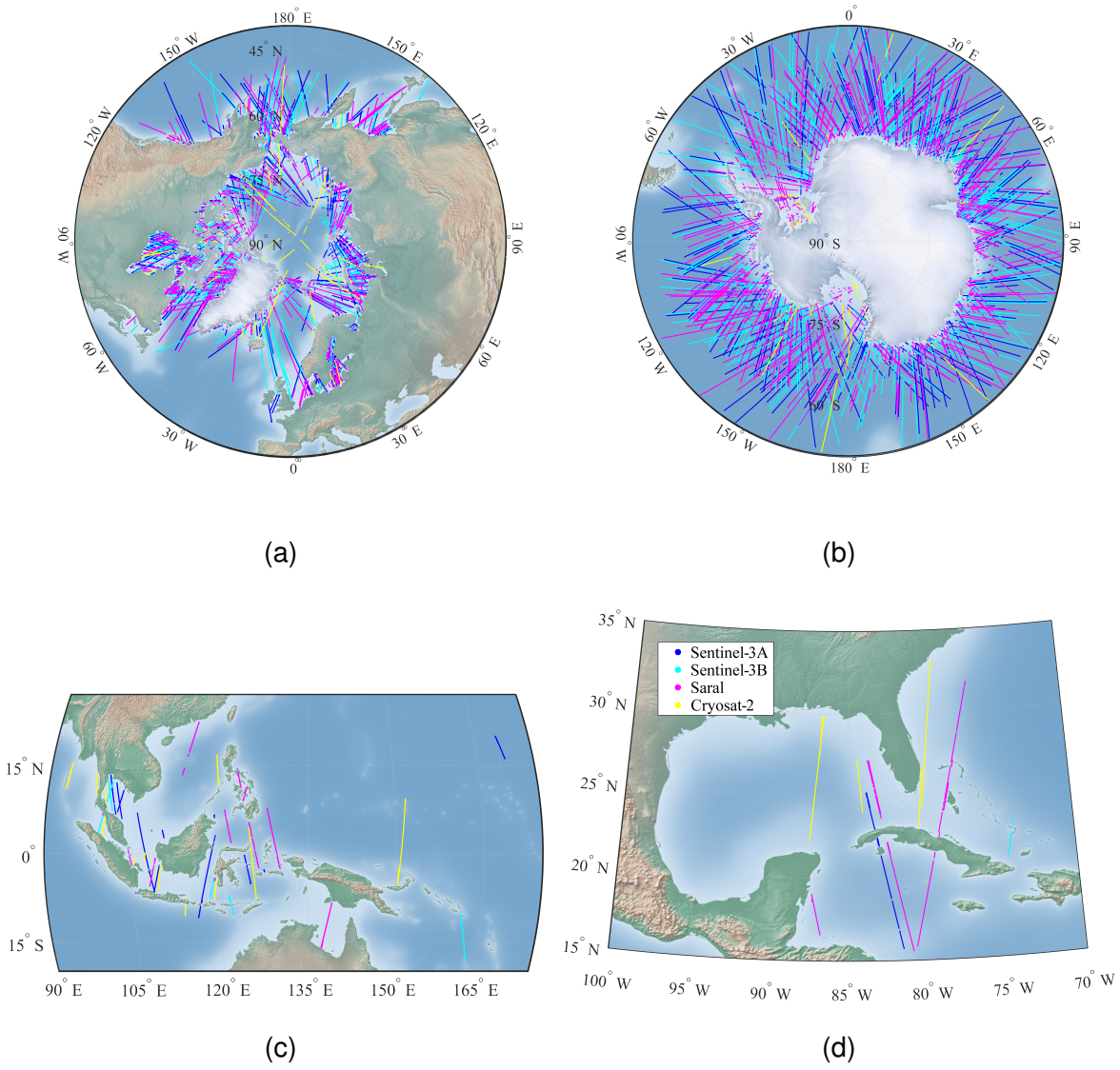

Figure 4.17: Identified tracks for the comparison between satellite altimetry and Spire GG-R measurements in the North Pole (a), South Pole (b), the Southeast Asian Seas (SEAS) (c), and Gulf of Mexico and surrounding areas (d). Dark blue, light blue, magenta, and yellow represent Sentinel-3A, Sentinel-3B, Saral, and Cryosat-2, respectively.

Table 4.15: Comparison of GG-R and satellite altimetry measurements. The second row represents the RMSE between GG-R altimetric retrieval and collocated RA measurement; the third raw ($SLA_{GG\text{-}R\ vs.\ RA}$) indicates the RMSE differences of estimated sea level anomaly derived from GG-R height profile and RA retrieval; the fourth row ($SLA_{GG\text{-}R\ vs.\ CMEMS}$ RMSE) shows the RMSE differences between $SLA_{GG\text{-}R}$ and SLA derived from CMEMS grid data (SLA_{CMEMS}), the last row represents the RMS differences between the SLA derived from the radar altimeter (SLA_{RA}) and SLA_{CMEMS}.

	Sentinel-3A	**Sentinel-3B**	**Saral**	**Cryosat-2**	**Multi-mission**
Collocated profiles	888	910	959	114	2871
Height RMSE (cm)	76.2	82.0	87.0	88.0	82.4
$SLA_{GG\text{-}R\ vs.\ RA}$ RMSE (cm)	40.0	46.7	54.0	41.9	46.8
$SLA_{GG\text{-}R\ vs.\ CMEMS}$ RMSE (cm)	37.5	35.7	36.3	37.8	36.6
$SLA_{RA\ vs.\ CMEMS}$ RMSE (cm)	4.9	5.3	5.1	5.4	5.1

Table 4.15 presents a comparison between the retrievals from the four radar altimeters and those from Spire GG-R measurements. This table contains the number of collocated tracks within an average distance of 10 km and 1 day apart: for example, 888 collocated tracks between Sentinel-3A and GG-R, and 114 between Cryosat-2 and Spire GG-R (first row). In terms of RMSE comparison, the height from WGS84 differences between GG-R profiles and RA measurements (second row) generally exceed the RMSE of $SLA_{GG\text{-}R}$ and SLA_{RA} (third row). Specifically, the RMSE of sea surface height between Saral RA and GG-R is 87.0 cm, whereas it is 54.0 cm for that of SLA from GG-R and Saral measurements. The multi-mission SLA comparison (Table 4.15, fifth column) shows an agreement of 46.8 cm with 2871 collocated tracks between the GG-R and all four satellite altimetry missions. This column aggregates the statistics of all RA missions and GG-R measurements. Additionally, the table compares $SLA_{GG\text{-}R}$ and SLA_{RA} with that post-processed daily grid data from CMEMS [74]. Similar results are observed across all missions. For instance, while the RMSE of SLA between GG-R and Sentinel-3A is 37.5 cm (fourth row), it is 4.9 cm for that of Sentinel-3A and CMEMS (last row). This comparison highlights that while GG-R operates on a decimeter scale, the RA approach achieves accuracy at the centimeter level, with values of 36.6 cm and 5.1 cm, respectively. This is because small delay errors map into large altimetric errors in GG-R [102, 103, 104], and it is more affected by atmospheric effects [75, 105]. It is important to clarify that the statistics in the fourth row and fifth row represent

GG-R tracks and RA collocated measurements, respectively, with their respective altimetry missions in each column, and compared with the gridded SLA data (SLA_{CMEMS}) data [74]. The lower values observed in the fourth row, compared to the fifth, can be attributed to the fact that the SLA grid from CMEMS represents an averaged dataset derived from multiple RA missions (TOPEX-Poseidon, Jason-1, 2 and 3 and Sentinel 6-A), spanning the period from 1 January 1993 to 8 September 2023 [74].

To illustrate this comparison further, four examples from different satellite missions and regions are selected. Figures 4.18 show two collocated events from all four satellite altimeters covering the North and South polar regions, Gulf of Mexico, and the Indonesian archipelago. Figure 4.18a provides the locations of these tracks. The physical distance between the collocated events varies from 0 to 25 km (Figure 4.18b), while the SP elevation angle ranges from 5° to 25° (Figure 4.18c). The GG-R 50 Hz height from WGS84 (black dots), the down-sampled 1 Hz GG-R height (orange line), and the radar altimeter data (blue line) are presented in Figure 4.18d, showing good agreement with the chosen reference model. Several discontinuities are also observed in the GG-R profiles, resulting from a loss of coherence, except for the profile in the North Pole. It should be noted that precision altimetry can be achieved by GG-R with coherent scattering. Furthermore, Figure 4.18e displays the $SLA_{GG\text{-}R}$ (50 Hz data as black dots and down-sampled 1 Hz data as the orange line), the SLA_{RA} (blue line) and SLA_{CMEMS} values (grey crosses).

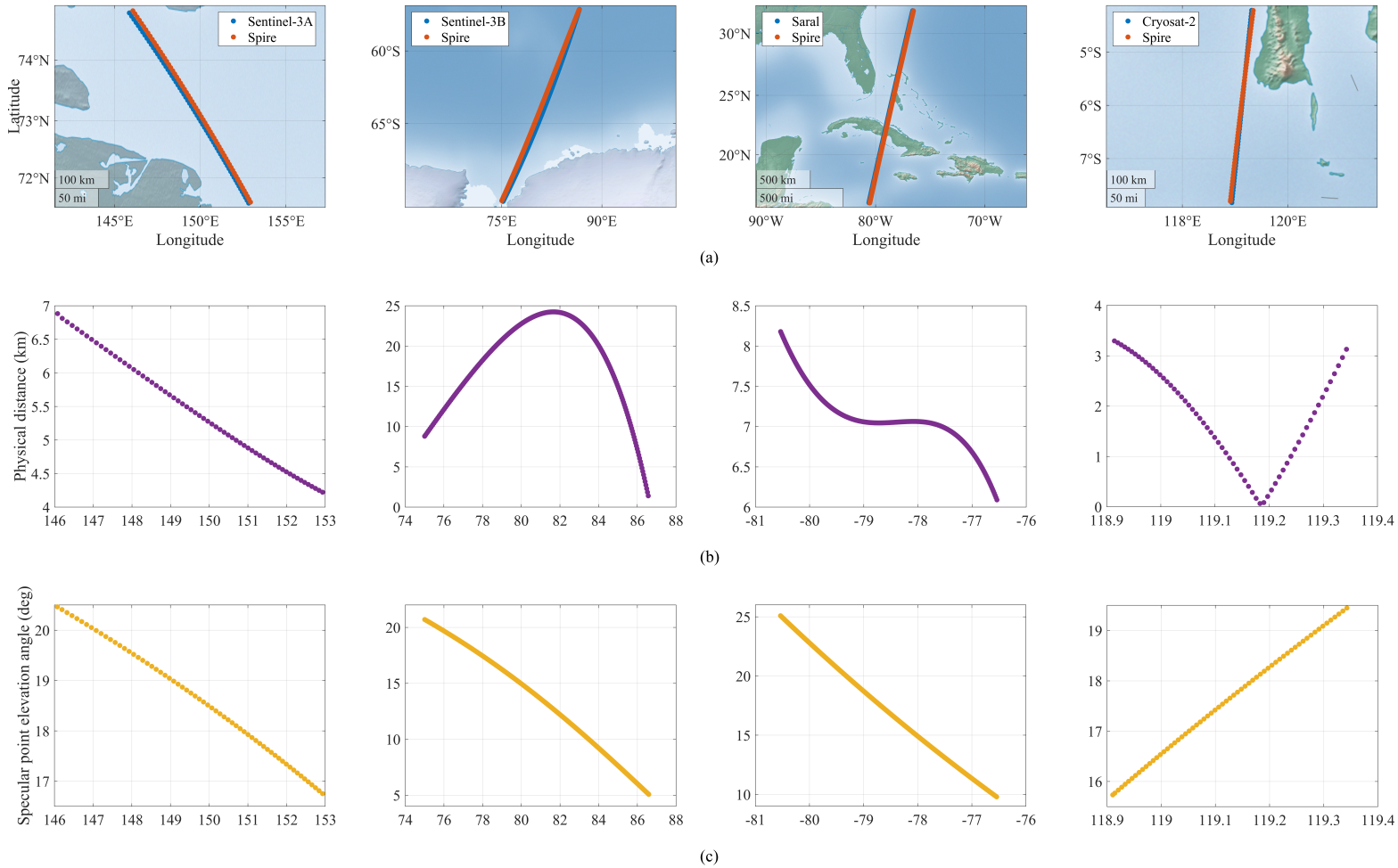
Sentinel-3A
Spire
Latitude
74°N
73°N
72°N
100 km
50 mi
145°E
150°E
155°E
Longitude
Sentinel-3B
Spire
60°S
65°S
75°E
90°E
Longitude
Saral
Spire
30°N
25°N
20°N
500 km
500 mi
90°W
80°W
70°W
Longitude
Cryosat-2
Spire
5°S
6°S
7°S
100 km
50 mi
118°E
120°E
Longitude
(a)
Physical distance (km)
(b)
Specular point elevation angle (deg)
(c)

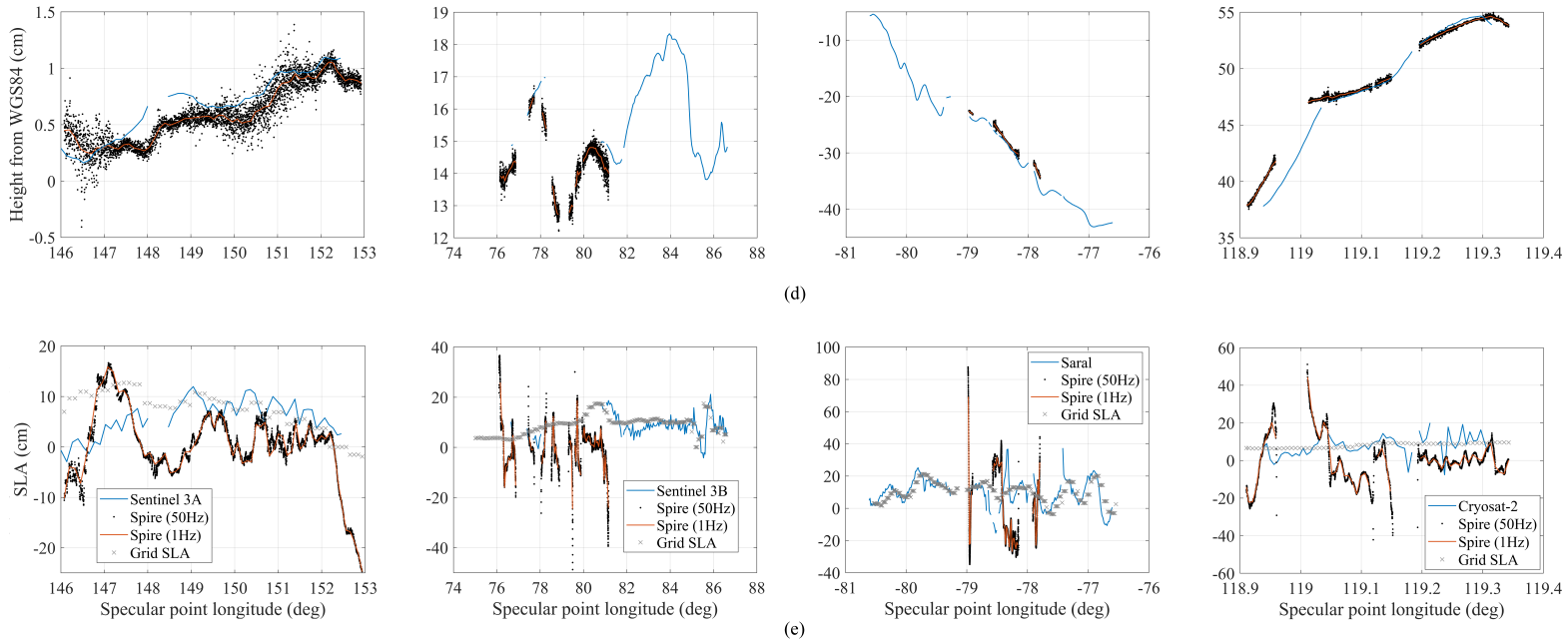

Figure 4.18: From left to right the examples from North and South Pole, Gulf of Mexico and Java Sea from Sentinel-3A, Sentinel-3B, Saral and Cryosat-2 respectively. (a) Locations of Sentinel-3A/B, Saral, and CryoSat-2 profiles (blue line) and Spire profiles (red line), (b) Physical distance between the collocated events in km, (c) SP elevation angle for the Spire GG-R track, (d) Absolute height w.r.t WGS84 of RA (blue line), GG-R 50 Hz (black dots), and GG-R 1 Hz (red line), and (e) SLA for each track compared with SLA derived from CMEMS grid data

The comparison results of these specific profiles are summarized in Table 4.16. The Cryosat-2 profile (last column) was generated on April 07, 2020 at 20:32:19 UTC (fourth row), while the GG-R profile from FM099 (first row) was generated from the GNSS transmitter Space Vehicle Number (SVN) 31 (second row) on April 08, 2020, at 01:44:15 UTC. The GG-R profile consists of four coherent segments (74% of the track) with durations of 9-sec, 20-sec, 5-sec, and 26-sec, respectively. The RMSE of $SLA_{GG\text{-}R}$ and SLA_{CMEMS} is 9.6 cm (sixth row), whereas it is 12.3 cm for that derived from RA measurements (seventh row). The RMSE analysis highlights differences in surface height retrievals between various datasets. For FM102 collocated with Sentinel-3A, the RMSE between the GG-R surface height retrieval and the Sentinel-3A data over a duration of 81 seconds is 13.4 cm (first column, fifth row). In comparison, the RMSE between the SLAGG-R and SLARA is lower, at 8.4 cm (eighth row). For FM101 collocated with Sentinel-3B, seven coherent segments (comprising 23% of the track) with durations ranging from 4 to 34 seconds show an RMSE of 14.5 cm (ninth row) between SLAGG-R and SLACMEMS. However, the RMSE between SLARA and SLACMEMS is substantially lower at 3.1 cm (tenth row). These results underline the varying accuracy across different retrieval methods and reference datasets.

Table 4.16: Comparison of GG-R and satellite altimetry measurements for the four selected tracks in different regions

	Sentinel-3A	**Sentinel-3B**	**Saral**	**Cryosat-2**
Spire FM	102	101	116	099
GPS PRN	27	09	30	31
Date and time (GG-R)	2021/08/09 09:40:48	2020/12/14 03:13:28	2021/06/30 15:53:13	2020/04/08 01:44:15
Date and time (RA)	2021/08/09 09:19:11	2020/12/13 02:38:58	2021/06/30 23:05:47	2020/04/07 20:32:19
Height RMSE (cm)	13.4	42.4	42.1	16.9
$SLA_{GG\text{-}R}$ RMSE (cm)	6.8	9.9	13.0	9.6
SLA_{RA} RMSE (cm)	7.8	8.6	23.0	12.3
$SLA_{GG\text{-}R\ vs.\ RA}$ RMSE (cm)	8.4	17.9	31.8	15.0
$SLA_{GG\text{-}R\ vs.\ CMEMS}$ RMSE (cm)	9.7	14.5	25.4	15.0
$SLA_{RA\ vs.\ CMEMS}$ RMSE (cm)	5.3	3.1	5.6	4.9

Upon general analysis of these four examples, the RMSEs of $SLA_{GG\text{-}R}$ and SLA_{RA} (rows 6 & 7) are lower than the RMSE differences between the sea surface height measurements

and SLA retrievals (row 5). These residuals for all four FMs highlight the limitations in the reference surface model. However, such differences can be seen when comparing the SLA_{CMEMS} from GG-R and RA. Additionally, higher RMSE values are observed for sea surface heights for FM101 and FM116, which are collocated with Sentinel-3B and Saral track examples, respectively. That could be a result of tropospheric mismodeling, as these two track examples have lower elevation angles compared to the other two examples, or residual geometry arising from the total phase differences between the direct and reflected signal errors, such as receiver clock errors, or the presence of ice.

GG-R collocated events

Hereafter, we propose a comparative analysis specifically focusing on comparing collocated GG-R measurements worldwide. The altimetry assessment is based on collocated GG-R height profiles occurring when two FMs capture reflected signal from the same area, with a maximum of 30 seconds apart. The focus is on maintaining a close physical distance, averaging around 10 km. The objective is to detect sea surface reflections from the same GPS satellite by two consecutive Spire FMs almost simultaneously. This would provide insight into the potential systematic differences among GG-R retrievals, helping to understand the noise of the Spire GG-R system.

Figure 4.19 illustrates the geophysical coverage of the collocated tracks found, a total of 938 profiles spanning from May 2019 to October 2021. Due to the map projection, measurements near the poles are not depicted in this figure, particularly those above latitudes exceeding 85°N, while those in the South Pole are less represented due to the absence of measurements below 85°S. It is also noteworthy that, as of June 2020, regions of interest were designed to implement data geo-filtering, aiming to limit data-collection demands on each FM for regions such as the North and South Poles, the Indonesian archipelago, and the Gulf of Mexico areas. This is particularly important due to the number of FMs available before September 2020 (Table 3.1).

The altimetry comparison is conducted using the closest neighbor technique. The median RMSE of the $SLA_{GG\text{-}R}$ comparison indicates an agreement of 25.2 cm with a standard

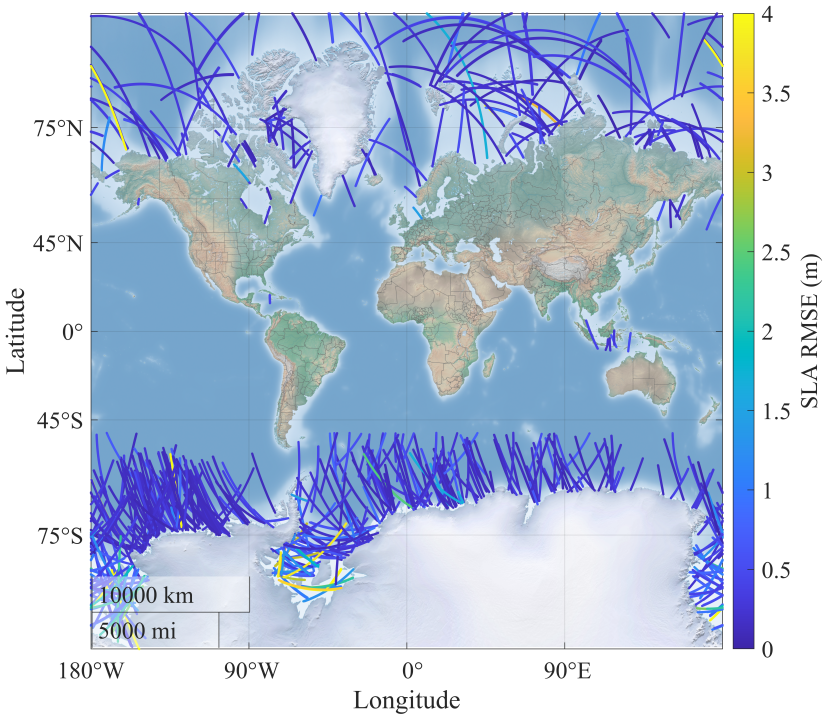

Figure 4.19: Geophysical coverage and SLA RMSE of the 938 GG-R collocated tracks, with a maximum time difference of 30-sec between each track pair and an average physical distance of 10 km among all the Spire data available for this study.

deviation of 25.4 cm. The majority of RMSE height differences between the reference and the collocated tracks fall below 60 cm: 29% of the tracks exhibit differences lower than 20 cm, 38% between 20 and 40 cm and, 17% 40 and 60 cm. The remaining 16% of tracks exceeding 1 m are primarily located in the Ronn and Ross ice shelves (the biggest shelves in Antarctica) with a few near the coast of Antarctica. In these instances, the larger discrepancies can be attributed to the limitations of the reference surface model in the area. Moreover, no seasonal changes in the comparison of the height and the reference surface model can be seen for the summer and winter periods (from January to June and from July to December) for both the northern and southern hemispheres, with RMSE values of 24.9 cm and 26.3 cm found in summer and winter, respectively. However, other studies have demonstrated the higher potential of GG-R for precision altimetry over young sea ice

[105]. These studies showed that seasonal changes (from areas of lower to higher ice concentration) resulted in improvement of 6 cm RMSE and 21 cm standard deviation median differences between the reference surface model and the GG-R altimetry [76].

Figure 4.20 shows four collocated GG-R profiles generated by different references and collocated FMs, with three of these profiles located in the Arctic region (first three columns), and the last example close to the vicinity of the coast of Antarctica. The physical distances between the collocated events range from 0.87 to 4.38 km (Figure 4.20b). In the left panel, FM122 serves as the reference track and FM120 as the collocated track, both tracking SVN04 on October 30, 2020. The first measurements of the reference and collocated tracks were captured at 10:33:23 UTC and 10:33:40 UTC, respectively. The physical distance between the reference and the collocated tracks varies from 3.5 km to 4.4 km (second panel). Figures 4.20c and d show retrieved GG-R heights and SLA from the reference (blue dot) and collocated (red dot) FMs. The reference surface models for the reference (blue line) and collocated (red line) tracks are also presented in Figures 4.20c. A good agreement between the RA height and each respective reference surface can be seen, resulting in SLA values below 15 cm.

Generally, the height profiles from the reference and collocated FMs over polar regions show residuals with respect to the reference model with an RMSE of better than 9.4 cm (Table 4.17). Additionally, the RMSE between the $SLA_{GG\text{-}R}$ from the reference and collocated tracks are better that 9.2 cm. The cm-level agreement between the sea surface height with respect to the reference models and $SLA_{GG\text{-}R}$ highlight the strength of the GG-R methodology and the consistency of results between GG-R measurements. The remaining difference may be due to the presence of ice, which is not considered in the reference surface model. As the MSS is the multi-year average of the sea surface, it does not include contributions from impacts such as the presence of ice, winds and eddies.

Moreover, each GG-R collocated event is independently compared to the CMEMS SLA values, demonstrating a median RMSE and standard deviation of 11 cm and 8.4 cm, respectively, thereby confirming the consistency of $SLA_{GG\text{-}R}$ retrievals.

Table 4.17: Comparison of four GG-R collocated events from Figure 4.20

	FM122/FM120	**FM106/FM113**	**FM106/FM113**	**FM120/FM122**
GPS PRN	04	30	30	05
Date	2020/10/30	2020/11/29	2020/11/29	2021/03/05
Reference FM time	10:33:23	23:41:02	23:46:42	11:18:45
Collocated FM time	10:33:40	23:41:08	23:46:48	11:19:14
Height RMSE (cm)	7.4	8.7	9.1	9.4
$SLA_{GG\text{-}R_{ref.}}$ RMSE (cm)	6.7	9.6	9.4	4.2
$SLA_{GG\text{-}R_{col.}}$ RMSE (cm)	6.1	9.2	9.4	4.0
$SLA_{GG\text{-}R_{ref.\ vs.\ col.}}$ RMSE (cm)	7.3	8.6	9.2	4.6

GG-R signal satellite altimetry coverage and coherency

In this section, we showcase a study illustrating the coverage of Spire GG-R in comparison to satellite altimeters, as well as the global coherency distribution of GG-R measurements. To achieve this, we processed data from May 2019 to June 2020 for the GG-R signal coverage and the coherency distribution analysis. Additionally, a week in June 2020 is analyzed to compare the coverage of GG-R and RA measurements.

Coverage The number of GG-R observations found from the first week of June 2020 is depicted in a 9-km EASE Cylindrical grid (Figure 4.21). Due to the orbit of the Spire constellation, most of the reflections are concentrated in polar regions. It is worth mentioning that while the radar altimetry spatiotemporal resolution remains constant, GG-R observations are pseudo-random data. In other words, satellite altimetry data is consistently valid worldwide at specific revisit times [99], whereas GG-R observations depend on probability of detecting a coherent reflection at any given time.

Out goal is to assess the coverage complementarity between Spire GG-R measurements and current altimetry data measurements. To achieve this, a week of Spire Level 2 (L2) data (profiles that passed the quality control filters of coherence and continuity criteria [77]) was selected, prior to the global data filtering, and all available measurements for the four satellite missions selected in this study (Sentinel-3A/3B, Saral, and Cryosat-2) collected during the first week of June 2020. Figure 4.22 presents Spire data in green and the radar altimetry data in red. This figure represents the grid cell (9 km EASE) that contains the highest number of valid measurements, whether from GG-R or RA. This data is depicted

across three different grids (worldwide cylindrical (Figure 4.22a), north (Figure 4.22b), south (Figure 4.22c)). GG-R observations are prevalent mostly in the area above latitudes of 50°N where the sea-ice can be found, with fewer measurements in the vicinity of the coast of Antarctica. In the Ross Ice Shelf in the East of Antarctica, there are less measurements. GG-R measurements are available in the Indonesian seas, Baltic and Mediterranean seas and Gulf of Mexico. The advantage of using GG-R measurements in polar regions is obvious as the number of measurements is higher. Furthermore, radar altimetry orbits do not cover latitudes above/below 88°N/S, making data in this areas particularly valuable. It is also worth to mention that the measurement rate is 50 Hz for Spire GG-R and 1 Hz for the satellite altimeters, contributing to the higher number of observations per grid cell.

Coherency As mentioned in Section 3.3 the coherency is computed using a 2-second moving window to calculate the standard deviations of the phase derivatives applied to the unwrapped phase residual differences of L_1 and L_2 from the reflected signal, corrected for cycle-slips. To establish a coherent segment, a minimum of 3 seconds of continuous measurements must exceed an empirically determined threshold of 0.065.

The data is gridded in three types: EASE Cylindrical, north and south projections. Three projections are shown in this study due to visual limitations of the cylindrical projection over the polar regions. Figure 4.23 shows the distribution of coherency in Spire GG-R measurements from May 2019 to June 2020, predating the application of the Spire data equatorial filter. The presented percentage values are relative to the highest coherency found in a grid cell. Additionally, the regions of interest like Gulf of Mexico, area on Indonesian SEAS, and Hudson Bay are also illustrated in Figure 4.23 due to the presence of coherent GG-R signals.

The highest percentage of coherence is observed in regions where the measurements are more prevalent (Figure 4.21). It coinciding with sea ice areas such as North and South Poles, as well as regions like Hudson Bay and Sea of Okhotsk in the northwestern of the Pacific Ocean. Additionally, high coherence is observed in areas with calm waters, like the Gulf of Mexico and the Indonesian archipelago, when compared globally. Notably, coherency levels exceeding 40% are found in the area of North Pole, correlating with presence of new-

year ice. Regions where first-year ice is formed include Hudson Bay, the western waters of Greenland, the East Siberian Sea in the northeast of Russia, and the North of Okhotsk Sea [106]. Focusing on regions with larger coherence in the northern hemisphere, variations in coherence levels can be observed across the expanse of sea ice. Examinations of various datasets such as ice concentration reveal a relationship between regions of higher coherence (around 40% and above) and the presence of young ice during periods of largest ice concentration and sea ice coverage [106, 105]. By comparing the median coherence percentages using two identical grids for both products, it is determined that there is an average 32 times more coherence between zero and first-year ice compared to first and second-year ice.

Global and regional track-wise coherency comparisons show that about 24% of tracks are coherent. A similar number is reported in [104], where reflections of GPS and Galileo collected in NASA Cyclone GNSS mission were studied, revealing 12 coherent tracks out of 63 (20%). Zooming into the regional number of profiles, the largest coherency value is found in the area of Hudson Bay, including some of the water bodies north of Hudson Bay, where 86% of the tracks in the region were found to be coherent. The second region with higher coherency corresponds to 52%, which includes the area of Arctic (north of 50°N), excluding the area of Hudson Bay. The third in the crescent order is the area of Java Sea with 35%. This is followed by the South Pole area (latitudes south of 50°S) with 31%, and Gulf of Mexico area with 29%. Finally, the area between 50°N and 50°S exhibits 7.4% coherency, excluding the Gulf of Mexico and Java Sea area.

4.5.3 Discussion and Interpretation

The comparison results highlight a difference ranging from decimeter to centimeter level between the retrievals from GG-R and those from radar altimetry missions, respectively. This difference becomes particularly evident when comparing with the SLA_{CMEMS} (Table 4.15). Despite using the entire available dataset, the number of observations compared remains relatively limited. This limitation arises due to a recurring phenomenon observed in the majority of analyzed profiles: while there are coherent GG-R retrievals, there are no valid

altimetry data for the radar altimeters measurements, and vice versa. Although the number of collocated tracks is substantial, the number of altimetry sampling comparisons is notably low, as illustrated in Table 4.15.

Two plausible and complementary hypotheses may explain these observed phenomena, both linked to the surface characteristics at the reflection point. First, the geometries of the reflections may be complementary. Reflections collected at low elevation angles often show high coherence over smooth surfaces such as ice, sea-ice, and calm waters. However, signals over such large, smooth surfaces might introduce noise in satellite altimetry receivers due to radar echo contamination from the very strong signal reflected from calm water [107]. Second, the altimetry product itself might feature an ice flag in areas with a high probability of ice presence, consistently aligning with high coherency Spire observations. To further illustrate this discussion, we present two examples showcasing this particular phenomenon (Figures 4.24 and Table 4.18), that offer insights into the interplay between Spire GG-R and satellite altimetric data. It reveals how they complement each other in various scenarios. This analysis illuminates both the strengths and limitations inherent in each measurement approach.

Table 4.18: Comparison of complementary tracks from Figure 4.24

	Sentinel-3A	**Cryosat-2**
Spire FM	106	103
GPS PRN	05	06
Date and time (GG-R)	2021/01/03 02:59:22	2020/04/12 02:27:44
Date and time (RA)	2021/01/03 09:17:26	2020/04/11 03:55:11
Height RMSE (cm)	36.09 cm	-
$SLA_{GG\text{-}R}$ RMSE (cm)	8.65 cm	11.95 cm
SLA_{RA} RMSE (cm)	5.38 cm	10.88 cm
$SLA_{GG\text{-}R\ vs.\ RA}$ RMSE (cm)	15.43 cm	-
$SLA_{GG\text{-}R\ vs.\ CMEMS}$ RMSE (cm)	12.3 cm	11.8 cm
$SLA_{RA\ vs.\ CMEMS}$ RMSE (cm)	5.2 cm	2.5 cm

The results from Section 4.5.2 demonstrate internal consistency within the current model formulation, suggesting that the developed technique and models are operating effectively.

Additionally, Section 4.5.2 reveals regions where GG-R shows greater potential in terms of data coherency distribution and the number of observations compared to the radar altimetry missions used in this study. Areas with higher coherency and a larger number of observations compared to other satellite missions include the north and south Pole regions, excluding coastal land measurements, Hudson and James Bay, the Indonesian archipelago, the Baltic sea, and the north of the Sea of Okhotsk (east of Russia and North of Japan).

Upon exploring GG-R and radar altimetry comparisons, it becomes apparent that GG-R coherent data complements radar altimetry measurements, with potential applications mainly in polar regions and areas with high ice concentration such as Hudson Bay and the Sea of Okhotsk, or calm waters like the Indonesian archipelago.

4.5.4 Summary

This study explores the potential of GG-R as a supplementary system to radar altimetry data. It compares SLA measurements from radar altimeters (Sentinel-3A and 3B, Saral, and Cryosat-2) with collocated measurements derived from Spire Global Inc. Grazing Angle GNSS-R satellite constellation. The data are 1-day and 10 km apart using exclusively dual-frequency GPS measurements. The analysis reveals that height measurements from both techniques often complement each other: with Spire valid altimetry data present when RA data are not valid and vise-versa. This result is obtained for a limited sampling comparisons despite a substantial number of collocated tracks. Plausible hypotheses linking this phenomenon to surface characteristics at the reflection point suggest complementary signal reflection geometries and features in the altimetry product itself. However, out of nearly 10,000 samples, the SLA comparison revealed a disparity of approximately 47 cm. This discrepancy is further evident in the comparison of SLA_{CMEMS} measurements, highlighting a centimeter to decimeter-level difference between radar altimetry and GG-R. This underscores the need for improved accuracy in GG-R measurements to establish it as a complementary system to current satellite altimeter data. Enhancements that could improve GG-R performance include: better coherency and cycle slips detection, incorporating L_5 carrier frequency along with Galileo signals, more accurate estimation of tropospheric de-

lay particularly at low elevation angles, refined location of the SP, and implementing lead detection to differentiate between sea ice and water signals.

Comparing GG-R collocated events verifies that there are no systematic errors in the system, with an RMSE of SLA of 25 cm. Additionally, two more analyses are conducted on coverage and coherency distribution. These analysis demonstrate higher coherency in polar regions, including Hudson and James Bay and the Okhotsk Sea, as well as in calmer waters, such as Gulf of Mexico and Indonesian seas. These areas are most conducive to the true potential of GG-R measurements, especially north/south of 88° N/S where satellite altimetry data is unavailable. Furthermore, in the north pole region, higher coherency is found in areas where first-year ice is present.

In conclusion, this study demonstrates the supplementary role of GG-R in satellite altimetry, providing valuable insights into regions where traditional altimetry missions may encounter limitations. However, enhancing measurement precision is essential for improving the accuracy and reliability of GG-R altimetry data. For instance, refining tropospheric model estimations, particularly for low elevation angle tracks, and developing new methods for phase unwrapping and cycle slip detection and correction, such as computing the interference pattern from the I/Q values and implying Kalman filtering methods, would be beneficial. Furthermore, advancing the GG-R technique to achieve absolute height retrievals, rather that relative ones, represents another promising avenue for improvement [108].These methods could serve as potential improvement and future directions of GG-R altimetry retrievals, ultimately contributing to the accuracy and understanding of altimetry measurements.

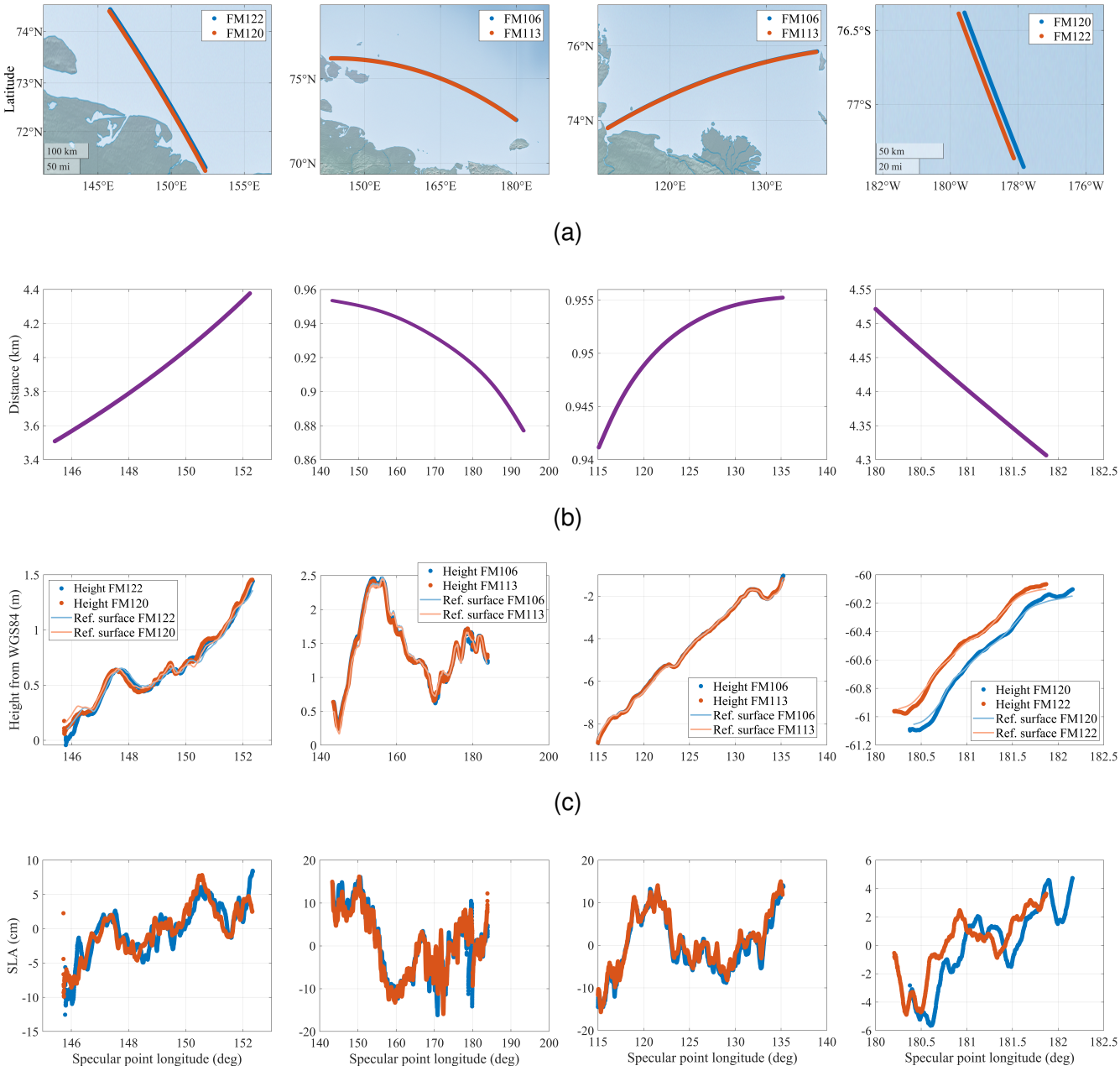

Figure 4.20: GG-R collocated events with the first three columns representing examples located in the Arctic region and the last column showing an example in Antarctica

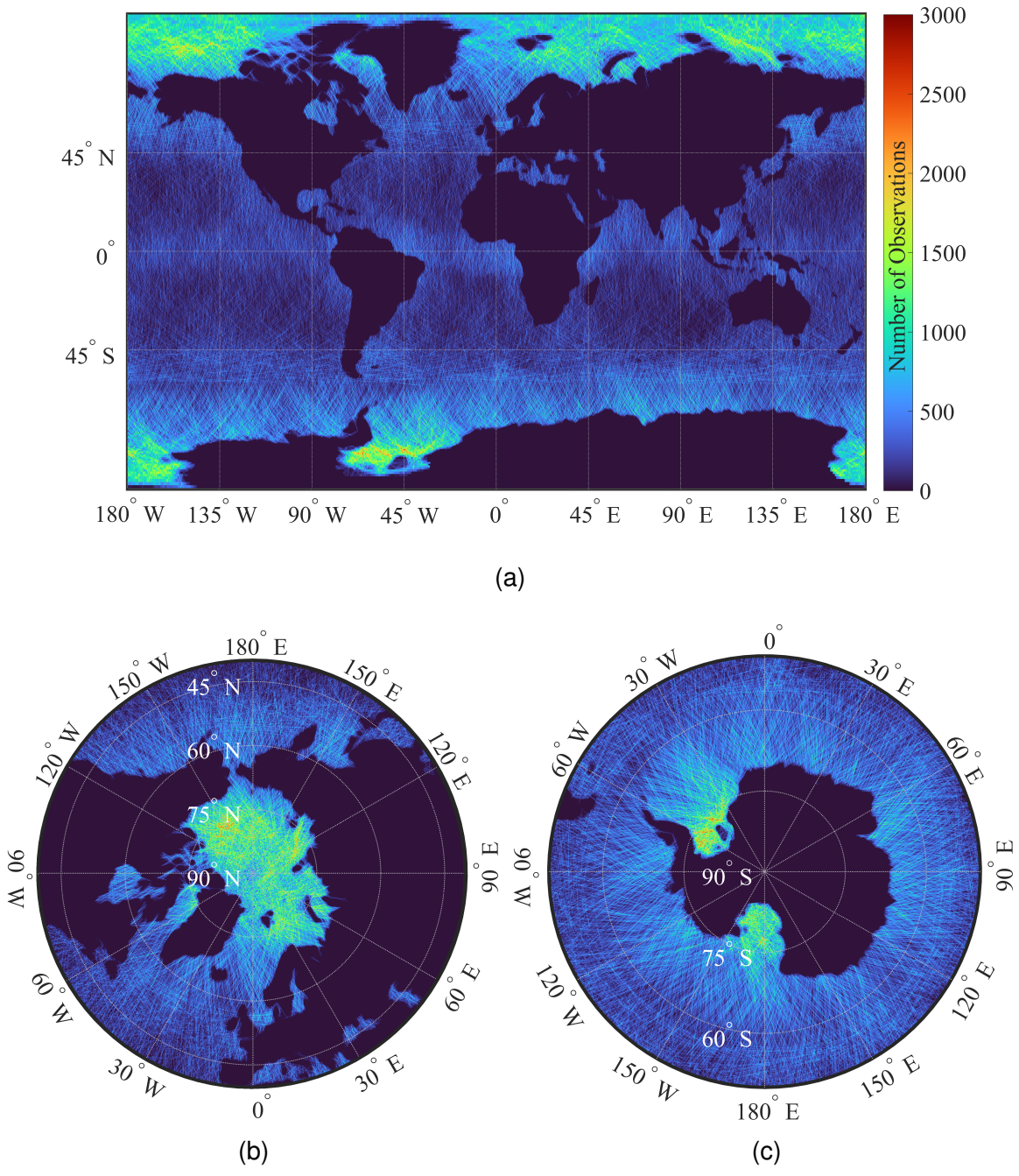

Figure 4.21: Number of Spire GG-R observations from May 2019 to June 2020 displayed in (a) EASE 9-km Cylindrical grid, (b) North EASE 9-km Grid Projection, and (c) South EASE 9-km Grid Projection

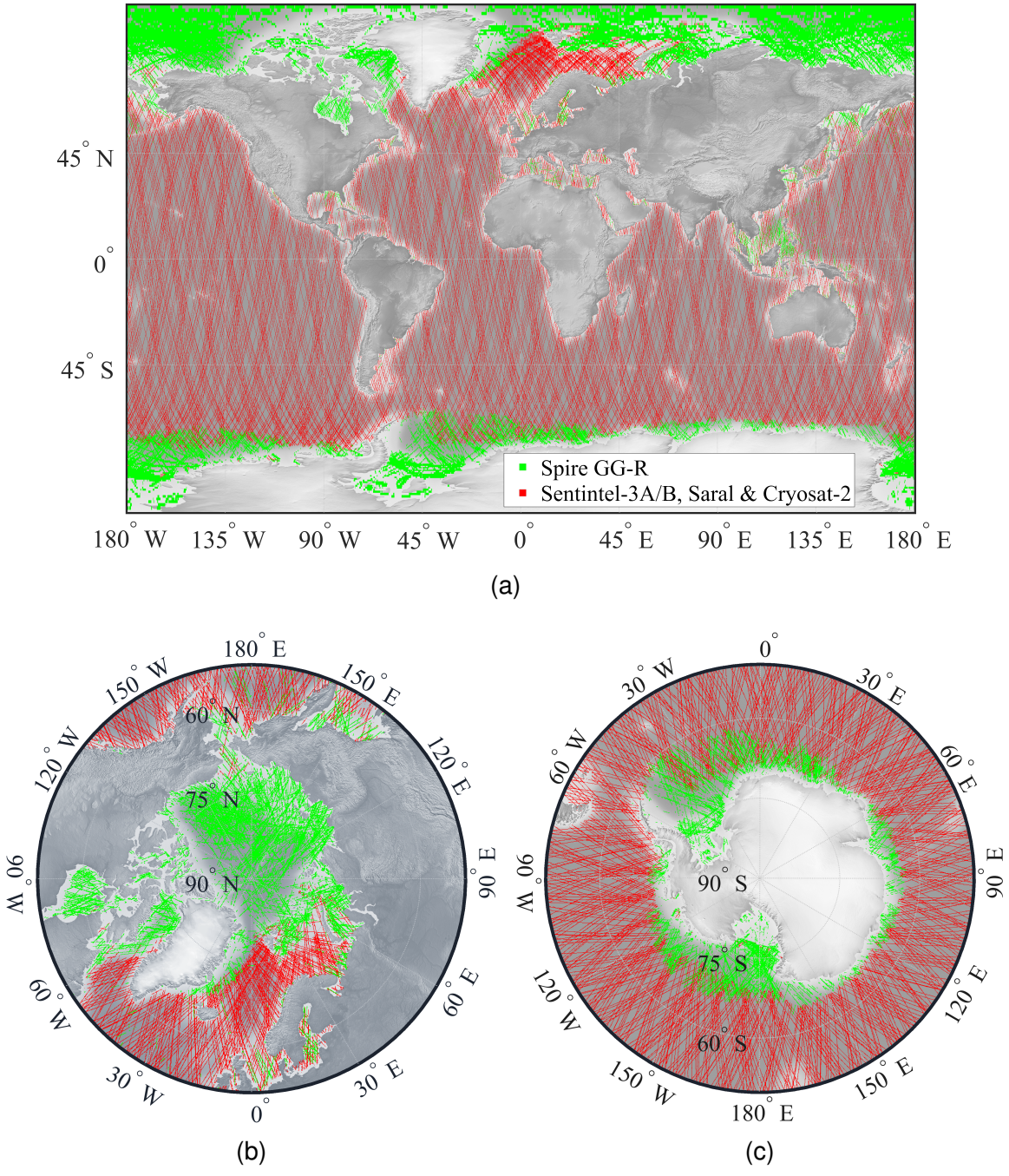

Figure 4.22: Grid of prevalence of measurements. Spire GG-R L2 measurements (green), RA (red) data from the first week of June 2020. (a) EASE 9-km Cylindrical grid, (b) North EASE 9-km Grid Projection, and (c) South EASE 9-km Grid Projection

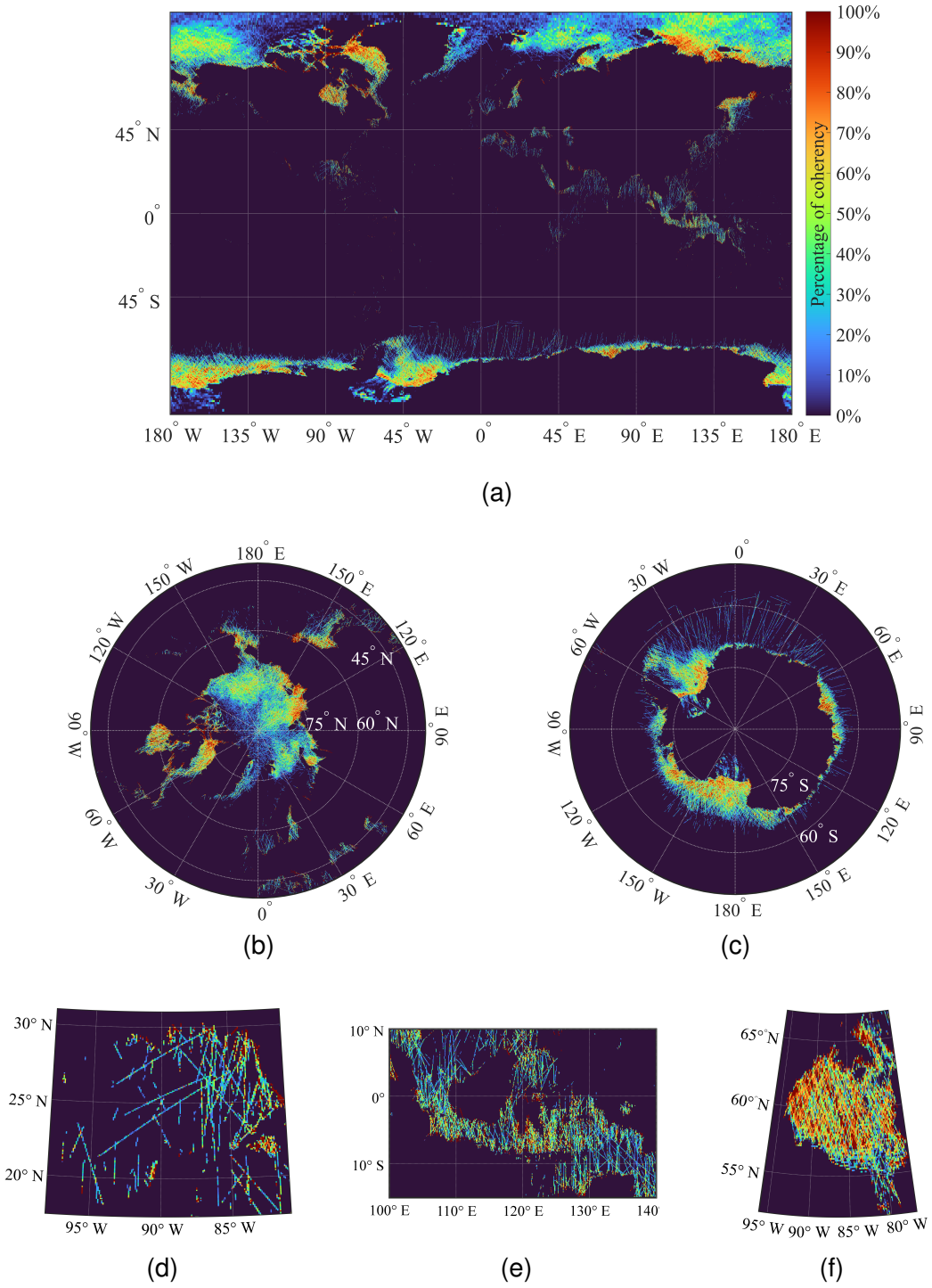

Figure 4.23: Percentage of coherency from May 2019 to June 2020 computed with an average moving window of the unwrapped and corrected for cycle-slips phase residual differences of L1 and L2 from the reflected signal. (a) EASE 9-km Cylindrical grid, (b) North EASE 9-km Grid Projection, and (c) South EASE 9-km Grid Projection and Zoom-in the regions of (d) Gulf of Mexico, (e) Indonesian SEAS, and (f) Hudson and James Bay area.

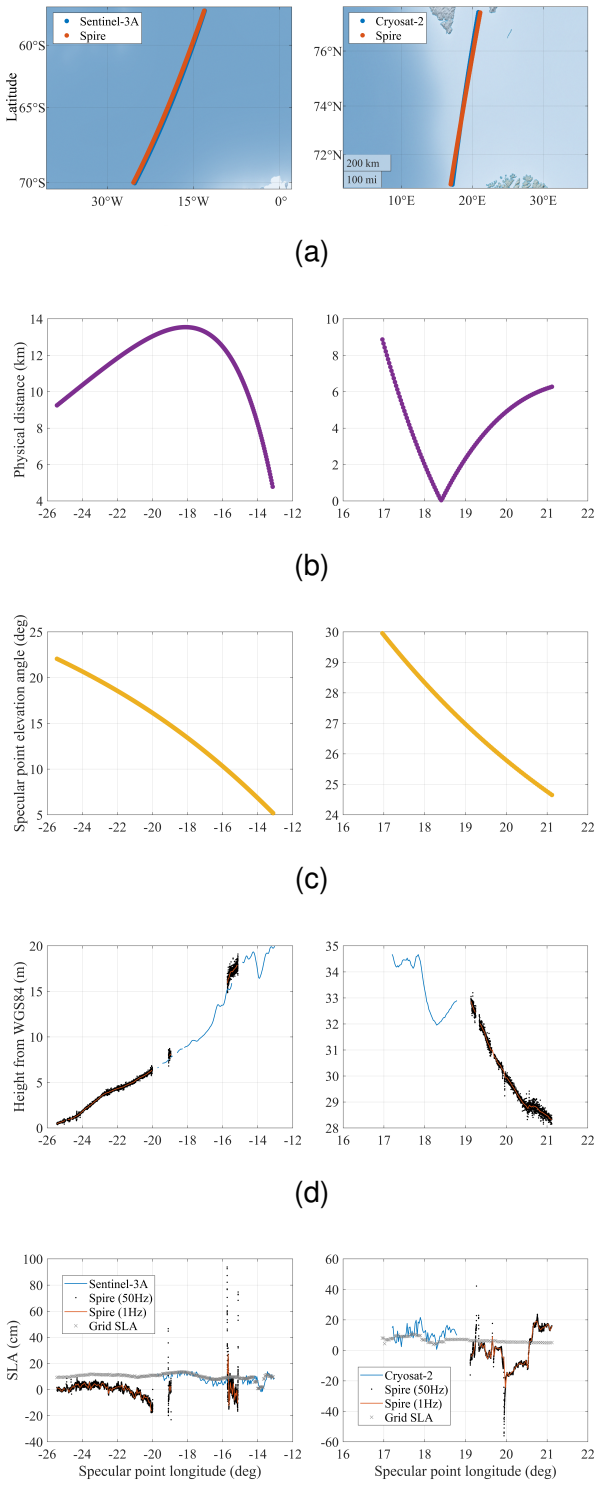

Figure 4.24: Examples of complementary tracks from Sentinel-3A and Cryosat-2: (a) Locations of Sentinel-3A/3B (blue) and Spire (red), (b) Physical distance in km, (c) SP elevation angle for Spire GG-R track, (d) Relative height w.r.t WGS84 for GG-R (50 Hz in black dots and 1 Hz in red line) and RA (blue line), and (e) SLA_{CMEMS} (grey crosses).

Chapter 5

Ice-sheet GG-R altimetry over Greenland and Antarctica

Ice sheet altimetry using group delay GNSS-R data was demonstrated in [109] [16] where UK-TDS-1 measurements were shown to yield surface height precision on the order of 30 meters. In contrast, more sophisticated satellite missions such as ICESat-2 and CryoSat-2 use laser and radar altimeters to measure the thickness and elevation of polar ice sheets with centimeter-level precision. Over the flat interior of the ice sheets, ICESat-2 measures surface elevation with an accuracy and precision of 3 cm and 9 cm respectively compared to in-situ GNSS measurements [110]. More extensive comparisons of CryoSat-2 performance against coincident airborne laser data from Operation IceBridge [111, 112] have shown that CryoSat-2 measures ice sheet surface elevation with an accuracy better than 30 cm in the interior of the ice sheets. The performance of the two altimeters slightly degrades over the high slope margins of the ice sheets, where the combined effect of the complex topography and rapidly thinning outlet glaciers leads to greater uncertainties in the retrievals of surface heights from spaceborne altimeters. However, both missions have demonstrated the ability to measure elevation changes at fine temporal and spatial resolution - typically every month at 5km - with a high accuracy of 1 cm/yr for CryoSat-2 [113] and 0.4 cm/yr for ICESat-2 [114] at the scale of the ice sheets, thanks to the large number of independent measure-

ments they acquire across the ice sheets. Importantly, ICESat-2 and CryoSat-2 are already operating past their designed lifetime and do not cover a gap above 88°S over the Antarctic Ice Sheet [115]. In this study, we seek to apply the decimeter-level phase-delay capability using GNSS-R signals on sea ice surfaces to ice sheet surfaces as a complementary system to the existent satellite altimetric products.

As such, this chapter a study of ice sheet height in Antarctica and Greenland GG-R land retrievals. Section 5.1 of this chapter introduces the Spire constellation and GG-R observations, which span a nine-month period from January to October 2021 and cover the Greenland and Antarctic ice sheets. The resulting ice sheet heights are assessed in Section 5.2. In Section 5.6, we discuss the potential of GNSS-R measurements and their complementary to altimetry measurements. Finally, Section 5.7 contains a summary of the results obtained in this chapter.

5.1 Data and Models

The L1B data span from January to October 2021 in Greenland and Antarctica and, the reflections are collected from 17 Spire CubeSats. In particular, the FM numbers 79, 87, 88, 99, 100, 101, 102, 103, 104, 106, 113, 116, 118, 120, 122, 124 and 125, in which we can find the orbital information in the Table 3.1.

From all the retrievals collected there were some coastal reflections, which have been filtered by a 200-km coastal buffer using a low-resolution line with the purpose to exclude sea surface reflections and to strictly keep land reflections [116].

The tropospheric model used in the data processing in this case study is the the VMF3, that together with the GPT3 is used to estimate the tropospheric delay [61]. Furthermore, surface height reference model above the ellipsoid is determined by extracting surface elevations from DEMs. Specifically, the ArcticDEM [72] and the REMA v1.1 [73] are used as DEMs in Greenland and Antarctica, respectively. These DEMs serve as the reference surfaces, with a horizontal resolution of less than 10 m [117, 118]. The method used for reference elevation model values involves taking the nearest DEM point location for each SP.

This rigorous approach ensures that the surface height deviations are precisely centered at zero.

5.2 GG-R Ice Sheet Height Retrievals

Ice sheet surface heights are retrieved from Spire grazing angle GNSS-R measurements from January to October 2021. A total of 25,186 tracks (L1B) were identified in Greenland and Antarctica during this nine-month period (Figure 5.1). Table 5.1 summarizes the number of profiles that passed the QC filter (L2), the total number of tracks that meet the low-resolution land filter (L2-LR) and the total number of coherent segments. In the remainder of the paper, the surface height deviations are presented for both regions. Additionally, two collocated height profiles in Antarctica are discussed in this section to assess the repeatability of the height retrievals.

Table 5.1: Number of L1B, L2, L2-LR profiles and total number of segments in Greenland and Antarctica from January to October 2021

	L1B Profiles	L2 Profiles	L2-LR Profiles	Coherent Segments
Greenland	3,165	335	136	433
Antartica	22,021	1,889	1,673	7,366

5.3 Height Retrieval over Greenland

A total of 3,165 grazing angle GNSS-R events were collected over a nine-month period from January to October 2021 in Greenland, and 11% of the profiles passed the QC filters. It is worth noting that while coastal segments are also processed, coherent segments less than a 200-km buffer from the Greenland's perimeter are discarded, as mentioned earlier. As a result, only 136 coherent profiles over the ice sheet are retained, with a total of 433 coherent segments. Figure 5.1 illustrates the profiles generated over Greenland ice sheet using Spire GG-R measurements from January to October 2021. The profiles are color-coded and coherent segments used in this study are outlined in purple.

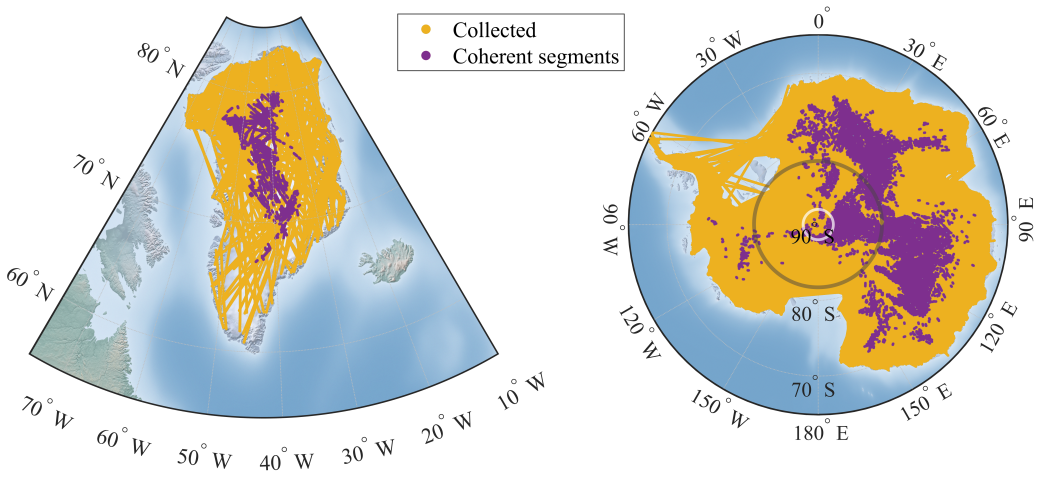

Figure 5.1: Spire L1B tracks generated from January to October 2021 are shown in yellow, while the L2-LR tracks used for ice sheet retrieval are shown in purple over Greenland (left) and Antarctica (right). The white line in the center of Antarctica delineates the 88° boundary where satellite altimeters, such as CryoSat-2 or IceSat-2, do not provide coverage. The dark line delineates the 81.5 ° boundary where satellite radar altimeters such as ERS-1/2, ENVISAT, and Sentinel-3 do not provide coverage.

As absolute height measurements are not resolved, careful selection of the reference surface model is crucial for outputting the relative height profiles as outlined in Section 3.6. In Greenland, the mosaic ArcticDEM [72] with a 100-m spatial resolution in 32-bit GeoTIFF format is used as the reference model.

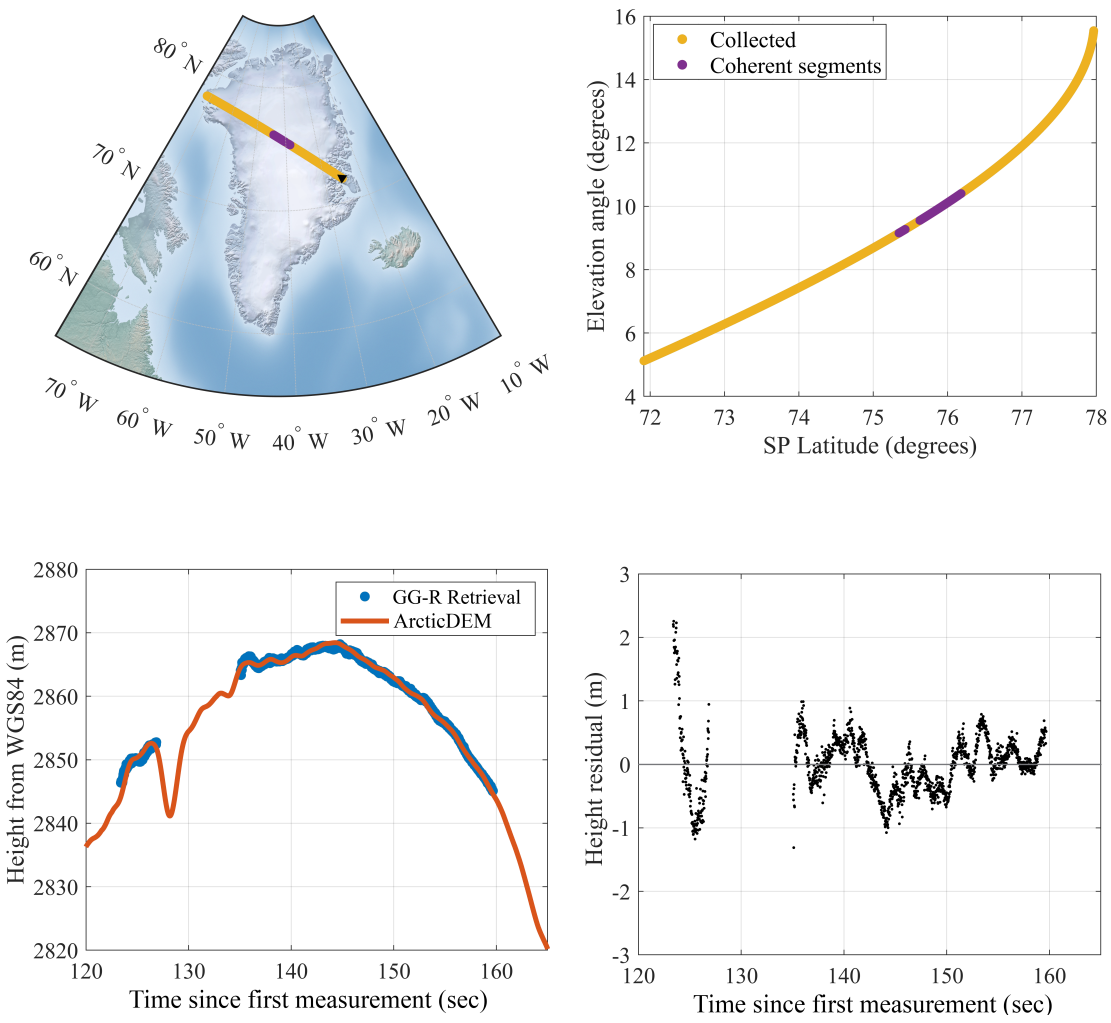

Figure 5.2: GG-R event over Greenland on 26 September 2021 at 13:41:33 UTC. (a) Collected phase observations (yellow) and coherent segments that are successfully unwrapped (purple). The black triangle indicates the first measurement location; (b) SP elevation during the GG-R event; (c) GG-R height profile (blue) since the first measurement, using the ArcticDEM as the reference model (red); (d) Residual of the GG-R height profile relative to the ArcticDEM

To illustrate, a GG-R profile from the FM104 is presented in Figure 5.2. This profile was generated from the GNSS transmitter SVN 62 on September 26, 2021, at 13:41:33 UTC. The measurements were collected at approximately 25° north and 72° west, as shown in

Figure 5.2a. Two coherent segments were found 124-sec after the first measurement, with durations of 3.5-sec and 24.6-sec, respectively. The RMSE between the GG-R surface height retrieval and ArcticDEM is 47.70 cm.

Figure 5.3 shows the distribution of segment-wise RMSE for the ice sheet height GG-R retrievals and the ArcticDEM reference surface model in Greenland over a nine-month period. The results indicate a considerable level of accuracy in the GG-R retrievals, with a median RMSE of 1.62 m for the coherent segments. Moreover, 85% of coherent segments have an RMSE below 3 m. It is important to note that the presence of small proportion of segments with higher RMSE values might be attributed to errors in the reference model or inconsistencies in the ice sheet surface, such as areas with relatively high slope values. Nevertheless, these results demonstrate the potential of the GG-R for retrieving ice sheet height over large spatial scales and highlight its relevance for a continuous monitoring of the polar ice sheets.

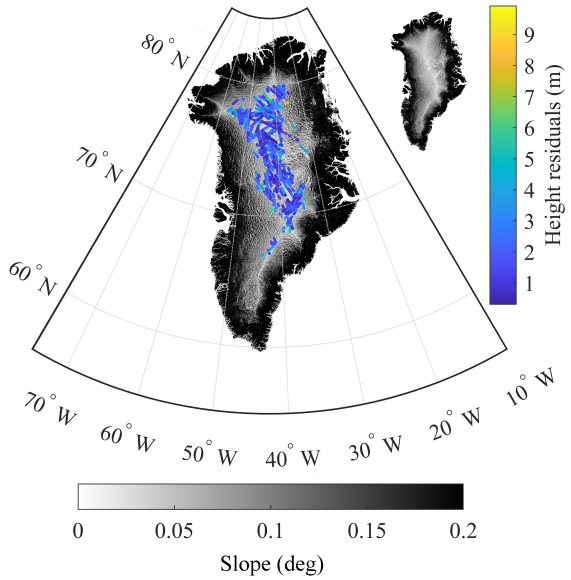

Figure 5.3: Coherent segments color-coded based on the RMSE between the GG-R height retrievals and ArcticDEM as the reference model in Greenland, along with an overlay of the surface slope [116]. The inset provides a better illustration of the correlation between the GG-R tracks and surface slopes.

5.4 Height Retrieval over Antarctica

This section provides details on the results of height retrieval over Antarctica. A total of 22,021 profiles were generated between January and October 2021 (Figure 5.1). However, only 1,889 profiles passed the QC filters of coherence and continuity criteria, and were deemed acceptable for further analysis. To ensure the reliability of results, all profiles within a 200-km buffer from Antarctica's coastline are discarded. Consequently, 1,673 profiles are used to retrieve the grazing angle ice sheet height over Antarctica (Figure 5.1).

As a matter of fact, satellite altimeters including CryoSat-2 and Sentinel-3 have limitations when it comes to measuring regions above certain latitude. Specifically, areas above 88° and 81.5° South latitudes are not accessible to these satellites, as depicted by the white and grey circle lines in Figure 5.1). Consequently, the data collected within these areas possesses exceptional values, considering the restricted measurement capabilities in those regions. Moreover, the upcoming CRISTAL satellite mission, expected to operate similarly to CryoSat-2, is planned for launch in 2027. In the scenario where CryoSat-2 becomes inoperative before the launch of CRISTAL, Sentinel 3 might remain operational but will still be unable to provide coverage for latitudes above 81.5°S.

Figure 5.4 shows an example of a GG-R profile over Antarctica, which was generated on 5 August 2021. The profile is from FM118 tracking the 50-Hz OL tracking of I and Q measurements of direct and reflected L_1 and L_2 signals from the GNSS transmitter SVN50. The first coherent observations occurred 129-sec after the first measurement at 23:55:21 UTC. The RMSE between the reference model and the height retrieval for all the 87.60-sec coherent segment is 93.01 cm. The RMSE of the last coherent segment that lasts 11.56-sec is 28.52 cm.

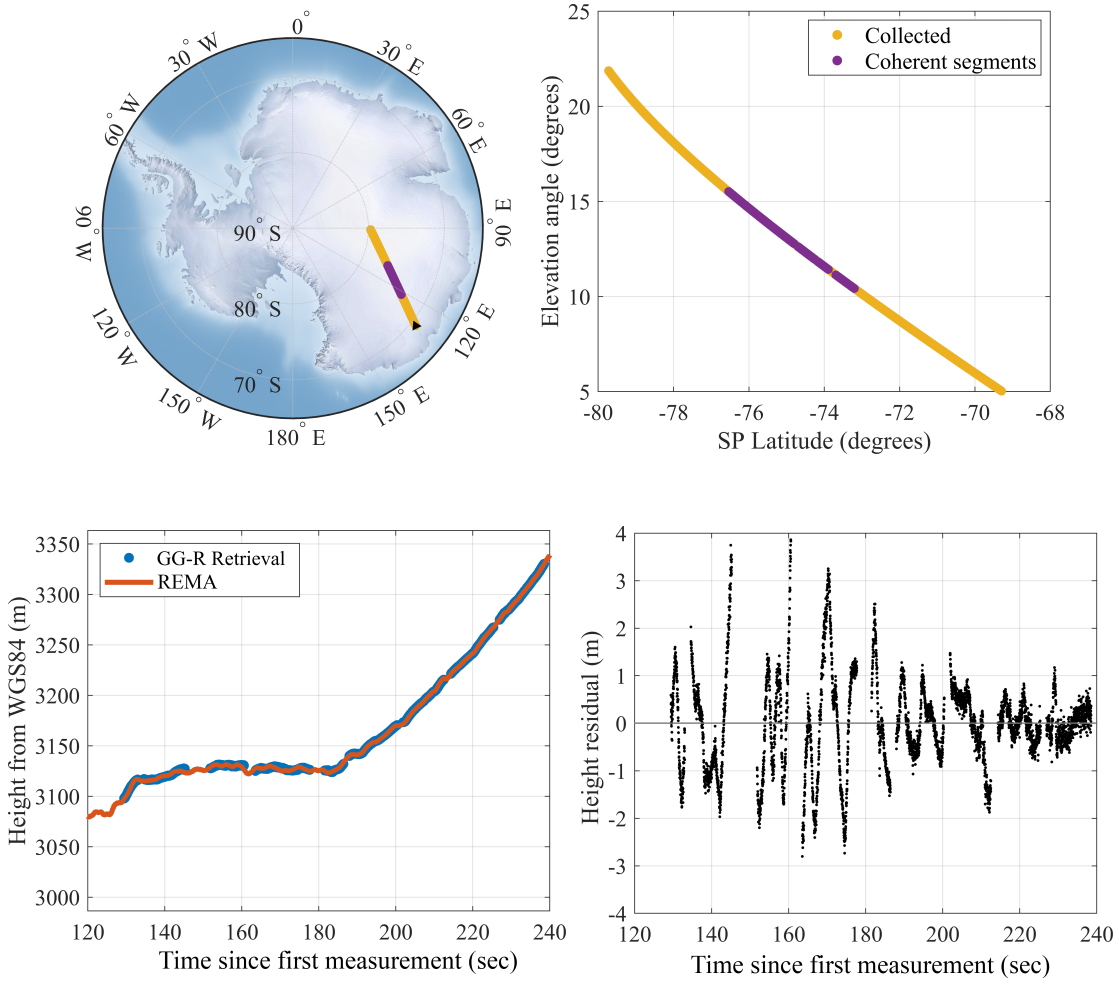

Figure 5.4: GG-R event over Antarctica on 5 August 2021 23:55:21 UTC. (a) Collected data (yellow), coherent segments (purple). The black triangle indicates the first measurement; (b) SP elevation during the GG-R event and (c); GG-R height profile (blue) since first measurement and the REMA as the reference model (red); and (d) residual of (c)

Figure 5.5 provides the Antarctic-wide assessment of RMSE between the GG-R surface height retrievals and REMA as the reference model. The median RMSE over all 7,366 coherent segments is found to be 1.78 m. The range of RMSE values varies from a minimum of 10.6 cm to a maximum of 19.25 m, indicating variability in the accuracy of height retrievals across different locations in Antarctica. However, the relatively low median RMSE obtained in this study suggests that GG-R can be a reliable technique for estimating ice sheet heights

over Antarctica, with potential applications for glaciological studies.

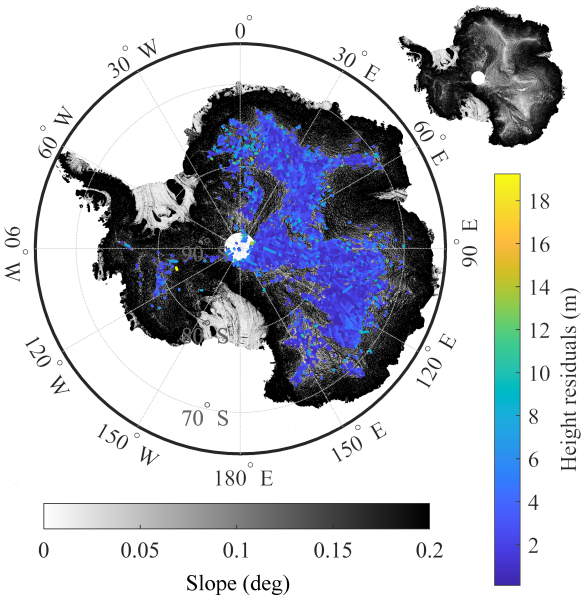

Figure 5.5: Coherent segments color-coded by the RMSE between the height retrievals and the reference model (REMAv1.1 at 200-meter spatial resolution) for the period of January to October 2021 over Antarctica, with an overlay of the surface slope. The inset displays the depiction of Antarctic surface slopes [116].

5.5 Collocated Height Profiles

This section presents two pairs of collocated profiles in Antarctica, which were generated by different FMs capturing the reflected signal from the same area within a short amount of time. The purpose of analyzing collocated height profiles is to understand the repeatability and consistency of height retrievals, which helps quantify the noise of the measurement system and isolate the magnitude of the different error sources.

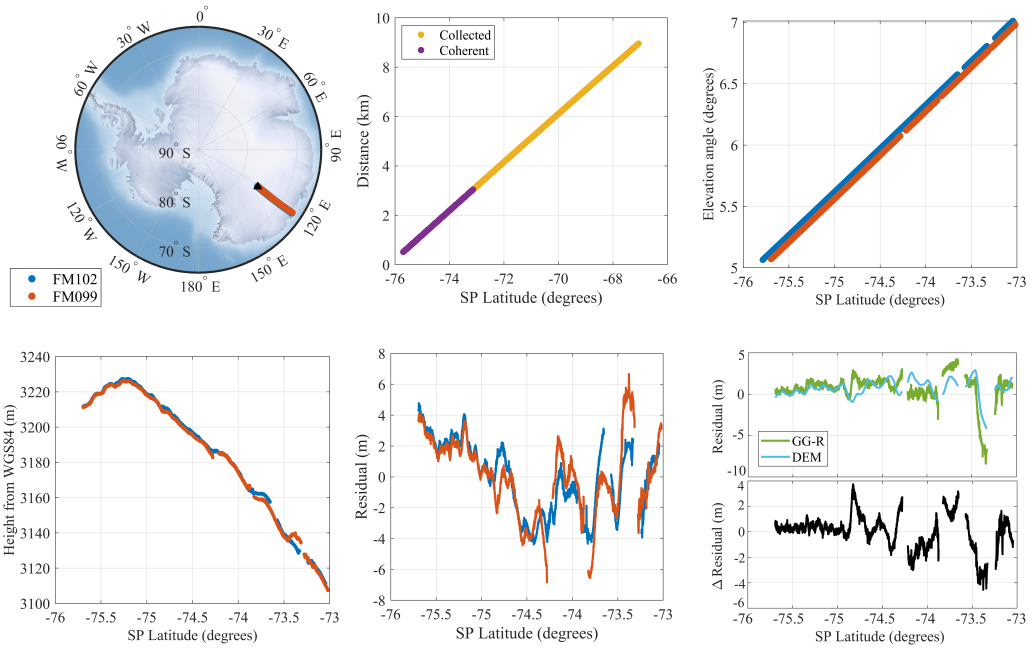

Figure 5.6: Collocated GG-R profiles generated by FM102 as the reference track and FM099 as the collocated track on August 21, 2021; (b) Physical distance between the reference and collocated tracks; (c) SP elevation during the collocated GG-R events; (d) GG-R collocated height profiles of the FM102 (blue) and FM099 (red); (e) residual of (d); (f) The green color in the top panel depicts the residual of (d) and blue color shows the residual of REMA at FM102 and FM099. Residuals of the top panel (bottom panel)

Figure 5.6 shows the collocated GG-R tracks generated by two different FMs (FM102 as the reference track and FM099 as the collocated track) tracking SVN71 on August 21, 2021. The first measurements of the reference and collocated tracks were captured at 13:37:04 UTC and 13:37:15 UTC, respectively. The physical distance between the reference and the collocated tracks varies from 500 m to 9 km, while the elevation angle of the coherent segments increases from 5° to 7° (Figure 5.6c). The RMSE between each GG-R profile and REMA is 1.85 m and 1.29 m for the reference and collocated tracks, respectively (Figure 5.6d). The sample-wise intersection height comparison is calculated using the coherent segments.

Figure 5.6e shows good agreement between the height GG-R retrievals, with an RMSE

of 40 cm. However, the systematic behavior observed in the residuals of both FMs implies limitations in the reference model. This behavior is visible in the bottom panel of Figure 5.6f, where the RMSE difference between the GG-R residuals and the REMA residuals is 1.33 m.

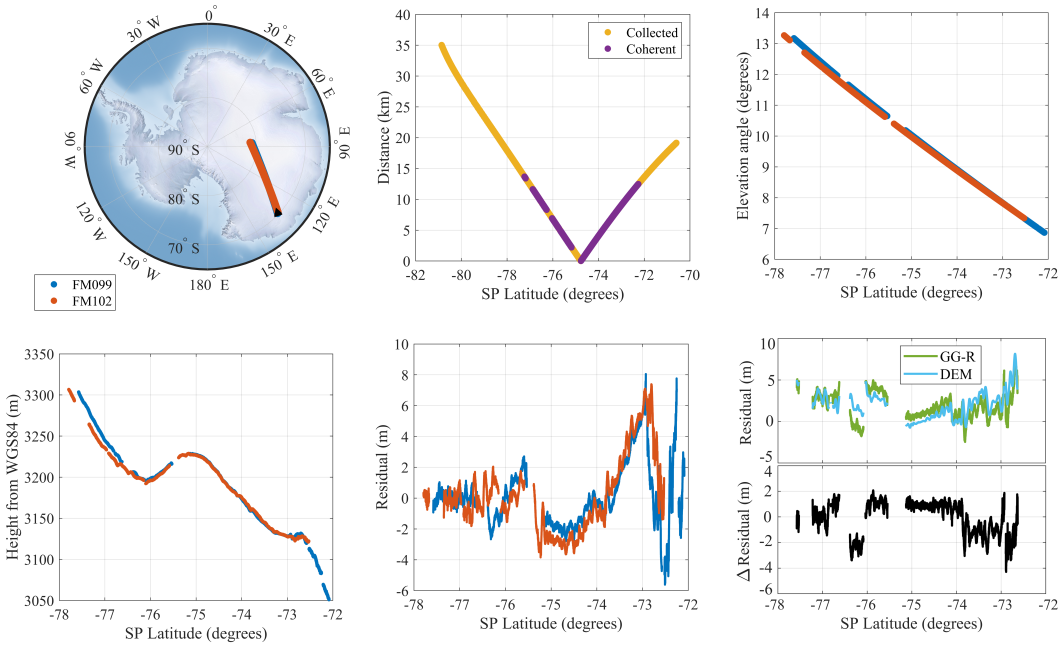

Figure 5.7: Collocated GG-R profiles generated by FM099 on April 30, 2021 as the reference track and FM102 on September 01, 2021 as the collocated track. The panels and colors are similar to those of Figure 5.6.

In Figure 5.7, another pair of collocated profiles tracking the GNSS signals by FM099 and FM102 is shown. The FM099 serves as the reference track, generated on April 30, 2021, at 23:00:15 UTC tracking SVN64, while FM102 is the collocated track generated on September 01, 2021, at 23:11:45 UTC based on SVN57 phase observations. The profiles start at -70° latitude and are 20-km apart. They intersect at -75° latitude, after which the physical distance between the collocated profiles increases to 35 km (Figure 5.7b). The elevation angle of the coherent segments ranges from $\sim$ 7° to 13°.

While the RMSE between the coherent segments of the reference profile and REMA is 2.42 m, it is 2.51 m between those of the collocated track and REMA. The closer the

physical distance between the profiles (Figure 5.7b), the smaller the residual between the GG-R height retrievals (Figure 5.7e). The systematic behavior of the residuals between the GG-R height retrievals on the one hand (green line in the top panel of Figure 5.7f) and the DEM data on the other hand (blue line in the top panel of Figure 5.7f) is clear. The RMSE between the two DEM data for the reference and collocated tracks is 1.29 m (bottom panel of Figure 5.7f).

5.6 Discussion and Interpretation

This section provides a more in-depth analysis of ice sheet height retrievals based on GNSS-R over Greenland and Antarctica using the GG-R approach. The aim is to help better understand the GNSS-R carrier phase observations under grazing angle events.

Figure 5.8 displays the Cumulative Distribution Function (CDF) of RMSE between the GG-R height retrievals of all coherent segments and ArcticDEM and REMA as reference surface models in Greenland and Antarctica, respectively. The CDFs of RMSE for both Greenland and Antarctica are similar, indicating that GG-R provides a consistent performance over both ice sheets. In Greenland, $\sim$90% of the CDFs of RMSE are less than 4 m, while in Antarctica, 80% of the CDFs of RMSE are less than 4 m. The median RMSE between track-wise GG-R retrievals and reference surface models in Greenland and Antarctica are 2.11 m and 2.49 m, respectively. It should be noted that there are 1,537 more GG-R retrievals in Antarctica than in Greenland.

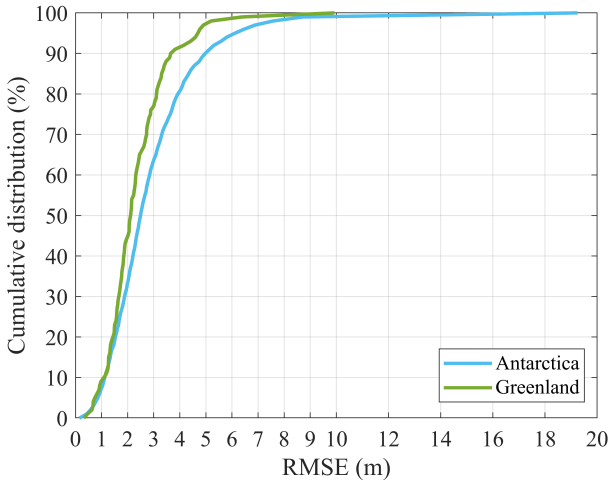

Figure 5.8: Cumulative distribution function of the track-wise RMSE in Antarctica (cyan) and Greenland (green)

Unlike conventional altimetry tracks, GG-R tracks are characterized by segmentation caused by rough surfaces and a loss of signal coherence. In our endeavor to understand the underlying cause of the distinct distribution of coherent measurements in both areas (Figure 5.1), we have identified a significant correlation with the topographical characteristics of the terrain. Specifically, coherent measurements are predominantly observed in areas with relatively low slopes (Figures 5.3 and 5.5), typically ranging from 0.01 to 0.1 degrees, indicating relatively flat terrain. To further investigate this correlation, we conducted an analysis of slope variations by computing the average slope across all segments within each region. The obtained values were approximately 0.05 degrees for Greenland and 0.06 degrees for Antarctica. These results provide partial evidence of a correlation between slope variations and the GG-R retrievals in each respective region.

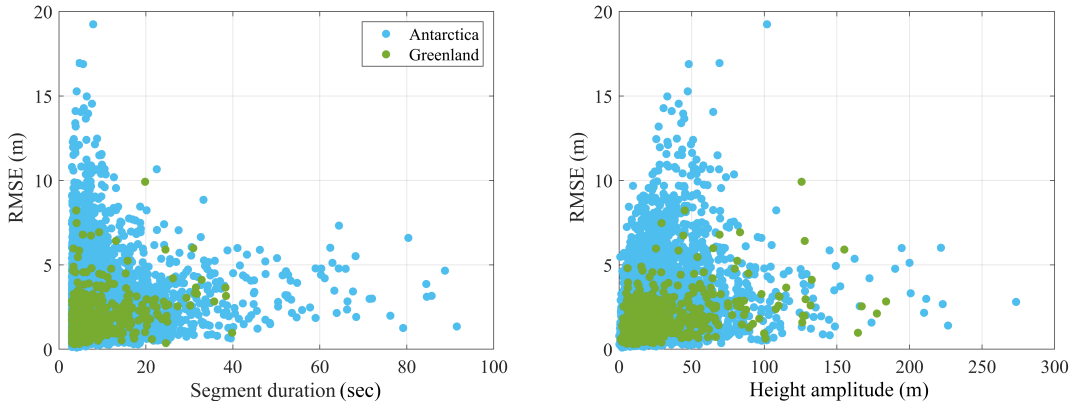

Figure 5.9: (a) Comparison of RMSE as retrieved for each individual segment over Greenland (green) and Antarctica (cyan); (b) GG-R residuals over retrieved height amplitude

In addition to the above analysis, we examine here the relationship between the effects of this segmentation and the performance metric defined (RMSE). To illustrate this issue, we have plotted the duration of the coherent segments (Figure 5.9) and the amplitude of the retrieved height, representing the absolute difference between maximum and minimum height values within each segment (Figure 5.9a). The segment-wise RMSEs between GG-R height retrievals and reference surface models in Greenland (green dot) and Antarctica (cyan dot) show a similar trend. The longer the segment duration is, the smaller the residuals between the GG-R height retrievals and reference surface model will be. Furthermore, the residuals between the retrieved ice sheet and ArcticDEM and REMA heights in Greenland and Antarctica are not a function of the height amplitude, as shown in Figure 5.9b. Therefore, GG-R products are not systematically affected by the elevation variations of ice sheet over the segment duration.

5.7 Summary

Grazing angle observations of GNSS reflections or GG-R are used to retrieve ice sheet height in Greenland and Antarctica in a systematic manner for the first time using Spire Global, Inc. data from 17 Spire CubeSats. While the number of tracks that passed the

QC measures was limited, the GG-R approach still provides a promising alternative to traditional satellite-based altimetry products. The ionosphere-free phase measurements from the direct and reflected signals are used to retrieve surface height over the polar regions. ArcticDEM and REMA are used here as reference surface models in Greenland and Antarctica, respectively.

The RMSE values of GG-R retrievals and their reference surface models are found to reach meter-level precision in both Greenland and Antarctica, indicating the potential of this approach to contribute to a more accurate estimation of ice sheet height. Moreover, our analysis showed that GG-R retrievals are not systematically biased by segment duration and surface elevation variations. These findings suggest that GG-R measurements can provide consistent and reliable ice sheet height retrievals, making it a valuable addition to the current satellite-based altimetry products. GG-R collocated events captured in Antarctica also highlight the limitations of reference surface models.

Coastal regions of Greenland and Antarctica are particularly interesting for ice sheet mass balance studies as ice losses are concentrated in the ice sheet margins [119] [120]. However, here, coastal areas are not well sampled by GNSS-R-based altimetry because of low signal coherence. The two main reasons for this low signal coherence are the relatively weak GNSS-R signals, which hinders increasing the sampling frequency size beyond 50 Hz, and complex underlying topography, which hinders unwrapping the phase information and disentangling cycle slips from true topographic signals. In future studies, collecting raw Intermediate Frequency (IF) signals in these coastal transition areas would enable studies with a higher number of delay taps (currently set to 3) and smaller chip spacing in order to better characterize the returned waveforms, and ultimately assess the feasibility of characterizing the heights of coastal areas, especially glaciers. Phase unwrapping approaches utilizing Kalman Filter approaches, which are able to account for the expected evolution of the height measurement based such as described in [121], could be pursued. Nevertheless, GNSS-R altimetry already provides reliable measurements in the interior of the ice sheets - and in Antarctica even provides additional coverage beyond current satellite radar and laser altimeters' polar gap - and thus future studies could investigate the potential of GNSS-R

measurements for measuring fluctuations in ice sheet elevation arising from surface mass balance processes.

Overall, the results reported here provide insight into the potential of dual-frequency GG-R measurements in complementing current satellite-based altimetry products over polar and ice-covered regions. Further research is needed to explore the full potential of this approach and to improve the accuracy of reference surface models for better estimation of ice sheet height.

Chapter 6

Software and L2 data product

The present chapter contains (1) the description of GRAALT software developed to process the data and produce the altimetry product in Section 6.1 and (2) a brief description of the final GL L2 data product from from Spire L1B product described in Section 6.2.

6.1 GRAALT description

GRAALT is the software used in this dissertation to process the L1B data to the L2. The purpose of this software is to facilitate its usage internally in the University of Luxembourg (UL), specifically in the department of GL. The graphical interface of GRAALTv1.0 software, shown in Figure 6.1, is designed to facilitate the processing and analysis of GG-R altimetry data. The interface is organized into several sections, providing the user with a structured and intuitive workflow:

Date Picker

Located in the upper left corner, this section allows the user to define the temporal range of the dataset to be processed. For the initial version of this software the data (L1B) is available from the 1st May 2019 to the 30th of October 2021. The Start Date and End Date fields include date and time selectors, ensuring precise control over the period of interest.

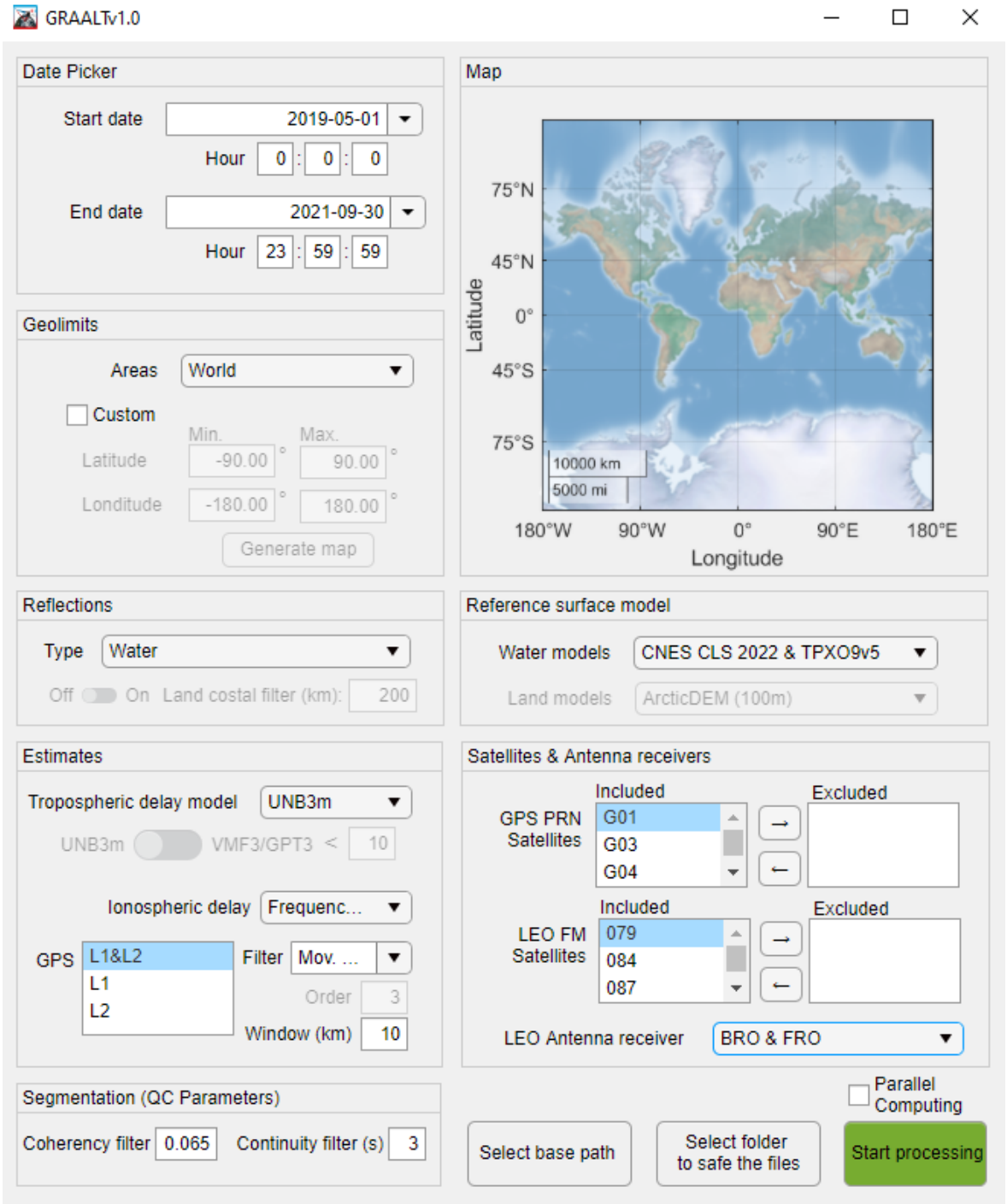

Figure 6.1: GRAALT software interface

Geo-limits

Directly below the date picker, the Geo-limits section enables the user to specify the geographical scope of the analysis. Users can choose from predefined areas such as “World", “South hemisphere", “Hudson Bay", etc. or define custom boundaries by inputting minimum and maximum latitude and longitude values. The "Generate map" button interacts with the Map panel to visualize the selected area, only in the custom boundaries case.

Map

The central portion of the interface displays a global map, which dynamically updates to reflect the selected Geo-limits. This visual representation aids in verifying the chosen geographical parameters.

Reflections

On the left side, beneath the map, the "Reflections" section allows the user to specify the reflection type for processing. Options include "Water", "Land" or "Water and Land" settings. When land reflections are selected, the grayed-out line in the bottom of the panel activates, enabling the user to apply a coastal filter if necessary. This option was added because some DEM models showed some discrepancies between the land and water height values.

Reference Surface Model

Adjacent to the Reflections section, this panel allows the user to choose the appropriate surface models for water and/or land with or without tidal correction for water reflections.

Estimates

This section, located below the GeoLimits panel, enables users to configure parameters related to tropospheric and ionospheric delay models.

The user can select between UNB3m or VMF3/GPT3 or combined models per elevation angle (e.g. UNB3m for angles below 10° and VMF3/GPT3 for angles above 10°).

There are two different ionospheric delay estimate methods that the user can select; ionospheric-free combination and frequency-specific. In case of the frequency specific method the options include the filter types Moving Mean, Moving Median and Savitzky-Golay filter, in which you can modify, window size, and order exclusively of the Savitzky-Golay filter.

Satellites & Antenna Receivers

On the right side, users can include or exclude specific satellites for processing. Separate lists are available for GPS PRN Satellites (e.g., G01, G03, G04) and LEO FM Satellites (e.g., 079, 084, 087). Additionally, the user can specify the type of antenna receiver back (BRO) and/or front (FRO).

Segmentation (QC Parameters)

Below the Estimates section, users can set quality control (QC) parameters, such as coherency and continuity filter values, which influence the segmentation of the data during processing.

Control Buttons

Located at the bottom, three buttons guide file and process management:

Select base path to define the directory for source data. Select folder to save the files for output storage. Start processing to execute the analysis. Parallel Computing Checkbox A checkbox in the lower right corner allows the user to enable parallel computing for enhanced performance.

Once the setting parameters are defined and the software is running, the sequential process undertaken by GRAALTv1.0 software is defined in Figure 6.2. It starts with the ingestion of Level-1B (L1B) data files, which contain residual phase measurements derived from GNSS-R observations. These files provide the fundamental input for all subsequent processing steps.

The first stage involves unwrapping the residual phase measurements. Phase unwrapping is essential to correct discontinuities in the phase signal caused by wrapping effects,

ensuring a continuous and consistent phase signal. Following this, the unwrapped phase data undergoes cycle slip detection and correction. This step identifies and rectifies any abrupt phase discontinuities, which could result from interruptions in the GPS signal or noise interference. This correction step ensures that the processed signal maintains coherence and accuracy.

Simultaneously, tropospheric delay corrections are applied to account for the atmospheric effects on signal propagation. These corrections mitigate delays caused by variations in atmospheric density and water vapor content, enhancing the fidelity of the altimetric retrieval. The residual phase measurements are then aligned with a the acquisition of reference surface model for the posterior height adjustment.

To further refine the data, quality control (QC) filters are applied. These filters screen the data for coherency, identifying segments that meet specific criteria for reliability and high-precision altimetry data. Coherent segments are then passed on to the next stage of processing.

The final stages of the workflow focus on detecting ice-sheet profiles and integrating all the corrected and filtered data to calculate the altimetric height. The ice-sheet profile detection step ensures the identification and isolation of coherent altimetric measurements over ice-covered regions. The process culminates in the calculation of accurate height values, integrating all corrections and adjustments made during the workflow.

This systematic workflow ensures high accuracy and reliability in GNSS-R altimetry, making it suitable for various applications such as monitoring sea-ice dynamics, ice-sheet surface elevation, and ocean surface height variability. Each step in the process addresses specific sources of error or variability, resulting in a robust and consistent altimetric data product.

6.2 Geophysics Laboratory (GL) L2 data product

The Geophysics Laboratory (GL) Level-2 (L2) product provides a comprehensive dataset derived from Level-1B L1B. This product the strictly necessary parameters to complement the

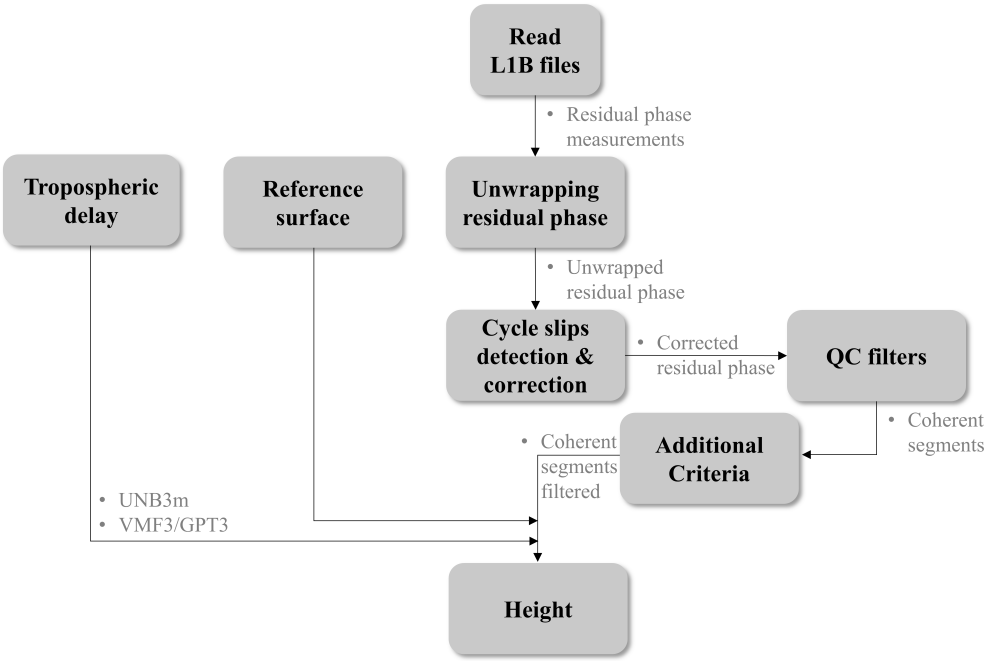

Figure 6.2: GRAALT software flowchart

altimetry data that have been rigorously processed and quality-controlled to deliver accurate values.

The GL L2 product includes various attributes and variables that characterize the altimetry measurements. Table 6.2 presents the attributes, including temporal markers, satellite information, and processing details. Meanwhile, Table 6.1 provides the primary variables contained within the L2 product, such as unwrapped and corrected phase residuals, tropospheric and geometric delays, and computed heights.

The L2 product contains essential information such as time (GPS and UTC), position of the specular point (latitude, longitude, and elevation angle), and phase residuals. Residuals include both reflected and direct signals, saved at multiple levels, such as unwrapped, corrected, and total phase. Critical atmospheric delays, including tropospheric delays and tide estimates.

The processed heights, represented in WGS84 coordinates at both 50 Hz and 1 Hz frequencies, provide the final altimetric values. These heights are adjusted using the smoothed

Table 6.1: List of Variables in the L2 GL product

Variables	**Description**	**Unit**
time	Time of GPS measurement (GPS seconds) - 50Hz	seconds
coarse_time	Time of GPS measurement (GPS seconds) - 1 Hz	seconds
spec_lat	Specular point latitude	degrees
spec_lon	Specular point longitude	degrees
spec_elevation	Specular point elevation angle	degrees
rpa_l1_phase_unwrapped	Reflected L_1 unwrapped phase residuals	meters
rpa_l2_phase_unwrapped	Reflected L_2 unwrapped phase residuals	meters
dpa_l1_phase_unwrapped	Direct L_1 unwrapped phase residuals	meters
dpa_l2_phase_unwrapped	Direct L_2 unwrapped phase residuals	meters
rpa_l1_phase_unwrapped_corr	Reflected L_1 corrected phase residuals	meters
rpa_l2_phase_unwrapped_corr	Reflected L_2 corrected phase residuals	meters
dpa_l1_phase_unwrapped_corr	Direct L_1 corrected phase residuals	meters
dpa_l2_phase_unwrapped_corr	Direct L_2 corrected phase residuals	meters
rpa_l1_phase	Reflected L_1 total phase	meters
rpa_l2_phase	Reflected L_2 total phase	meters
dpa_l1_phase	Direct L_1 total phase	meters
dpa_l2_phase	Direct L_2 total phase	meters
tropo_delay	Tropospheric delay	meters
TPXOv5	Tide estimate	meters
ref_surface	Reference surface model	meters
ref_surface_smoothed	Reference surface model smoothed	meters
geometric_diff	Geometric difference	meters
standard_dev	Standard deviation (Reflected L_1 minus L_2)	Unit-less
height_WGS84_50Hz	Height from WGS84 - 50Hz	meters
height_WGS84_1Hz	Height from WGS84 - 1Hz	meters
segments_id	Segmentation	Unit-less
bias	Reference surface adjustment	meters

reference surface models. The geometric difference, standard deviation, and reference surface adjustments complete the dataset, ensuring robustness and accuracy in altimetric retrievals.

We also ensure that the product includes the minimum necessary parameters to recompute the height as if it were derived again from L1B data. This guarantees flexibility and reproducibility for further analyses, enabling researchers to validate or adapt the methodology as needed. The processing framework incorporates robust corrections and models to optimize the accuracy of the final altimetric measurements.

The parameters and models used to produce the worldwide Level-2 (L2) GL altimetry

Table 6.2: List of Attributes in the L2 GL product

Attributes	**Description**	**Unit**
rms	Root Mean Square error or Sea Level Anomaly	meters
robust_rms	Robust RMS errors of SLA	meters
num_retrievals	Number of coherent measurements	Unit-less
num_segments	Number of segments of the retrievals	Unit-less
year	Year (GPS time)	Unit-less
month	Month (GPS time)	Unit-less
day	Day (GPS time)	Unit-less
hour	Hour (GPS time)	hours
minute	Minuts (GPS time)	minuts
seconds	Seconds (GPS Time)	seconds
UTC_start_time	UTC start time	Unit-less
UTC_stop_time	UTC end time	Unit-less
duration	Duration of the track	seconds
leo_sat	Spire Global FM number	Unit-less
gps_sat	GPS PRN number	Unit-less
tropospheric_model	Tropospheric model name	Unit-less
ref_surface_model	Reference surface model name	Unit-less
proc_center	Processing center	Unit-less
proc_time	Processing time	Unit-less

product are summarized in Table 6.2. Phase unwrapping is performed using the in-house GL algorithm, ensuring coherent retrieval of the reflected signal phase. To account for atmospheric effects, the UNB3m tropospheric delay model is applied, which has demonstrated robust performance and efficient computational time in previous comparisons. The reference surface includes the MSS models SIO CNES-CLS22 and DTU21, complemented by the TPXO9v5 tidal model to correct for oceanic tidal variations.

The segmentation of data is refined using quality control (QC) filters, where the coherency threshold is set at 0.065 and the continuity filter ensures consistent phase measurements within a 3-second window. For the ionospheric correction we selected the frequency specific average L1 and L2 combination, applying a median filter with a window size of 10 km. This configuration minimizes the influence of noise, leading to improved retrievals of sea level anomalies (SLA) and surface heights as demonstrated in Section 4.4.

The results for the initial processing period, spanning from May 1, 2019, to November 30, 2020, demonstrate the performance of the L2 product using the parameters outlined in

Table 6.3: Parameters and models for the world wide L2 GL altimetry product

Parameters:		**Selection:**
Phase unwrapping		GL
Tropospheric delay		UNB3m
Reference surface	MSS	SIO CNES-CLS22 DTU21
	Tides	TPXO9v5
QC filters	Coherency	0.065
	Continuity	3 sec
Frequency combination		L_1 and L_2
Filter	Type	Median
	Order	-
	Window	10 km

Table 6.2. From an initial dataset of 349,403 L1B tracks, 113,765 tracks were successfully processed into the L2 product, representing 33% of the total. The differences between the reference surface model and the heights derived from WGS84 yielded an RMSE of 16.8 cm and a standard deviation of 16.9 cm.

The histogram of RMSE differences (Figure 6.3) highlights that most profiles exhibit small RMSE differences, with the majority concentrated below 50 cm. Specifically, Table 6.4 reveals that 71.5% of the tracks have RMSE values below 30 cm, with 23.7% of tracks achieving RMSEs under 10 cm and 33.4% between 10 cm and 20 cm. Tracks with larger RMSE values (>2 m) account for 4.3% of the total. These results confirm that the combination of precise corrections and optimized parameters ensures high accuracy and consistency for the L2 altimetry product across various regions, including oceans, sea ice, and ice sheets.

Table 6.4: Percentage of RMSE between the GG-R height and the reference surface model

RMSE	< 10 cm	10 cm - 20 cm	20 cm - 30 cm	30 cm - 50 cm	50 cm - 1 m	1 m - 2 m	> 2 m
% of tracks	23.7%	33.4%	13.8%	12.0%	9.1%	3.7%	4.3%

Generally, the GL L2 product represents a high-quality dataset derived from GG-R L1B observations and serves as a valuable resource for ocean, sea-ice, and ice sheet altimetry. The dataset's precision and consistency demonstrate the potential of GG-R as a complement to traditional altimetric missions, particularly in polar and challenging environments.

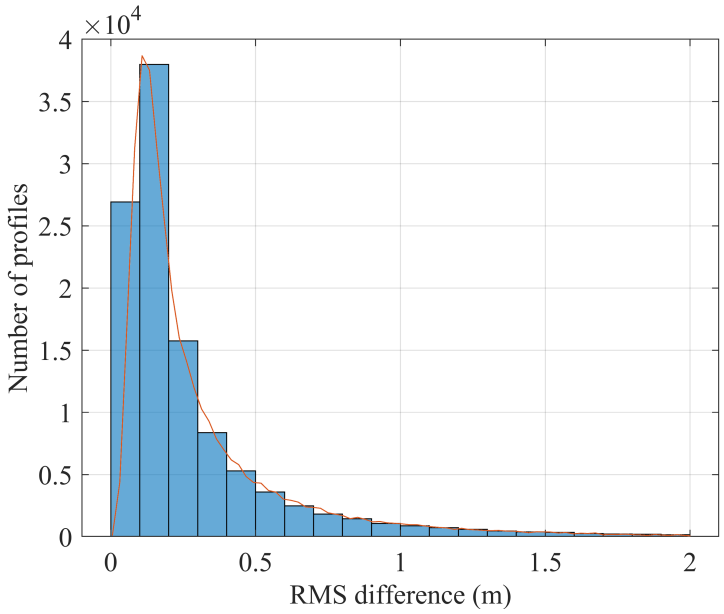

Figure 6.3: Histogram of RMSE differences between GG-R height profiles

Conclusions and Future work

This doctoral thesis presents a comprehensive exploration of dual-frequency Grazing Angle GNSS-Reflectometry (GG-R) for altimetry, advancing in the application of GPS signals in environmental monitoring and remote sensing. The research conducted has significantly expanded the capabilities of GG-R, with applications across various surface types, including ocean, sea-ice, and ice-sheet regions. The outcomes of this work not only validate the potential of GG-R altimetry but also offer practical methodologies and models for its broader application.

The GG-R altimetry technique used was extensively validated over the Hudson Bay region, demonstrating a high correlation between GG-R coherency and sea-ice concentration. Seasonal analyses from January to October 2021 revealed that the measurements coherency percentages were closely tied to sea-ice dynamics, with strong correlations during peak ice concentration periods. Furthermore, improved altimetry accuracy in sea-ice-covered regions was achieved by leveraging dual-frequency GG-R carrier phase signals, reaching decimeter-level precision in sea surface height retrievals. These findings underscore the reliability of GG-R altimetry for monitoring seasonal sea-ice changes and its utility in polar climate studies.

One of the most significant improvements on the GG-R altimetry results in this thesis was the development of an improved ionospheric correction model. This model effectively mitigated the ionospheric delay impact on GG-R altimetry, leading to a significant reduction in height retrieval errors (8 cm). Frequency-specific ionospheric corrections reduced Root Mean Square Errors (RMSE) in GG-R altimetry data by up to 30% compared to conventional

methods. Validation across diverse environments, including the Java Sea and polar regions, confirmed the robustness of these corrections.

Extensive comparisons were made between GG-R altimetry data and traditional satellite altimeters such as Sentinel-3A/3B, CryoSat-2, and Saral. The GG-R altimetry retrievals achieved SLA RMSE values of approximately 47 cm relative to traditional radar altimetry missions, demonstrating comparable performance in sea surface height measurements. Additionally, GG-R altimetry exhibited enhanced coverage in polar regions, performing well in areas beyond the latitudinal limits of radar altimeters and filling critical gaps in current altimetric data. These comparisons validate GG-R altimetry as a complementary technique to existing satellite missions, particularly in polar regions.

The application of GG-R altimetry to ice-sheet altimetry marked another significant contribution of this research. Over 7800 coherent GG-R segments were processed for Greenland and Antarctica from January to October 2021. Height retrievals demonstrated strong alignment with ArcticDEM and REMA reference models, achieving RMSE values below 2 meters over smooth ice-sheet surfaces. GG-R tracks provided detailed insights into ice-sheet surface variability, enabling improved monitoring of ice dynamics and mass balance changes.

The thesis introduced novel software tools and processing algorithms tailored to process GG-R Spire L1B data to produce L2 altimetry data. The software was named GRAALT and its aim is to facilitate to determine the initial parameters and models that needs to be used to process this type of data. The output of this software is the Level-2 (L2) GL altimetry product which contains the altimetry retrievals along with the data necessary to complement the L2, ensuring flexibility for further analysis and validation.

The ongoing process to fulfill the GL L2 dataset produced 113,765 GL tracks, from 349,403 L1B events, resulted in a refined Level-2 (L2) product, representing 33% of the total data from May 2019 to October 2021. Comparisons between the GG-R retrieved heights and reference surface models revealed an RMSE of 16.8 cm and a standard deviation of 16.9 cm.

The findings of this research highlight the potential of GG-R altimetry for Earth obser-

vation. GG-R techniques address the spatial and temporal limitations of radar altimetry, particularly in polar and coastal regions. The versatility of GG-R extends to applications in oceanography, cryospheric science, and climate monitoring, offering high-resolution data for diverse scientific inquiries. The methodologies and models developed in this thesis lay the groundwork for integrating GG-R altimetry into existing Earth observation systems, with potential for cost-effective global monitoring.

Overall, this thesis has established dual-frequency GG-R as a robust and versatile tool for altimetry, delivering significant advancements in accuracy, coverage, and applicability. The methodologies and insights developed herein provide a foundation for future research and operational applications, contributing to our understanding of Earth's dynamic systems and supporting global sustainability efforts.

For future research, the presented work in the thesis pace the way for numerous avenues. Building upon the current understanding, the following directions will enhance the accuracy, utility, and application of GNSS-R and GG-R techniques across diverse environments.

One promising path involves integrating tropospheric models, such as the GFS tropospheric model, to refine SLA standard deviation. Tropospheric delay corrections have already been shown to impact altimetry retrievals significantly, and employing more sophisticated models like GFS can mitigate errors and improve overall precision.

Improving the estimation of specular point positions using POD is another critical direction, particularly for land reflections where errors can be substantial. Land surface variations and roughness complicate specular point estimation, which impacts altimetry accuracy. POD techniques that consider dynamic orbit adjustments will play a vital role in reducing these errors and enhancing performance over diverse terrains.

In addition, there is an opportunity to develop studies focusing on the semi-coherency of GG-R signals. Specifically, investigating the range of semi-coherency could enable its application in precise altimetry. Semi-coherent reflections, particularly in transitional environments such as melting sea ice or mixed surface types, may bridge the gap between coherent and incoherent measurements. This research can further refine models and improve

height retrievals under less favorable conditions.

A related area is the use of ray-path interferometric GG-R phase measurements to achieve absolute height measurements. Comparing these absolute measurements with relative height retrievals from absolute height altimetry methods could provide valuable insights into the accuracy and consistency of interferometric approaches.

Furthermore, coherency studies should be extended as a continuation of Section 4.2, focusing on sea ice concentration correlation over Hudson Bay and perhaps search on other regions. This research has demonstrated promising results in linking coherency percentages with ice distribution. A continuation of this analysis using a larger temporal and spatial dataset could establish more concrete relationships between GNSS-R coherency and cryospheric dynamics, contributing to improved climate monitoring tools.

Expanding data acquisition over land reflections will provide opportunities to study the evolution of ice sheets and glaciers more comprehensively. Larger datasets will allow researchers to monitor trends, identify changes in ice sheet elevation, and contrast GNSS-R with traditional altimetry missions. This could be particularly useful for observing remote regions of Greenland and Antarctica.

The inclusion of additional GNSS constellations, such as Galileo, GLONASS, and BeiDou, will further enhance the robustness of GNSS-R altimetry. By incorporating multiple GNSS systems, the temporal resolution and spatial coverage of reflected signals can be significantly improved. This multi-constellation approach will not only help reduce systematic errors and enhance redundancy, ensuring reliable measurements even in challenging environments, but it will also leverage the use of different GNSS signal frequencies. These frequencies can provide various and therefore valuable information about surface characteristics such as roughness, moisture content, and composition.

Finally, studying triple differences in ionospheric delays across multiple GPS signals (L_1, L_2, and L_5) is a key future direction. Triple-difference methods have shown great potential in reducing ionospheric errors, a major uncertainty source in GNSS-R altimetry. The combination of L_1, L_2, and L_5 signals offers improved accuracy for ionospheric delay corrections, especially in regions with significant ionospheric disturbances.

References

[1] Zhe Zhu and Curtis E. Woodcock. “Continuous change detection and classification of land cover using all available Landsat data”. In: *Remote Sensing of Environment* 144 (2014), pp. 152–171. ISSN: 0034-4257. DOI: https://doi.org/10.1016/j.rse.2014.01.011. URL: https://www.sciencedirect.com/science/article/pii/S0034425714000248.

[2] Nathalie Pettorelli et al. “Using the satellite-derived NDVI to assess ecological responses to environmental change”. In: *Trends in Ecology & Evolution* 20.9 (Sept. 2005), pp. 503–510. ISSN: 0169-5347. DOI: 10.1016/j.tree.2005.05.011. URL: https://doi.org/10.1016/j.tree.2005.05.011.

[3] M.D. King et al. “Cloud and aerosol properties, precipitable water, and profiles of temperature and water vapor from MODIS”. In: *IEEE Transactions on Geoscience and Remote Sensing* 41.2 (2003), pp. 442–458. DOI: 10.1109/TGRS.2002.808226.

[4] Anny Cazenave and William Llovel. “Contemporary Sea Level Rise”. In: *Annual Review of Marine Science* 2.Volume 2, 2010 (2010), pp. 145–173. ISSN: 1941-0611. DOI: https://doi.org/10.1146/annurev-marine-120308-081105. URL: https://www.annualreviews.org/content/journals/10.1146/annurev-marine-120308-081105.

[5] Nature Editorial Board. “The science is clear: sustainable development and climate action are inseparable”. In: *Nature* 620 (2023), pp. 921–922. DOI: 10.1038/d41586-023-02686-3. URL: https://www.nature.com/articles/d41586-023-02686-3.

[6] Carissa Wong. “Earth just had its hottest year on record-climate change is to blame.” In: *Nature* (2023). URL: https://www.nature.com/articles/d41586-023-03523-3.

[7] “Mass balance of the Antarctic Ice Sheet from 1992 to 2017”. In: *Nature* 558.7709 (June 2018), pp. 219–222. ISSN: 1476-4687. DOI: 10.1038/s41586-018-0179-y. URL: http://dx.doi.org/10.1038/s41586-018-0179-y.

[8] W. Turner et al. “Free and open-access satellite data are key to biodiversity conservation”. In: *Biological Conservation* 182 (2015), pp. 173–176. ISSN: 0006-3207. DOI: https://doi.org/10.1016/j.biocon.2014.11.048. URL: https://www.sciencedirect.com/science/article/pii/S000632071400473X.

[9] Michael A. Wulder and Nicholas C. Coops. “Satellites: Make Earth observations open access”. In: *Nature* 513.7516 (Sept. 2014), pp. 30–31. ISSN: 1476-4687. DOI: 10.1038/513030a. URL: https://doi.org/10.1038/513030a.

[10] Christopher S. Ruf and Rajeswari Balasubramaniam. “Development of the CYGNSS Geophysical Model Function for Wind Speed”. In: *IEEE Journal of Selected Topics in Applied Earth Observations and Remote Sensing* 12.1 (2019), pp. 66–77. DOI: 10.1109/JSTARS.2018.2833075.

[11] Nereida Rodriguez-Alvarez et al. “Soil Moisture Retrieval Using GNSS-R Techniques: Experimental Results Over a Bare Soil Field”. In: *IEEE Transactions on Geoscience and Remote Sensing* 47.11 (2009), pp. 3616–3624. DOI: 10.1109/TGRS.2009.2030672.

[12] C. C. Chew and E. E. Small. “Soil Moisture Sensing Using Spaceborne GNSS Reflections: Comparison of CYGNSS Reflectivity to SMAP Soil Moisture”. In: *Geophysical Research Letters* 45.9 (2018), pp. 4049–4057. DOI: https://doi.org/10.1029/2018GL077905. eprint: https://agupubs.onlinelibrary.wiley.com/doi/pdf/10.1029/2018GL077905. URL: https://agupubs.onlinelibrary.wiley.com/doi/abs/10.1029/2018GL077905.

[13] Paulo T. Setti Jr. and Sajad Tabibi. “Evaluation of Spire GNSS-R reflectivity from multiple GNSS constellations for soil moisture estimation”. In: *International Journal of Remote Sensing* 44.20 (2023), pp. 6422–6441. DOI: 10.1080/01431161.2023.2270108. URL: https://doi.org/10.1080/01431161.2023.2270108.

[14] Vu A. Nguyen et al. “Initial GNSS Phase Altimetry Measurements From the Spire Satellite Constellation”. In: *Geophysical Research Letters* 47.15 (2020). e2020GL088308 10.1029/2020GL088308. DOI: https://doi.org/10.1029/2020GL088308. eprint: https://agupubs.onlinelibrary.wiley.com/doi/pdf/10.1029/2020GL088308. URL: https://agupubs.onlinelibrary.wiley.com/doi/abs/10.1029/2020GL088308.

[15] Weiqiang Li et al. “Exploration of Multi-Mission Spaceborne GNSS-R Raw IF Data Sets: Processing, Data Products and Potential Applications”. In: *Remote Sensing* 14.6 (2022). ISSN: 2072-4292. DOI: 10.3390/rs14061344. URL: https://www.mdpi.com/2072-4292/14/6/1344.

[16] J. Cartwright, C. J. Banks, and M. Srokosz. “Improved GNSS-R bi-static altimetry and independent digital elevation models of Greenland and Antarctica from TechDemoSat-1”. In: *The Cryosphere* 14.6 (2020), pp. 1909–1917. DOI: 10.5194/tc-14-1909-2020. URL: https://tc.copernicus.org/articles/14/1909/2020/.

[17] Randall Friedl and Stacey Boland. “Mission Costs of Earth-Observing Satellites”. In: *Encyclopedia of Remote Sensing*. Ed. by Eni G. Njoku. New York, NY: Springer New York, 2014, pp. 405–407. ISBN: 978-0-387-36699-9. DOI: 10.1007/978-0-387-36699-9_106. URL: https://doi.org/10.1007/978-0-387-36699-9_106.

[18] UKRI. *GtR — gtr.ukri.org.* [Accessed 03-09-2024]. URL: https://gtr.ukri.org/projects?ref=100896#/tabOverview.

[19] *U-M To Lead $152M NASA Satellite Project — cbsnews.com*. [Accessed 03-09-2024]. URL: https://www.cbsnews.com/detroit/news/u-m-to-lead-152m-nasa-satellite-project/.

[20] Peter B. de Selding. *Cubesat constellation operator Spire offers to launch 20 customer payloads in 12 months for $12 million - Space Intel Report — spaceintelreport.com*. [Accessed 03-09-2024]. URL: https://www.spaceintelreport.com/cubesat-constellation-operator-spire-offers-to-launch-20-customer-payloads-in-12-months-for-12-million/.

[21] Safran - Navigation and Timing. *GNSS Spectrum ROW*. [Accessed 04-09-2024]. URL: https://safran-navigation-timing.com/document/the-gnss-spectrum/.

[22] Fran Fabra. *GNSS-R as a source of opportunity for Remote Sensing of the Cryosphere*. Universitat Politècnica de Catalunya (UPC), 2013. URL: https://www.researchgate.net/publication/282005286_GNSS-R_as_a_Source_of_Opportunity_for_Remote_Sensing_of_the_Cryosphere.

[23] Pratap Misra and Per Enge. *Global Positioning System: Signals, Measurements, and Performance*. Ganga-Jamuna Press, 2005. ISBN: 978-0970954428. URL: https://g.co/kgs/1TZTQE.

[24] Aberto Alonso Arroyo. *Contributions to Land, Sea, and Sea-ice Remote Sensing Using GNSS-Reflectometry*. Universitat Politècnica de Catalunya, Departament de Teoría del Senyal i Comunicacions, 2016. URL: https://www.tdx.cat/handle/10803/404062#page=1.

[25] *GPS.gov: Space Segment — gps.gov*. [Accessed 04-09-2024]. URL: https://www.gps.gov/systems/gps/space/.

[26] C.D. Hall and R.A. Cordey. "Multistatic Scatterometry". In: *International Geoscience and Remote Sensing Symposium, 'Remote Sensing: Moving Toward the 21st Century'.* Vol. 1. 1988, pp. 561–562. DOI: 10.1109/IGARSS.1988.570200.

[27] Manuel Martin-Neira. "A PAssive Reflectometry and Interferometry System (PARIS): Application to ocean altimetry". In: *ESA Journal* (Jan. 1993), pp. 331–355.

[28] Katzberg Stephen J. and Jr James L. Garrison. *Utilizing GPS To Determine Ionospheric Delay Over the Ocean*. Tech. rep. 1996.

[29] James L. Garrison, Stephen J. Katzberg, and Michael I. Hill. “Effect of sea roughness on bistatically scattered range coded signals from the Global Positioning System”. In: *Geophysical Research Letters* 25.13 (1998), pp. 2257–2260. DOI: https://doi.org/10.1029/98GL51615. URL: https://agupubs.onlinelibrary.wiley.com/doi/abs/10.1029/98GL51615.

[30] V.U. Zavorotny and A.G. Voronovich. “Scattering of GPS signals from the ocean with wind remote sensing application”. In: *IEEE Transactions on Geoscience and Remote Sensing* 38.2 (2000), pp. 951–964. DOI: 10.1109/36.841977.

[31] Martin Unwin, Scott Gleason, and Michael Brennan. “The space GPS reflectometry experiment on the UK disaster monitoring constellation satellite”. In: *Proceedings of the 16th International Technical Meeting of the Satellite Division of The Institute of Navigation (ION GPS/GNSS 2003)*. 2003, pp. 2656–2663.

[32] Martin Unwin et al. “Spaceborne GNSS-Reflectometry on TechDemoSat-1: Early Mission Operations and Exploitation”. In: *IEEE Journal of Selected Topics in Applied Earth Observations and Remote Sensing* 9.10 (2016), pp. 4525–4539. DOI: 10.1109/JSTARS.2016.2603846.

[33] C. Ruf et al. “CYGNSS: Enabling the Future of Hurricane Prediction [Remote Sensing Satellites]”. In: *IEEE Geoscience and Remote Sensing Magazine* 1.2 (2013), pp. 52–67. DOI: 10.1109/MGRS.2013.2260911.

[34] Christopher S. Ruf et al. “A New Paradigm in Earth Environmental Monitoring with the CYGNSS Small Satellite Constellation”. In: *Scientific Reports* 8 (2018). DOI: 10.1038/s41598-018-27127-4. URL: https://doi.org/10.1038/s41598-018-27127-4.

[35] Carlos Molina and Adriano Camps. “First Evidences of Ionospheric Plasma Depletions Observations Using GNSS-R Data from CYGNSS”. In: *Remote Sensing* (Nov. 2020). DOI: 10.3390/rs12223782.

[36] Y. Wang and J. Morton. “Preliminary Result of GNSS-R Carrier Phase Altimetry over Glaciers”. In: *CYGNSS Science Team Meeting*. 2022.

[37] James Garrison et al. *GNSS Reflectometry for Earth Remote Sensing*. Dec. 2020. DOI: 10.1002/9781119458449.ch34. URL: http://dx.doi.org/10.1002/9781119458449.ch34.

[38] Maria Paola Clarizia et al. “Spaceborne GNSS-R Minimum Variance Wind Speed Estimator”. In: *IEEE Transactions on Geoscience and Remote Sensing* 52.11 (2014), pp. 6829–6843. DOI: 10.1109/TGRS.2014.2303831.

[39] Alberto Alonso-Arroyo et al. “Retrieval of Significant Wave Height and Mean Sea Surface Level Using the GNSS-R Interference Pattern Technique: Results From a Three-Month Field Campaign”. In: *IEEE Transactions on Geoscience and Remote Sensing* 53.6 (2015), pp. 3198–3209. DOI: 10.1109/TGRS.2014.2371540.

[40] Jinwei Bu et al. “Estimation of Swell Height Using Spaceborne GNSS-R Data from Eight CYGNSS Satellites”. In: *Remote Sensing* 14 (Sept. 2022), p. 4634. DOI: 10.3390/rs14184634.

[41] Paulo T. Setti, Sajad Tabibi, and Tonie van Dam. “CYGNSS GNSS-R Data for Inundation Monitoring in the Brazilian Pantanal Wetland”. In: *IGARSS 2022 - 2022 IEEE International Geoscience and Remote Sensing Symposium*. 2022, pp. 5531–5534. DOI: 10.1109/IGARSS46834.2022.9883409.

[42] Jessica Cartwright, Christopher J. Banks, and Meric Srokosz. “Sea Ice Detection Using GNSS-R Data From TechDemoSat-1”. In: *Journal of Geophysical Research. Oceans* 124.8 (July 2019). ISSN: 2169-9275. DOI: 10.1029/2019jc015327. URL: https://www.osti.gov/biblio/1577553.

[43] Nereida Rodriguez-Alvarez et al. “The Use of SMAP-Reflectometry in Science Applications: Calibration and Capabilities”. In: *Remote Sensing* 11.20 (2019). ISSN: 2072-4292. DOI: 10.3390/rs11202442. URL: https://www.mdpi.com/2072-4292/11/20/2442.

[44] Andreas Dielacher, Heinrich Fragner, and Otto Koudelka. “PRETTY – passive GNSS-Reflectometry for CubeSats”. In: *e & i Elektrotechnik und Informationstechnik* 139.1

(Feb. 2022), pp. 25–32. ISSN: 1613-7620. DOI: 10.1007/s00502-022-00993-7. URL: https://doi.org/10.1007/s00502-022-00993-7.

[45] Nereida Rodriguez-Alvarez, Joan Francesc Munoz-Martin, and Mary Morris. "Latest Advances in the Global Navigation Satellite System—Reflectometry (GNSS-R) Field". In: *Remote Sensing* 15.8 (2023). ISSN: 2072-4292. DOI: 10.3390/rs15082157. URL: https://www.mdpi.com/2072-4292/15/8/2157.

[46] Saleh Abdalla et al. "Altimetry for the future: Building on 25 years of progress". In: *Elsevier* (July 2021). URL: https://doi.org/10.1016/j.asr.2021.01.022.

[47] Dallas Masters and Vu A. Nguyen. *Spire Grazing Angle GNSS-R Level 1 Product Description*. Version 1.0. Nov. 2020.

[48] Vu Nguyen, Matthieu Talpe, and Philip Jales. *Spire Grazing Angle GNSS-R Level 2 Altimetry*. Version 1.2. June 2022.

[49] Ahmed El Rabbany et al. "The effect of physical correlations on the ambiguity resolution and accuracy estimation in GPS differential postioning". In: (1994).

[50] John A. Klobuchar. "Ionospheric Time-Delay Algorithm for Single-Frequency GPS Users". In: *IEEE Transactions on Aerospace and Electronic Systems* AES-23.3 (1987), pp. 325–331. DOI: 10.1109/TAES.1987.310829.

[51] G. Di Giovanni and S.M. Radicella. "An analytical model of the electron density profile in the ionosphere". In: *Advances in Space Research* 10.11 (1990), pp. 27–30. ISSN: 0273-1177. DOI: https://doi.org/10.1016/0273-1177(90)90301-F. URL: https://www.sciencedirect.com/science/article/pii/027311779090301F.

[52] U.S. Department of Defense. *IS-GPS-200*. Tech. rep. Interface Specification, Revision H. Global Positioning Systems Directorate, 2018. URL: https://www.gps.gov/technical/icwg/IS-GPS-200M.pdf.

[53] European Commission. *Ionospheric Correction Algorithm for Galileo Single Frequency Users*. Tech. rep. Technical Note. European Commission, 2016. URL: https://www.

gsc-europa.eu/sites/default/files/sites/all/files/Galileo_Ionospheric_Model.pdf.

[54] M. Hernández-Pajares et al. “Wide-Area Ionospheric Delay Corrections for GNSS: Assessment of the State of the Art and New Approaches”. In: *IEEE Transactions on Geoscience and Remote Sensing* 47.10 (2009), pp. 3213–3221. DOI: 10.1109/TGRS.2009.2014941.

[55] JF Zumberge. “Precise point positioning for the efficient and robust analysis of GPS data from large network”. In: *J. Geophys. Res.* 102 (1997), pp. 5–005.

[56] M. Hernández-Pajares, J.M. Juan, and J. Sanz. “New approaches in global ionospheric determination using ground GPS data”. In: *Journal of Atmospheric and Solar-Terrestrial Physics* 61.16 (1999), pp. 1237–1247. ISSN: 1364-6826. DOI: https://doi.org/10.1016/S1364-6826(99)00054-1. URL: https://www.sciencedirect.com/science/article/pii/S1364682699000541.

[57] *Ionosphere-free Combination for Dual Frequency Receivers - Navipedia — gssc.esa.int*. https://gssc.esa.int/navipedia/index.php/Ionosphere-free_Combination_for_Dual_Frequency_Receivers. [Accessed 12-09-2024].

[58] J. Saastamoinen. “Atmospheric Correction for the Troposphere and Stratosphere in Radio Ranging Satellites”. In: *The Use of Artificial Satellites for Geodesy*. American Geophysical Union (AGU), 1972, pp. 247–251. ISBN: 9781118663646. DOI: https://doi.org/10.1029/GM015p0247. eprint: https://agupubs.onlinelibrary.wiley.com/doi/pdf/10.1029/GM015p0247. URL: https://agupubs.onlinelibrary.wiley.com/doi/abs/10.1029/GM015p0247.

[59] H. S. Hopfield. “Two-quartic tropospheric refractivity profile for correcting satellite data”. In: *Journal of Geophysical Research (1896-1977)* 74.18 (1969), pp. 4487–4499. DOI: https://doi.org/10.1029/JC074i018p04487. URL: https://agupubs.onlinelibrary.wiley.com/doi/abs/10.1029/JC074i018p04487.

[60] Leandro R., Santos M., and Langley R. “UNB Neutral Atmosphere Models: Development and Performance”. In: *Proceedings of the 2006 National Technical Meeting of The Institute of Navigation, Monterey, California, 18-20 January*. 2006. URL: https://gge.ext.unb.ca/Resources/unb3m/unb3m.html.

[61] D. Landskron and J. Böhm. “VMF3/GPT3: refined discrete and empirical troposphere mapping functions”. In: *Journal of Geodesy* 92 (2018), pp. 349–360. DOI: https://doi.org/10.1007/s00190-017-1066-2.

[62] J. Boehm et al. “Global Mapping Function (GMF): A new empirical mapping function based on numerical weather model data”. In: *Geophysical Research Letters* 33.7 (2006). DOI: https://doi.org/10.1029/2005GL025546. eprint: https://agupubs.onlinelibrary.wiley.com/doi/pdf/10.1029/2005GL025546. URL: https://agupubs.onlinelibrary.wiley.com/doi/abs/10.1029/2005GL025546.

[63] Ole Andersen, Per Knudsen, and Lars Stenseng. “The DTU13 MSS (Mean Sea Surface) and MDT (Mean Dynamic Topography) from 20 Years of Satellite Altimetry”. In: *IGFS 2014*. Ed. by Shuanggen Jin and Riccardo Barzaghi. Cham: Springer International Publishing, 2016, pp. 111–121. ISBN: 978-3-319-39820-4.

[64] Ole Baltazar Andersen et al. “The DTU15 MSS (Mean Sea Surface) and DTU15LAT (Lowest Astronomical Tide) reference surface”. English. In: ESA Living Planet Symposium 2016 ; Conference date: 09-05-2016 Through 13-05-2016. 2016. URL: http://lps16.esa.int/.

[65] O. Andersen, P. Knudsen, and L. Stenseng. “A New DTU18 MSS Mean Sea Surface – Improvement from SAR Altimetry”. English. In: 25 years of progress in radar altimetry symposium ; Conference date: 24-09-2018 Through 29-09-2018. 2018, p. 172.

[66] O. B. Andersen et al. “A new high resolution Mean Sea Surface (DTU21MSS) for improved sea level monitoring”. In: *EGU General Assembly 2021, online, 19–30 Apr 2021, EGU21-16084* (2021). DOI: https://doi.org/10.5194/egusphere-egu21-16084.

[67] David T. Sandwell. *Adding Mean Sea Surface (MSS) as an Altimetry Product*. 2024. DOI: 10.21221/S26P4H. URL: https://escholarship.org/uc/item/08z6v9wq.

[68] CLS. "CNES-CLS 2022 Mean Sea Surface". In: (2022). DOI: 10.24400/527896/A01-2022.017. URL: https://www.aviso.altimetry.fr/en/data/products/auxiliary-products/mss/mss-global-cnes-cls.html.

[69] Chad A. Greene, Tyler Sutterley, and Susan Howard. *chadagreene/Tide-Model-Driver*. Oct. 31, 2024. URL: https://github.com/chadagreene/Tide-Model-Driver.

[70] Earth & Space Research (ESR). *Arc2km Arctic Tidal Model*. https://www.esr.org/research/polar-tide-models/. High-resolution Arctic tidal model available from Earth & Space Research (ESR). 2016.

[71] C. Hirt and M. Rexer. "Earth2014: 1 arc-min shape, topography, bedrock and ice-sheet models - available as gridded data and degree-10,800 spherical harmonics". In: *International Journal of Applied Earth Observation and Geoinformation 39, 103-112* (). DOI: 10.10.1016/j.jag.2015.03.001.

[72] Claire Porter et al. *ArcticDEM, Version 3*. Version V1. 2018. DOI: 10.7910/DVN/OHHUKH. URL: https://doi.org/10.7910/DVN/OHHUKH.

[73] Ian Howat et al. *The Reference Elevation Model of Antarctica - Mosaics, Version 1.1*. Type: dataset. 2022. DOI: 10.7910/DVN/EBW8UC. URL: https://dataverse.harvard.edu/citation?persistentId=doi:10.7910/DVN/EBW8UC (visited on 11/29/2022).

[74] *Global Ocean Gridded L4 Sea Surface Heights And Derived Variables Reprocessed 1993 Ongoing*. Accessed: 2023-12-22. URL: https://data.marine.copernicus.eu/product/SEALEVEL_GLO_PHY_L4_MY_008_047/description.

[75] Raquel N. Buendía, Sajad Tabibi, and Matthieu Talpe. "Preliminary GNSS-R Altimetry in the Hudson Bay Based on Spire Grazing Angle Measurements". In: *IGARSS 2022 - 2022 IEEE International Geoscience and Remote Sensing Symposium*. 2022, pp. 7135–7138. DOI: 10.1109/IGARSS46834.2022.9883079.

[76] Raquel N. Buendía, Sajad Tabibi, and Olivier Francis. “Relation between GG-R Carrier Phase Signal Coherency and Sea ICE Concentration over Hudson Bay”. In: (2024), pp. 92–95. DOI: 10.1109/IGARSS53475.2024.10640714.

[77] Raquel N. Buendía, Sajad Tabibi, and Matthieu Talpe. “An Improved Ionospheric Correction Model for Grazing Angle GNSS-R Altimetry”. In: *IGARSS 2023 - 2023 IEEE International Geoscience and Remote Sensing Symposium*. 2023, pp. 4332–4335. DOI: 10.1109/IGARSS52108.2023.10282507.

[78] Raquel N. Buendía et al. “Ice sheet height retrievals from Spire grazing angle GNSS-R”. In: *Remote Sensing of Environment* 297 (2023), p. 113757. ISSN: 0034-4257. DOI: https://doi.org/10.1016/j.rse.2023.113757. URL: https://www.sciencedirect.com/science/article/pii/S0034425723003085.

[79] Alexandre S. Gagnon and William A. Gough. “Trends in the Dates of Ice Freeze-up and Breakup over Hudson Bay, Canada”. In: *Arctic* 58.4 (2005), pp. 370–382. ISSN: 00040843. URL: http://www.jstor.org/stable/40513104.

[80] W. N. Meier et al. “NOAA/NSIDC Climate Data Record of Passive Microwave Sea Ice Concentration,Version 4.” In: *Hudson Bay sea-ice extension product. Boulder, Colorado USA. NSIDC: National Snow and Ice Data Center. Accessed: 10/12/2021* (2021). DOI: https://doi.org/10.7265/efmz-2t65. URL: https://www.ncdc.noaa.gov/snow-and-ice/regional-sea-ice/extent/Hudson/0.

[81] Gary D. Egbert and Svetlana Y. Erofeeva. “Efficient Inverse Modeling of Barotropic Ocean Tides”. In: *Journal of Atmospheric and Oceanic Technology* 19.2 (2002), pp. 183–204. DOI: 10.1175/1520-0426(2002)019<0183:EIMOBO>2.0.CO;2. URL: https://journals.ametsoc.org/view/journals/atot/19/2/1520-0426_2002_019_0183_eimobo_2_0_co_2.xml.

[82] Fetterer F., J. S. Stewart, and W. N. Meier. *MASAM2: Daily 4 km Arctic Sea Ice Concentration Version 2*. 2023. DOI: 10.7265/bqd9-vm28. URL: https://nsidc.org/data/G10005/versions/2.

[83] MW Strassburg et al. “Sea level trends in Southeast Asian seas”. In: *Climate of the Past* 11.5 (2015), pp. 743–750.

[84] William S Cleveland, Eric Grosse, and William M Shyu. “Local regression models”. In: *Statistical models in S*. Routledge, 2017, pp. 309–376.

[85] Mary J Brodzik et al. “EASE-Grid 2.0: Incremental but significant improvements for Earth-gridded data sets”. In: *ISPRS International Journal of Geo-Information* 1.1 (2012), pp. 32–45. DOI: 10.3390/ijgi1010032.

[86] Craig J. Donlon, Robert Cullen, and Luisella Giulicchi et al. “The Copernicus Sentinel-6 mission: Enhanced continuity of satellite sea level measurements from space”. In: *Remote Sensing of Environment* 258 (2021), p. 112395. ISSN: 0034-4257. DOI: https://doi.org/10.1016/j.rse.2021.112395. URL: https://www.sciencedirect.com/science/article/pii/S0034425721001139.

[87] R. S. Nerem et al. “Climate-change–driven accelerated sea-level rise detected in the altimeter ERA”. In: *Proceedings of the National Academy of Sciences* 115.9 (2018), pp. 2022–2025. DOI: 10.1073/pnas.1717312115. eprint: https://www.pnas.org/doi/pdf/10.1073/pnas.1717312115. URL: https://www.pnas.org/doi/abs/10.1073/pnas.1717312115.

[88] R Kwok. “Arctic sea ice thickness, volume, and multiyear ice coverage: losses and coupled variability (1958–2018)”. In: *Environmental Research Letters* 13.10 (Oct. 2018), p. 105005. DOI: 10.1088/1748-9326/aae3ec. URL: https://dx.doi.org/10.1088/1748-9326/aae3ec.

[89] Lee-Lueng Fu et al. “EDDY DYNAMICS FROM SATELLITE ALTIMETRY”. In: *Oceanography* 23.4 (2010), pp. 14–25. ISSN: 10428275, 2377617X. URL: http://www.jstor.org/stable/24860859 (visited on 10/18/2023).

[90] M. Martin-Neira et al. “The PARIS concept: an experimental demonstration of sea surface altimetry using GPS reflected signals”. In: *IEEE Transactions on Geoscience and Remote Sensing* 39.1 (2001), pp. 142–150. DOI: 10.1109/36.898676.

[91] Stephen T. Lowe et al. “5-cm-Precision aircraft ocean altimetry using GPS reflections”. In: *Geophysical Research Letters* 29.10 (2002), pp. 13-1-13–4. DOI: https://doi.org/10.1029/2002GL014759. eprint: https://agupubs.onlinelibrary.wiley.com/doi/pdf/10.1029/2002GL014759. URL: https://agupubs.onlinelibrary.wiley.com/doi/abs/10.1029/2002GL014759.

[92] A. M. Semmling et al. “Sea surface topography retrieved from GNSS reflectometry phase data of the GEOHALO flight mission”. In: *Geophysical Research Letters* 41.3 (2014), pp. 954–960. DOI: https://doi.org/10.1002/2013GL058725. eprint: https://agupubs.onlinelibrary.wiley.com/doi/pdf/10.1002/2013GL058725. URL: https://agupubs.onlinelibrary.wiley.com/doi/abs/10.1002/2013GL058725.

[93] Sajad Tabibi and Olivier Francis. “Can GNSS-R Detect Abrupt Water Level Changes?” In: *Remote Sensing* 12 (Nov. 2020), p. 3614. DOI: 10.3390/rs12213614.

[94] Sajad Tabibi et al. “SNR-Based GNSS-R for Coastal Sea-Level Altimetry”. In: *Geosciences* 11.9 (Sept. 2021). Number: 9 Publisher: Multidisciplinary Digital Publishing Institute, p. 391. ISSN: 2076-3263. DOI: 10.3390/geosciences11090391. URL: https://www.mdpi.com/2076-3263/11/9/391 (visited on 07/29/2024).

[95] Xiaohui Li, Guoqi Han, and Jingsong Yang. “Chapter 9 - Application of satellite altimetry for storm surge research and simulations along the coast of China”. In: *Coastal Altimetry*. Ed. by Stefano Vignudelli and Nurul Hazrina Idris. Elsevier, 2023, pp. 159–175. ISBN: 978-0-323-91708-7. DOI: https://doi.org/10.1016/B978-0-323-91708-7.00010-9. URL: https://www.sciencedirect.com/science/article/pii/B9780323917087000109.

[96] *European Space Agency - Cryosat-2*. Accessed: 2023-11-23. URL: https://earth.esa.int/eogateway/missions/cryosat.

[97] *Indian Space Research Organisation (ISRO) - SARAL*. Accessed: 2023-11-23. URL: https://www.isro.gov.in/SARAL.html.

[98] *European Space Agency Copernicus - Sentinel*. Accessed: 2023-11-23. URL: https://sentinels.copernicus.eu/web/sentinel/copernicus.

[99] Apr. 2022. URL: https://www.aviso.altimetry.fr/fileadmin/documents/data/tools/hdbk_L2P_S3_S6.pdf.

[100] Marie-Isabel Pujol et al. “Gauging the improvement of recent mean sea surface models: A new approach for identifying and quantifying their errors”. In: *Journal of Geophysical Research: Oceans, 123* (2018). DOI: https://doi.org/10.1029/2017JC013503.

[101] Andersen O. et al. “The DTU15 MSS (Mean Sea Surface) and DTU15LAT (Lowest Astronomical Tide) reference surface”. In: *ESA Living Planet Symposium 2016 - Prague, Czech Republic.* (2018). URL: http://lps16.esa.int/page_session189.php#1579p.

[102] Maria Paola Clarizia et al. “First spaceborne observation of sea surface height using GPS-Reflectometry”. In: *Geophysical Research Letters* 43.2 (2016), pp. 767–774. DOI: https://doi.org/10.1002/2015GL066624. eprint: https://agupubs.onlinelibrary.wiley.com/doi/pdf/10.1002/2015GL066624. URL: https://agupubs.onlinelibrary.wiley.com/doi/abs/10.1002/2015GL066624.

[103] L. Peraza et al. “Analysis of Grazing GNSS Reflections Observed at the Zeppelin Mountain Station, Spitsbergen”. In: *Radio Science* 52.11 (2017), pp. 1352–1362. DOI: https://doi.org/10.1002/2017RS006272. eprint: https://agupubs.onlinelibrary.wiley.com/doi/pdf/10.1002/2017RS006272. URL: https://agupubs.onlinelibrary.wiley.com/doi/abs/10.1002/2017RS006272.

[104] Estel Cardellach et al. “First Precise Spaceborne Sea Surface Altimetry With GNSS Reflected Signals”. In: *IEEE Journal of Selected Topics in Applied Earth Observations and Remote Sensing* PP (Dec. 2019), pp. 1–11. DOI: 10.1109/JSTARS.2019.2952694.

[105] Carolyn J. Roesler et al. “Coherent GNSS-Reflections Characterization Over Ocean and Sea Ice Based on Spire Global CubeSat Data”. In: *IEEE Transactions on Geoscience and Remote Sensing* 60 (2022), pp. 1–18. DOI: 10.1109/TGRS.2021.3129999.

[106] M. Tschudi et al. *EASE-Grid Sea Ice Age, Version 4*. 2019. DOI: 10.5067/UTAV7490FEPB. URL: https://daacdata.apps.nsidc.org/pub/DATASETS/nsidc0611_seaice_age_v4/browse/2021/iceage_nh_12.5km_20210326_20210401_v4.1.png.

[107] Detlef Stammer and Anny Cazenave. *Satellite altimetry over oceans and land surfaces*. CRC press, 2017.

[108] E. Cardellach et al. "Carrier phase delay altimetry with GPS-reflection/occultation interferometry from low Earth orbiters". In: *Geophysical Research Letters* 31.10 (2004). DOI: https://doi.org/10.1029/2004GL019775. eprint: https://agupubs.onlinelibrary.wiley.com/doi/pdf/10.1029/2004GL019775. URL: https://agupubs.onlinelibrary.wiley.com/doi/abs/10.1029/2004GL019775.

[109] Antonio Rius et al. "Feasibility of GNSS-R ice sheet altimetry in Greenland using TDS-1". In: *Remote Sensing* 9 (July 2017), p. 742. DOI: 10.3390/rs9070742.

[110] K. M. Brunt, T. A. Neumann, and B. E. Smith. "Assessment of ICESat-2 Ice Sheet Surface Heights, Based on Comparisons Over the Interior of the Antarctic Ice Sheet". In: *Geophysical Research Letters* 46.22 (2019), pp. 13072–13078. ISSN: 0094-8276. DOI: https://doi.org/10.1029/2019GL084886. URL: https://agupubs.onlinelibrary.wiley.com/doi/abs/10.1029/2019GL084886.

[111] Thomas Slater et al. "A new digital elevation model of Antarctica derived from CryoSat-2 altimetry". In: *The Cryosphere* 12.4 (2018), pp. 1551–1562. ISSN: 1994-0424;1994-0416; DOI: 10.5194/tc-12-1551-2018.

[112] Inès Otosaka, Andrew Shepherd, and Malcolm McMillan. "Ice Sheet Elevation Change in West Antarctica From Ka-Band Satellite Radar Altimetry". In: *Geophysical Research Letters* (2019). ISSN: 0094-8276. DOI: 10.1029/2019GL084271. URL: https://doi.org/10.1029/2019GL084271.

[113] T. Parrinello et al. "CryoSat: ESA's ice mission – Eight years in space". In: *Advances in Space Research* 62.6 (2018), pp. 1178–1190. ISSN: 0273-1177. DOI: https://doi.org/10.1016/j.asr.2018.04.014. URL: https://www.sciencedirect.com/science/article/pii/S0273117718303296.

[114] Thorsten Markus et al. “The Ice, Cloud, and land Elevation Satellite-2 (ICESat-2): Science requirements, concept, and implementation”. In: *Remote Sensing of Environment* 190 (2017), pp. 260–273. ISSN: 0034-4257. DOI: 10.1016/j.rse.2016.12.029.

[115] M. Meloni et al. “CryoSat Ice Baseline-D validation and evolutions”. In: *The Cryosphere* 14.6 (2020), pp. 1889–1907. DOI: 10.5194/tc-14-1889-2020. URL: https://tc.copernicus.org/articles/14/1889/2020/.

[116] Chad A. Greene, David E. Gwyther, and Donald D. Blankenship. “Antarctic Mapping Tools for Matlab”. In: *Computers & Geosciences* 104 (July 2017), pp. 151–157. DOI: 10.1016/j.cageo.2016.08.003. URL: https://doi.org/10.10162Fj.cageo.2016.08.003.

[117] I. M. Howat et al. “The Reference Elevation Model of Antarctica”. In: *The Cryosphere* 13.2 (2019), pp. 665–674. DOI: 10.5194/tc-13-665-2019. URL: https://tc.copernicus.org/articles/13/665/2019/.

[118] Paul Morin et al. “ArcticDEM; A Publically Available, High Resolution Elevation Model of the Arctic”. In: *EGU General Assembly Conference Abstracts*. EGU General Assembly Conference Abstracts. Apr. 2016, EPSC2016-8396, EPSC2016–8396.

[119] Andrew Shepherd et al. “Trends in Antarctic Ice Sheet Elevation and Mass”. In: *Geophysical Research Letters* (2019). ISSN: 0094-8276. DOI: 10.1029/2019GL082182.

[120] Ben Smith et al. “Pervasive ice sheet mass loss reflects competing ocean and atmosphere processes”. In: *Science* 368.6496 (2020), pp. 1239–1242. DOI: 10.1126/science.aaz5845. URL: https://science.sciencemag.org/content/sci/368/6496/1239.full.pdf.

[121] Yang Wang and Y. Jade Morton. “Coherent GNSS Reflection Signal Processing for High-Precision and High-Resolution Spaceborne Applications”. In: *IEEE TRANSACTIONS ON GEOSCIENCE AND REMOTE SENSING* 59.1 (2021), pp. 831–840.